Diss. ETH No. 13930

Experimental and Theoretical Study of Ionic Clustering Reactions Involving Water

a dissertation submitted to the

SWISS FEDERAL INSTITUTE OF TECHNOLOGY (ETH)

for the degree of
Doctor of Natural Sciences

presented by

Alexander Likholyot

dipl. phys., Moscow Institute of Physics and Technology

accepted on the recommendation of

Prof. T. M. Seward, examiner
Dr. J. K. Hovey, co-examiner
Prof. H.-E. Audier, co-examiner

November 2000

Contents

Acknowledgements

I would like to thank all the people who helped me at various stages of this project.

First and foremost, I would like to thank my advisor, Dr. Jamey Hovey, who guided me through this research program. From him I learned much about mass spectrometry and science in general. Jamey's design of the ion source and overall HPMS experiment defined the success of our project. His drive for scientific excellence and high standards pushed me to aspire for the same. I enjoyed our scientific discussions that have always been a lot of fun. I thank him for being patient when I was stubborn or plain annoying. Aside from being a teacher, Jamey has always been a good friend.

I also would like to thank Professor Terry Seward for hosting and supporting our research project, helping me to keep the faith that I would see it through to the end and helping to overcome many bureaucratic obstacles. I greatly enjoyed the scientific atmosphere that Terry created in his group.

This project required a lot of design and construction of various parts for the experimental setup. I would like to thank Bruno Zürcher and Urs Menet for machining vital components for our HPMS apparatus. I also thank Urs Graber and Sven Girsperger for their help with machining on several occasions. Design of most of the electronic circuits that I constructed for this project greatly benefited from discussions with Bruno Rütche, who also helped to build some of them.

I would like to thank Dr. Oleg Suleimenov and Dr. T.-K. Ha for helping me to get started with quantum mechanical calculations. Oleg was also helpful with advice regarding various experimental problems. Dr. Kirill Feldman's help in elucidating the nature of contamination by XPS analysis during initial ion source tests is greatly appreciated. I thank Dr. Yuri Podladtchikov for valuable discussions on certain mathematical aspects. Interpretation of the experimental results benefited from the discussions with Professor Terry McMahon and Dr. Eugene Markin from the University of Waterloo and I would like to thank them for their input. I thank Florian Schwandner for translating the Summary to German.

I would like to thank Dr. Dip Banerjee and all my friends and colleagues for helping me to stay in good spirit and to survive this exercise. I thank Sylvia Sopchakova for her support and understanding. Last but not the least, I would like to thank my family and, especially, my mother for encouragement and support. To her I dedicate this dissertation.

Summary

A detailed knowledge of the fundamental manner in which ions and molecules are solvated in aqueous media is required for an understanding of numerous natural processes. Ion-molecule clustering reactions in the gas phase are direct analogs to ionic solvation in a fluid. In addition, the thermochemistry of stepwise solvation reactions can be used directly in the construction of solvation theories and in the development of interaction potentials for molecular dynamics simulations. The high-pressure mass spectrometric technique (HPMS) can provide accurate gas-phase thermochemical data including free energies, enthalpies, and entropies for various ion-molecule reactions. A number of previously identified problems in the use of HPMS to generate accurate thermochemical data have been considered in this attempt to construct an HPMS apparatus that would potentially generate the most accurate thermochemical quantities to date.

We have examined the physical conditions and behavior of ions in a typical HPMS ion source using simple ion/gas theory. It has been shown that molecular flow from an HPMS ion source leads to mass discrimination affecting not only neutral molecules as previously thought, but also ions exiting the ion source. This mass discrimination effect introduces errors in the measured free energy and entropy changes of the reaction, but is easily correctable. Experimental HPMS results corrected for mass discrimination are, on average, in better agreement with results from non-mass discriminating techniques, i.e. ion cyclotron resonance mass spectrometry.

Reactions of stepwise hydration around Cl^-, Br^-, I^- and H^+ ions have been investigated using a pulsed-electron high-pressure mass spectrometer. Results of these experiments strongly suggest that our new construction that concentrated more on temperature measurement and control of the ion source, significantly improved the accuracy of the HPMS measurements. Ion-water clusters of larger size than have been previously observed have been measured with this new spectrometer. The highest hydration steps measured experimentally were n=8 for Cl^-, n=7 for Br^-, n=5 for I^-, and n=7 for H^+. Quantum mechanical calculations using density functional theory (DFT) and large basis sets were performed for each of the systems studied experimentally. Vibrational frequencies obtained from these calculations were used for the computation of the fraction of clusters having energies exceeding dissociation thresholds. These results were used in the selection of appropriate experimental conditions where the fraction of clusters undergoing unimolecular dissociation would be minimized. On one

occasion, the excited fraction data were used to correct the experimentally observed ionic ratios for unimolecular dissociation where the extent of unimolecular dissociation was non-negligible.

Two distinct types of cluster geometry are possible for halide water clusters - interior and surface solvated states. Comparison of experimental results with results from quantum mechanical calculations suggests that surface clusters prevail for the cluster sizes investigated here due to a larger number of surface isomers. The interior structures are also expected to be present as a smaller fraction at elevated temperatures.

There is good agreement between experimental and theoretical trends in the stepwise enthalpies and entropies of hydration for all halide and proton water clusters. In contrast with results from previous experimental investigations, both experimental and theoretical thermodynamic quantities from this study exhibit non-monotonic behavior with increasing cluster size. These trends are interpreted through the competition between the number of additional hydrogen bonds formed at each hydration step and the weakening effect of increasing the cluster size on the ion-solvent interactions. The ion-solvent interactions become weaker with an increasing ionic radius. For Cl^- water clusters, the ion-solvent interaction is stronger than solvent-solvent interaction. The difference between the two types of interaction diminishes with increasing cluster size. The ion-solvent and solvent-solvent interactions are of nearly equal magnitude for iodide. Good agreement between the experimental and density functional theory results lends strong support to the validity of DFT calculations when used as a tool for obtaining structural and thermodynamic information for ion clusters where experimental results are lacking.

Results of comparison of gas-phase differential integrated enthalpies of solvation for halide water clusters with differential values for bulk solvation and non-monotonic dependence of stepwise thermochemical quantities on cluster size lead to the conclusion that properties of small clusters with 7-8 water molecules are still expectedly removed from bulk solvation.

Zusammenfassung

Für das Verständnis einer Vielzahl natürlicher Vorgänge ist ein detailiertes Wissen um die fundamentalen Prozesse notwendig, in denen Ionen und Moleküle in wässrigen Medien solvatisiert werden. Ion-Molekül-Clusterungsreaktionen in der Gasphase sind direkte Analoge zu ionischen Solvatationen in einem Fluid. Hinzu kommt, dass die Thermochemie der schrittweisen Solvatationsreaktionen in der Konstruktion der Solvatationstheorie und der Entwicklung der Wechselwirkungspotentiale für molekulardynamische Simulationen direkt benutzt wird. Hochdruckmassenspektrometrische Techniken (high-pressure mass spectrometry, HPMS) können genaue gasphasen-thermochemische Daten für verschiedene Ion-Molekül-Reaktionen liefern, wie Freie Energien, Enthalpien, und Entropien. Eine Anzahl bereits früher identifizierter potentieller Probleme in der Benutzung von HPMS zur Generierung genauer thermochemischer Daten wurde in diesem Ansatz, eine HPMS-Anlage zu konstruieren welche potentiell die genauesten thermochemischen Werte generieren würde, berücksichtigt.

Wir haben unter Benutzung einfacher Ion/Gas-Theorie die physikalischen Bedingungen und das Verhalten der Ionen in einer typischen Ionenquelle untersucht. Es konnte gezeigt werden, dass der Molekülfluss von einer HPMS-Ionenquelle zur Massendiskriminierung führt, die nicht nur, wie vorher angenommen, neutrale Moleküle betrifft, sondern auch von der Ionenquelle emittierte Ionen. Dieser Massendiskriminierungseffekt erzeugt einen Fehler in der gemessenen Freien Energie und den Entropie-Änderungen der Reaktion, der aber leicht berücksichtigt werden kann. Experimentelle, für Massendiskriminierung korrigierte HPMS-Ergebnisse sind im Durchschnitt mit Resultaten von nicht-massendiskriminierenden Techniken, wie der Ionen-Zyklotron-Resonanz-Massenspektrometrie, in besserer Übereinstimmung.

Reaktionen der schrittweisen Hydratation um Cl^-, Br^-, I^- und H^+ Ionen wurden unter Benutzung eines Gepulste-Elektronen-Hochdruckmassenspektrometers untersucht. Die Ergebnisse dieser Experimente weisen stark darauf hin, dass unsere neue Konstruktion, die mehr auf die Temperaturmessung und Kontrolle der Ionenquelle konzentriert ist, signifikant die Genauigkeit der HPMS-Messungen verbessert. Mit diesem neuen Spektrometer wurden grössere Ion-Wasser-Cluster als bisher beobachtet gemessen. Die höchsten experimentell gemessenen Hydratationsschritte waren n=8 für Cl^-, n=7 für Br^-, n=5 für I^-, und n=7 für H^+. Quantenmechanische Berechnung unter Zuhilfenahme der Dichtenfunktionaltheorie (DFT) und grosser Basissätze wurden für jedes der experimentell untersuchten Systeme durchgeführt. Die von diesen Berechnungen erhalten Schwingungsfrequenzen wurden für die Bestimmung des

Anteiles der Cluster, die Energien über den Dissoziationsgrenzen haben, benutzt. Diese Ergebnisse wurden in der Auswahl der geeigneten experimentellen Bedingungen benutzt, unter denen der Anteil der Clusters minimiert würde, der unimolekular dissoziiert wird. In einem Fall wurden die Daten des angeregten Anteils benutzt, um die experimentell beobachteten Ionenverhältnisse für unimolekulare Dissoziation zu korrigieren, wo das Ausmass der unimolekularen Dissoziation nicht vernachlässigbar war. Zwei distinkte Typen von Clustergeometrien sind für Halid-Wassercluster möglich - innen- und oberflächensolvatisierte Zustände. Der Vergleich der experimentellen Ergebnisse mit Resultaten quantenmechanischer Berechnungen legt nahe, dass Oberflächencluster für von uns untersuchte Clustergrössen aufgrund einer grösseren Anzahl von Oberflächenisomeren vorherrschen. Es ist ebenfalls zu erwarten, dass die innensolvatisierten Strukturen in geringerem Anteil bei erhöhten Temperaturen anzutreffen sind.

Die experimentellen und theoretischen Verhalten stimmen in den schrittweisen Enthalpien und Hydratations-Entropien für alle Halid- und protonierten Wassercluster gut überein. Im Gegensatz zu Ergebnissen von früheren experimentellen Untersuchungen zeigen sowohl experimentelle als auch theoretische thermodynamische Grössen in dieser Studie mit zunehmender Clustergrösse nicht-monotones Verhalten. Dieses Verhalten wird als das Konkurrenzverhalten zwischen der Anzahl der bei jedem Hydratationsschritt geformten zusätzlichen Wasserstoffbindungen und dem schwächendem Effekt der ansteigenden Clustergrösse auf die Ion-Lösungsmittel-Wechselwirkung interpretiert. Die Ion-Lösungsmittel-Wechselwirkungen werden mit ansteigendem Ionenradius schwächer. Für Cl^--Wassercluster ist the die Ion-Lösungsmittel-Wechselwirkung stärker als Lösungsmittel-Lösungsmittel-Wechselwirkungen. Der Unterschied zwischen den zwei Typen von Wechselwirkungen verkleinert sich mit ansteigender Clustergrösse. Die Ion-Lösungsmittel- und Lösungsmittel-Lösungsmittel-Wechselwirkungen sind für Iodid von fast gleicher Grösse. Die gute Übereinstimmung zwischen den experimentellen Ergebnissen und denen der DFT geben der Validität von DFT-Berechnungen starken Rückhalt, wenn diese als Hilfsmittel benutzt werden, um strukturelle und thermodynamische Informationen von Ionenclustern zu erhalten, wo experimentelle Ergebnisse fehlen.

Die Ergebnisse des Vergleichs von Differenzen integrierter Solvationsenthalpien für Halid-Wassercluster in der Gasphase mit jenen für die Gesamtsolvatation sowie die nicht-monotone Abhängigkeit der schrittweisen thermochemischen Grössen auf die Clustergrösse

führen zu dem Schluss, dass die Eigenschaften kleiner Cluster mit 7-8 Wassermolekülen wie erwartet immer noch von denen der Gesamtsolvatation entfernt sind.

Chapter 1. Introduction

The understanding of numerous natural processes such as reactions and properties of fluids in the Earth's crust, reactions in atmospheric and oceanic environments, and biomolecular reactions in the body requires a detailed knowledge of the fundamental manner in which ions and molecules are solvated in aqueous media. Insight into many geochemical processes, especially under hydrothermal conditions, is fundamentally premised on a knowledge of ion-solvent interaction. For example, the changing nature of stable isotope fractionation in high temperature-high pressure aqueous systems is reflected by the changing ion hydration environments. Changing water activity is aqueous electrolyte systems over wide ranges of temperature and pressure results not only from changes in the properties of the bulk solvent (e.g. decrease in density and dielectric constant) but also from related changes in ion hydration. These effects play an important role in defining mineral solubilities and reactions as well as silicate melting phenomena under extreme conditions in the Earth's crust.

In solution it is not possible to measure "naked" ions, however, this is possible in the gas phase and can be carried out in a stepwise manner such that enthalpy and entropy changes may be determined for individual clustering steps when measured over a range of conditions. Ion-molecule clustering reactions in the gas phase are the direct analog to solvation in a fluid. The thermochemistry of stepwise solvation, especially the thermochemistry of the initial solvation steps leading to formation of the first and second solvation shells, and cluster structural information, are used directly in the construction of various theories of solvation [1-3]. Several continuum solvation models have been reviewed in ref. [4]. It is apparent that experimental verification of ionic solvation models and development of improved theories requires well-known and accurate stepwise thermodynamic properties. The desire to obtain thermochemical information for successive clustering reactions has led to a variety of direct and indirect experimental methods. At present, cluster ions formed by expansion of a molecular beam into a low-pressure region comprise the majority of experimental results related to energetics of these cluster ions. These experiments although potentially highly informative, have limited applicability because of ill-defined quantum states of resultant cluster ions. In contrast, clustering reactions under equilibrium conditions produce ions in well-defined quantum states. Historically, the equilibrium determination of thermochemical properties has been limited to studies using ion cyclotron resonance (ICR), Fourier-transform ion cyclotron resonance

(FTICR), and high-pressure mass spectrometric (HPMS) techniques. Of these, only HPMS allows equilibrium studies at variable temperatures, leading to not only the free energy, but also the enthalpy and entropy changes associated with the reaction.

The HPMS technique is not commercially available, and a few "home-made" instruments have been constructed in several laboratories around the world based on pioneering designs of Kebarle [5]. Several problems related to accuracy of the HPMS method have been previously identified. These problems were considered in the attempt to construct an overall HPMS experiment that would lead to potentially the most accurate thermochemical data to date. The newly constructed high-pressure mass spectrometer was used to study the thermochemistry of stepwise hydration of hydrogen and various halides. This choice of species was dictated by the fact that Cl^- and Br^- together with H^+ hydrates are widespread in nature and have been examined previously by several techniques, including HPMS. Addition of iodide to the two other halides allowed characterization of ion-water interactions across this group of homologous elements. Comparison of accurate experimental thermochemical data with results from quantum mechanical calculations allows estimation of the accuracy of these theoretical results. In the case of good agreement, it lends support to the validity of quantum mechanical predictions for structural and thermochemical data pertaining to cluster ions for which no experimental information is available. A combination of experimental and theoretical results provides a wealth of information on the details of stepwise solvation reactions and can be used for a better understanding of the solvation process as a whole.

Chapter 2. Experimental

2.1 Introduction

The pulsed-electron high-pressure mass spectrometric technique was originally developed by Paul Kebarle and coworkers using alpha-particle sources in the 1960's and settled into a successful workable design in the early 1970's with continual improvements in the following years. A comprehensive introduction to HPMS and the history of its development is given in ref. [6]. Our implementation of the HPMS technique explicitly builds upon other successful designs from the groups of Hiraoka [7] and McMahon [8]. Several areas of potential important improvement were identified in these early instruments centered mostly on the ability to unambiguously define the temperature in the reaction chamber. A simple analysis of errors associated with quantities such as the change in enthalpy and entropy that are implicitly derived via derivatives with respect to temperature of measured ionic ratios is given in the following sections. It shows that strict knowledge and control of temperature is required for even reasonably accurate values for these quantities. Kebarle and Hiraoka [9] noted the importance of a sufficiently high vacuum in the source chamber to minimize undesirable competing reactions including collision-induced dissociation (CID). The current implementation of the HPMS technique was developed with these and other concerns in mind.

2.2 Overall experimental layout

Overall layout of the HPMS experiment is shown in Figure 2.1. Samples are prepared in the gas-handling plant by injecting the gas(es) or liquid(s) of interest with a calibrated syringe into a 5L glass mixing bulb containing a carrier gas, generally methane. After sufficient equilibration time, the mixture is allowed to flow through the ion source. Alternatively, liquid samples may be introduced directly into the controlled methane flow with a syringe pump fitted through a septum port. This method is less accurate in terms of known sample concentrations in methane, but is easier to use. Ions are produced in the high-pressure ion source by a 4kV electron beam irradiation. Physical conditions and behavior of ions in the ion source are considered in detail in Chapter 3. The ion source is floated to a potential of 4kV. A small fraction of ions escape from the ion source through an ion exit slit, undergo 4kV acceleration and enter the mass analysis section of the mass spectrometer.

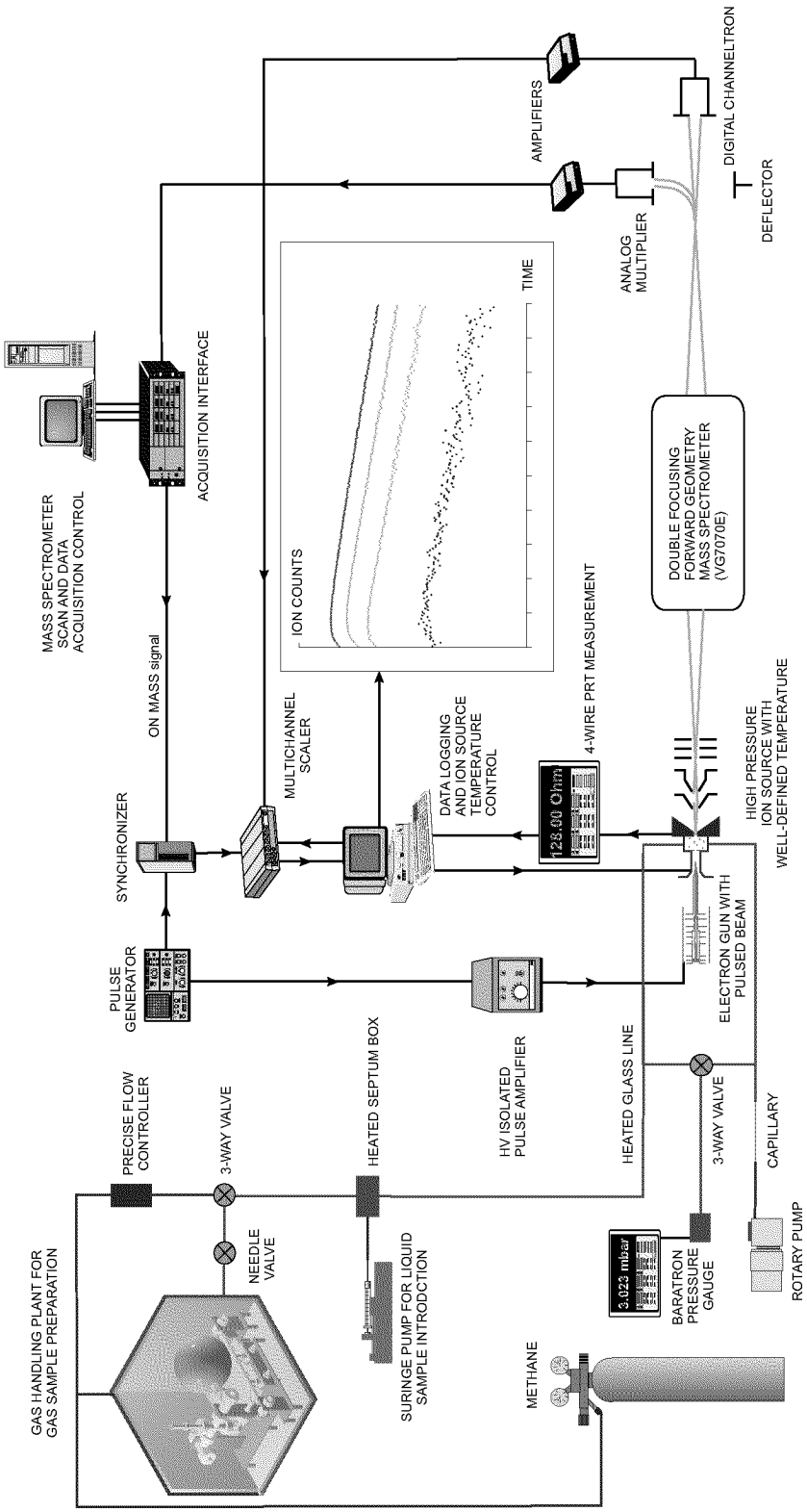

Figure 2.1. Experimental setup.

The ions first enter the electrostatic analyzer (ESA) that performs energy filtering. Following the ESA, the monoenergetic ion beam enters the magnetic field that performs momentum filtering. Ions are detected by electron multipliers. The fitted analog multiplier outputs a signal proportional to the impeding ion current and the digital multiplier outputs pulses proportional to each detected ion, thus allowing for discrete ion counting. The analog multiplier is used to acquire overall mass spectra, whereas the digital multiplier is used in pulsing experiments to follow reaction kinetics and the approach to equilibrium.

Equilibrium studies were performed in the pulsing mode of operation. The electron beam is gated by short pulses from a master pulse generator through an optically isolated battery operated floating pulse amplifier. The electron pulse width is generally kept between 3 and 50μs and the pulse period between 1 and 50ms. Ions are formed after each electron pulse and undergo various chemical reactions in addition to ionic diffusion to the ion source walls whereupon they discharge. Ions that escape from the ion source through the ion exit slit are selectively mass-filtered by the mass analysis section of the mass spectrometer set to monitor a specific mass of interest. Within a preset fixed mass window, only ions of this mass are detected by the digital electron multiplier. The output of the multiplier is fed after preamplification into a multichannel scaler. The multichannel scaler is synchronized with the electron beam pulse via the master pulse generator and records ion counts as a function of time after each pulse. This recording is achieved by counting ions for discrete periods of time (~1-20μs time channels) and performing this operation over a sufficiently large number of channels. The pulsing sequence is performed several thousand times to accumulate enough ion counts in each time channel and for improvement of the signal-to-noise ratio.

The detected ion signal at any time is proportional to the number density of ions of a given mass in the ion source. The concentrations of different ions in the source can be recorded as a function of time to within a machine-dependent factor. If two ions are monitored, the ratio of recorded ion counts will yield the ratio of ion concentrations in the source as a function of time under the assumption that the machine-dependent factor is the same for ions of different masses. This assumption does not always hold and the factor might be mass dependent in certain cases. This aspect is discussed in detail in Chapter 3.

The data collection part of the experiment can be fully automated by synchronizing the ion detection subsystem with the existing mass scan facilities of the mass spectrometer. The mass spectrometer is programmed to monitor a given set of ionic masses over predefined periods of

time during which the multichannel scaler records time profiles for each mass. Details of the construction of various components are given in the following sections and in the Appendix.

2.3 Modifications to the commercial mass spectrometer

The new HPMS apparatus was constructed using an existing VG 7070E spectrometer (previously upgraded from a 7070H) obtained from Fisons Instruments Canada (Micromass). A magnetic sector machine was acquired preferentially over a quadrupole instrument to minimize problems due to mass dependent sensitivity. The 7070E magnetic sector double-focusing mass spectrometer is of EB geometry and although having reasonably high ion sensitivity, was not adequate for the HPMS experiments and was subsequently modified. Modifications were made to the overall pumping speed in the source housing, some ion optics, and the ion detection system.

The commercial VG 7070E spectrometer is pumped by two Edwards diffusion pumps in the source and analyzer regions, respectively. The original Edwards 160/700M source diffusion pump (700 L/s of N2) is connected to the source chamber by a 142 mm ID stainless steel tube. Because of the high pressures involved with the HPMS experiment it was necessary to add a Leybold TMP1000 (1150 L/s of N_2) ceramic bearing turbo pump mounted directly above the ion-exit slit in a vertically inverted position. The 250mm CF pump flange from the turbo pump was mounted onto a thick stainless steel adapter connected between a mating 250mm CF flange and a 152x102 mm rectangular slot cut into the top of the commercial source chamber. The conservation of cross sectional area in this adapter has minimized conductance losses due to the adapter. The original source flange was replaced by a source flange assembly that also incorporates an electron gun mount and appropriate electron gun housing chamber. The original source chamber was expanded to accommodate this larger assembly. The electron gun chamber is differentially pumped with an Edwards 63/150M diffusion pump (135 L/s of N_2). The turbo pump is only used during the course of experimental measurements, and the ultimate vacuum of this system is better than $4x10^{-7}$mbar after an appropriate bakeout. Several large (Edwards E2M40, 2xE2M28) roughing pumps were added to the source high vacuum pumps. In this configuration, there is differential pumping of the analyzer, electron gun, and ion source regions. As such, a vacuum of better than $5x10^{-7}$mbar is maintained during an experiment in the analyzer and $5x10^{-6}$mbar in the electron gun regions leading to a pressure in the source chamber not exceeding $5x10^{-5}$mbar for the source pressures employed to date.

It was found that the original Y (horizontal plane perpendicular to ion beam) and Z

(vertical plane) focusing and deflection was responsible for a loss in ion sensitivity due to losses in the region prior to the ESA. We have added a series of precision-machined stainless steel plate lenses in the first field-free region prior to the ESA and have achieved increased ion sensitivity by nearly a factor of 2. Voltages for these additional plates are drawn from a modified ESA voltage supply unit. In addition, the possibility of digital signal acquisition was added by expanding the ion detection region and placing a Galileo Channeltron 4870V electron multiplier at exactly the same position as the existing analog conventional electron multiplier.

2.4 High pressure ion source and electron gun

The HPMS ion source consists of an electron gun mounted coaxially to the produced ion beam and the high-pressure source itself, and is shown schematically in Figure 2.2. Because the VG 7070E mass spectrometer is capable of operating with 6kV of ion acceleration potential, the electron gun was designed to operate with the filament floated at -12 kV. This large potential would be required if 6kV of electron acceleration was to be used for the highest ion acceleration (negative ions). Design of the electron gun was based on previous versions of electron guns from Kebarle [6], Szulejko and McMahon [10], and by examination of 3-4kV cathode ray tubes used in a variety of well-focused Hewlett Packard oscilloscopes. The initial design was simulated using the ion optics software package SIMION and the final version of the electron gun capable of providing 2-6kV of acceleration for positive ions (starting at ground potential) or negative ions (starting at a potential below ground) was constructed. The electron gun was powered by a custom built filament power supply capable of floating to ± 15kV and a precision high voltage divider built as part of this project and detailed in Appendix A. Conventional VG 7070E filaments were used as obtained from VG Micromass or Haltech Inc. Initial tests of the electron gun for optimum voltage characteristics were performed using a phosphor screen obtained from Kimball Physics Inc. and showed that the resultant electron beam was stable and relatively tightly focused. The position of the electron gun can be clearly seen in Figure 2.2. The electron gun is fixed to a stainless steel mount (4) that is electrically isolated by 4 ceramic spacers from the electron gun filament mount plate (7) and from the electron gun feedthrough flange (1) by a 25mm machineable ceramic (MACOR) mount. The electron gun was mounted in-line with the high-pressure source as guided through the electron gun housing (2) through a ceramic guide (18) that also serves as a differential pumping aperture. Voltages were provided by high-voltage (20kV) feedthroughs mounted on the main electron gun flange (1).

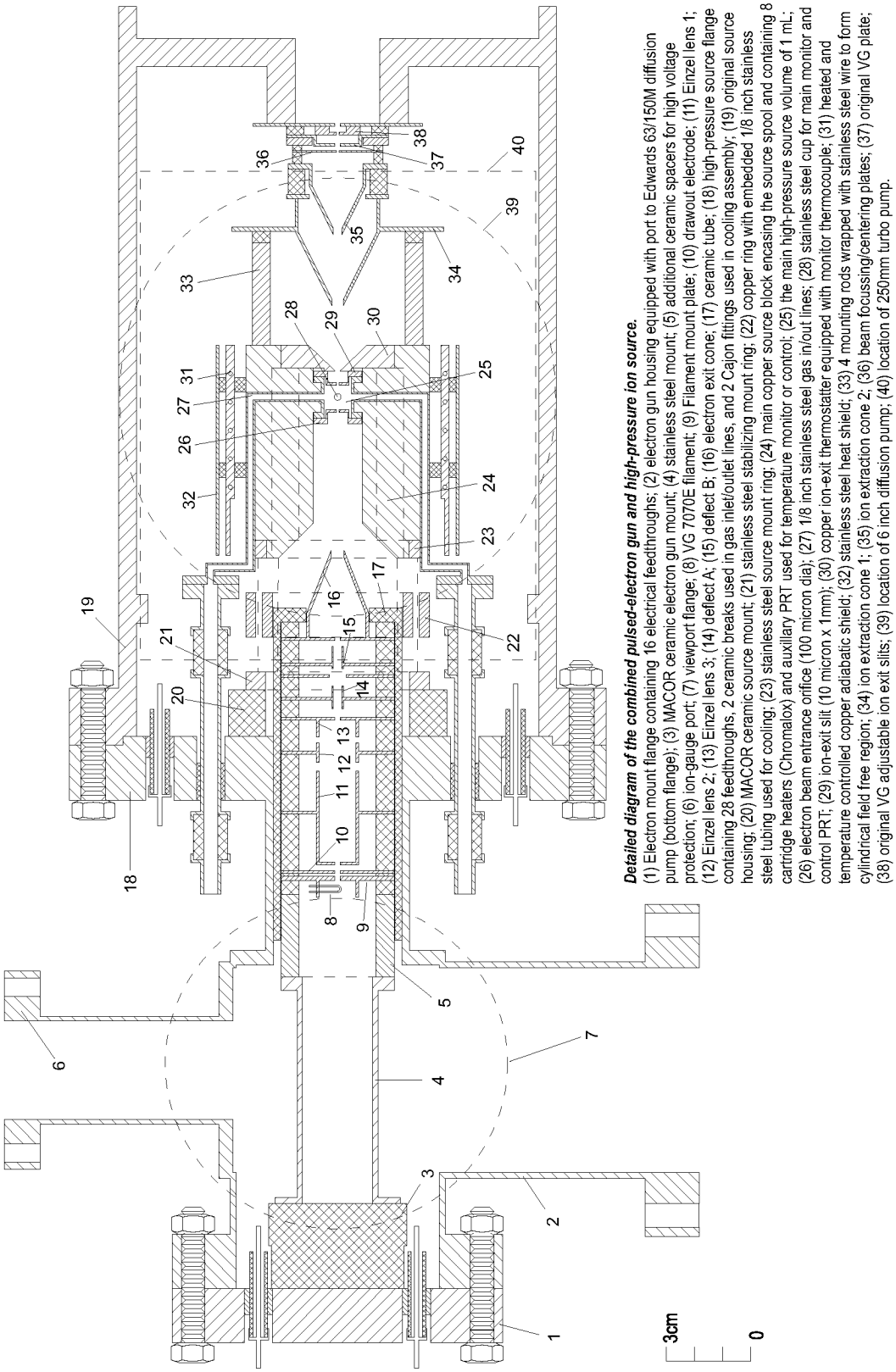

Detailed diagram of the combined pulsed-electron gun and high-pressure ion source. (1) Electron mount flange containing 16 electrical feedthroughs; (2) electron gun housing equipped with port to Edwards 63/150M diffusion pump (bottom flange); (3) MACOR ceramic electron gun mount; (4) stainless steel mount; (5) additional ceramic spacers for high voltage protection; (6) ion-gauge port; (7) viewport flange; (8) VG 7070E filament; (9) Filament mount plate; (10) drawout electrode; (11) Einzel lens 1; (12) Einzel lens 2; (13) Einzel lens 3; (14) deflect A; (15) deflect B; (16) electron exit cone; (17) ceramic tube; (18) high-pressure source flange containing 28 feedthroughs, 2 ceramic breaks used in gas inlet/outlet lines, and 2 Cajon fittings used in cooling assembly; (19) original source housing; (20) MACOR ceramic source mount; (21) stainless steel stabilizing mount ring; (22) copper ring with embedded 1/8 inch stainless steel tubing used for cooling; (23) stainless steel source mount ring; (24) main copper source block encasing the source spool and containing 8 cartridge heaters (Chromalox) and auxillary PRT used for temperature monitor or control; (25) the main high-pressure source volume of 1 mL; (26) electron beam entrance orifice (100 micron dia); (27) 1/8 inch stainless steel gas in/out lines; (28) stainless steel cup for main monitor and control PRT; (29) ion-exit slit (10 micron x 1mm); (30) copper ion-exit thermostatter equipped with monitor thermocouple; (31) heated and temperature controlled copper adiabatic shield; (32) stainless steel heat shield; (33) 4 mounting rods wrapped with stainless steel wire to form cylindrical field free region; (34) ion extraction cone 1; (35) ion extraction cone 2; (36) beam focussing/centering plates; (37) original VG plate; (38) original VG adjustable ion exit slits; (39) location of 6 inch diffusion pump; (40) location of 250mm turbo pump.

Figure 2.2. HPMS ion source and electron gun.

The electron gun and its housing were designed such that the filament could be replaced without completely removing the high-pressure source from the mass spectrometer or disassembling the electron gun. The electron gun housing was equipped with a viewport for visual confirmation of filament power or check for potential high voltage breakdown. The electron beam was shielded from magnetic fields by 0.1 mm thick mu-foil (Magnetic Shield Corp.) wrapped in 3 layers around the ceramic tube (17), electron exit cone (16), and inside the cylindrical channel located in the center of the copper source block (24). No observable effect of the mass spectrometer magnet on the electron beam focusing and deflection conditions was detected. This is an important requirement because the number of electrons entering the ion source after each electron beam pulse must be independent of the mass monitored by the mass spectrometer.

As outlined previously, one of the main goals during the construction of this new HPMS ion source was to minimize errors due to temperature instability or lack of precision in its measurement. As such, the design was based partly on successful high-temperature calorimeters that maintain temperature stability to better than 10^{-3}K [11]. The central component of the ion source is the stainless steel source "spool" (25) that was constructed from 10mm OD and 0.5mm wall thickness tubing and had an internal volume of approximately 1cm^3. A thin-walled 2mm ID stainless steel cup inset into the spool was fitted to house the main platinum resistance thermometer (PRT). Two 1/8" stainless steel gas inlet and outlet lines were also welded to the source spool as shown in Figure 2.3. This internal ion source chamber is sealed using a scaled-down version of the NW16 CF flange and gold-plated copper gaskets. Ion exit and electron entrance apertures were constructed using standard stainless steel orifice (100μm diameter for electron entrance) and slit (10μm wide for ion exit), obtained from Melles Griot, that were welded onto the source flanges. The entire source spool sits tightly encased in a large nickel-plated copper source block machined to an extremely high tolerance so as to maintain good thermal contact between the source spool and the block. The gas lines are sandwiched tightly into the large copper source block for temperature pre-equilibration and are, in turn, connected to high voltage ceramic breaks (6kV, Kurt Lesker Company) and to 1/4" high-voltage stainless steel isolated feedthroughs (12kV, Kurt Lesker Company) that were welded to the source flange (18). Silver solder used in the construction of the ceramic breaks limited experimentally usable high temperatures to approximately 600°C. The thin source spool, large copper block, and inset PRT element were all designed to minimize temperature gradients near the source, provide temperature uniformity, and ultimately provide knowledge of the temperature of the reaction

during the course of the experimental measurements. The copper block was fitted with 8 cartridge heaters (Chromalox, CIR type) and various control and monitoring (PRT and thermocouple) temperature elements. A thick copper ion-exit plate (30) was used to maintain thermal contact near the ion-exit region and was fitted with a monitor thermocouple. The entire source block was enveloped by a 4mm thick nickel-plated adiabatic copper shield embedded with a 1mm OD Omegaclad metal-sheathed thermocouple wire (Omega Engineering) used as a heater. The adiabatic shield had an embedded monitor thermocouple that was used together with a Eurotherm temperature controller to maintain a preset temperature. The shield was located such as to give a 5mm gap between the source block and the shield. This shield, in turn, was surrounded by an unheated nickel-plated stainless steel tube used as an outer heat shield. This combination of adiabatic shield and outer heat shield minimizes radial radiative heat losses and provides excellent temperature stability and uniformity. Even when no heating or temperature control of the adiabatic shield was used, the temperature stability was found to be no worse than 0.02°C over 1 hour throughout the entire temperature range used (-45°C to 540°C). For the most common temperature range (30°C to 200°C) the stability was better than 0.001°C over 1 hour.

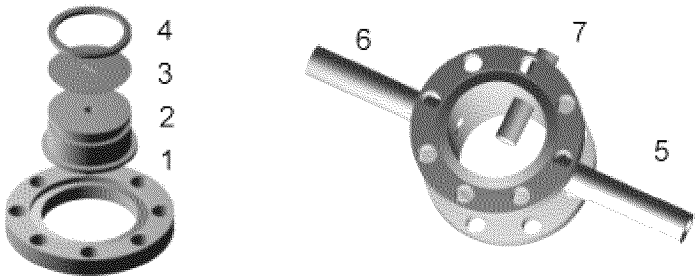

Figure 2.3. Ion source spool and flange. Ion exit and electron entrance flanges are of identical design. Height of cylinder (2) welded to the flange (1) determines the volume of ion source. Standard foil with circular or rectangular orifice (3) is sandwiched between cylinder (2) and washer (4) and welded along the outside edge. Gas inlet and outlet lines (5,6) and main PRT cup (7) are welded to the source spool. The PRT cup has the end inside the source blanked.

Ions exit the high-pressure source and enter the cylindrically shaped field-free region constructed using 4 stainless steel rods (33) wrapped concentrically using 0.8mm stainless steel wire with spacing of 3-4mm between the loops. The first ion extraction cone (mirror polished to reduce radiative heat losses) incorporating a 4mm opening was fixed to the source via 4

stainless steel rods and was electrically isolated using ceramic spacers. A second cone containing a 3mm opening was mounted between this and the ion focus and deflection plates (36,37). The VG 7070E adjustable source slit (38) was retained although normal operation was achieved when the slit was fully open that yielded an instrument resolution of approximately 500 to 1000. The entire source is mounted onto an original VG 7070E source flange using a stabilizing stainless steel ring source mount assembly (21,23) held together by 4 stainless steel rods and designed to minimize stress on the main ceramic isolating mount (20). This source mount was fitted with a cooling assembly constructed using 1/8" stainless steel tubing sandwiched inside in a copper ring and tightly fixed to 4 rods on the source mount. The tubing is electrically isolated from the flange using two 1/4" Cajon glass-to-metal adapters. The ion source can be easily cooled to -100°C by flowing cold nitrogen gas through the cooling assembly. The gas is cooled by passing it through a copper coil immersed in liquid nitrogen. The source flange is equipped in total with 28 electrical feedthroughs in addition to two high-voltage gas feedthroughs connected to the gas inlet and outlet lines and two Cajon fittings for the cooling assembly.

A Minco S274PD type PRT was used for ion source temperature measurement. These PRT's are encased in a ceramic capsule 2mm in diameter and 10mm long. A 4-wire resistance measurement was performed for temperature determination. A 4-wire measurement ensures that lead resistances cancel. Nichrome wire was used for the lead extensions that were spot-welded to the original platinum PRT leads 8mm away from the PRT body. Nichrome has a thermal conductivity 2.5 times lower than platinum and 30 times lower than that of copper. This choice of wire was dictated by the desire to reduce temperature measurement errors that might occur when using wires with higher thermal conductivity. Heat may be pumped away from the light platinum sensor in the PRT through lead wires if they are at a temperature lower than the PRT when lead extensions have a sufficiently high thermal conductivity. Approximately 12-15cm of the Nichrome lead extensions were placed in 4-hole ceramic capillaries and were mounted in the copper block (24) to ensure good thermal contact with the block.

Prior to being mounted in the ion source, the PRT was calibrated against a NIST traceable secondary reference standard PRT in a specially designed calibration vessel. The main part of the vessel was a copper cylinder 25mm in diameter and 150mm long. The secondary reference standard PRT was placed in the channel in the center of the cylinder and the source PRT was placed in another channel immediately adjacent to it. Metal-sheathed Omegaclad thermocouple wire was wrapped around the cylinder and was used as a heater. The cylinder was placed inside

a polished stainless-steel tube that served as a heat shield, similar to our ion source design. The whole assembly was placed inside an evacuated stainless steel manifold. The mounting of the copper cylinder inside the shield and the shield inside the manifold was done using sharpened pins to have only point contacts to reduce conductive heat losses. The calibration was performed over the temperature range 30°C to 470°C and PRT coefficients were calculated following the NIST guidelines given in ref. [12]. For temperatures below 30°C the calibration was extrapolated. According to ref. [12], most PRT's have an error of a few mK when the calibration is extrapolated in this manner which is negligible in our case. The accuracy of the present calibration was estimated to be 0.05°C. The calibration of the secondary reference standard PRT was rechecked by an external calibration laboratory after the calibration of the ion source PRT and was found to be consistent with its original calibration.

The 4-wire resistance measurement of the source PRT was performed by a Keithley 2001 Multimeter floated at the ion source potential and powered through isolation transformers. The data were sent to a monitoring computer via an optically isolated IEEE bus. The computer handled resistance to temperature conversion and implemented a PID algorithm for the ion source temperature control. Control of the ion source heaters was of the time-proportioning type. The computer outputs pulses of variable width to control the heater power. The pulses were sent via a fiber-optic link to a solid state relay, floated at the ion source potential, that switched the source heaters on and off.

2.5 Sample introduction system and pressure measurement

The gas handling plant (GHP) consisted of a stainless steel manifold with all-metal valves and a 5L glass bulb fitted with a septum inlet port. The exact volume of the bulb was calibrated using water. The manifold and bulb were mounted inside a uniformly heated box. The temperature inside the GHP was kept at 140°C and was controlled by a temperature controller using a thermocouple sensor. The pressure in the GHP was measured using a 1000 mbar MKS Baratron 628A absolute pressure transducer.

Gas lines from the GHP to the ion source and from the ion source to the outlet rotary pump were made using 2m long glass tubes having a 9mm inside diameter. Small segments of the lines immediately adjacent to the source (~60cm length) were made from glass tubes having a 4mm inside diameter. This length of glass tubes was chosen to avoid electrical breakdown through the gas from the ion source to ground when maintaining low ion source pressures. These glass lines were designed to operate at the ion source potentials of up to 6kV. For

comparison, HPMS machines in the laboratory of Kebarle had 60cm long glass lines for ion source operating voltages of up to 2kV [6]. The glass lines were kept at 140°C by temperature controllers. The glass tubes were connected together using stainless steel or teflon Swagelok-type unions with teflon ferrules. The teflon unions were drilled through as to minimize the surface area of teflon exposed to the gas flow. The flow from the GHP was regulated by means of a Hoke MilliMite 1300 stainless steel metering valve. When the syringe pump was used for sample introduction, the methane flow was controlled by an MKS 1679A Mass-Flo flow controller.

The pressure was measured at the far ends of the 2m glass lines by a 10 mbar MKS Baratron 628A absolute pressure transducer. The Baratron could monitor either inlet or outlet line pressures and was switched by means of a Hoke SelectoMite 7165 stainless steel 3-way valve. Because we were not able to measure the pressure directly in the ion source, we ensured that the inlet and outlet gas lines were identical. In addition, the combined conductance of the gas lines from the points of pressure measurement to the ion source and conductance of the ion exit and electron entrance slits in the ion source was measured as a function of source temperature. This was achieved by alternatively closing off either inlet or outlet line and measuring the gas flow through the ion source using a calibrated flow meter and monitoring pressures at the ends of both lines. With this arrangement, one of the pressures will be equal to the pressure inside the ion source. The obtained calibration data was used to calculate the corresponding pressure in the ion source in the normal flow-through configuration from measured pressures at the ends of the inlet and outlet lines. The accuracy of this conductance calibration was found to be no worse than 0.05 mbar in ion source pressure. The partial pressure of a sample in the ion source was calculated from the known GHP total bulb volume, the volume of injected sample, the pressure and temperature of methane in the GHP before injection, and the total pressure inside the source. When the syringe pump was used, the partial pressure was calculated from the known syringe pump injection rate, the known methane flow rate, and the total pressure inside the ion source. If partial pressures of neutral reactants in the ion source are known and the ratios of ionic concentrations in the source are determined from ionic profiles, equilibrium constants are easily calculated. The exact expression for the equilibrium constant depends on the specific reaction studied and will be given in Chapter 4. Once the equilibrium constants for a reaction at several temperatures are determined, the enthalpy and entropy changes for the reaction can be calculated from plots of the logarithm of equilibrium constant against reciprocal temperature, so-called van't Hoff plots, using the

following equations:

$$\Delta G^\circ = -RT \ln K \tag{2.1}$$

$$\Delta G^\circ = \Delta H^\circ - T\Delta S^\circ \tag{2.2}$$

$$\ln K = -\frac{\Delta H^\circ}{R}\left(\frac{1}{T}\right) + \frac{\Delta S^\circ}{R} \tag{2.3}$$

If the van't Hoff plots exhibit linearity, as is the case for studied clustering reactions, then the enthalpy and entropy changes are easily calculated from the slopes and y-intercepts.

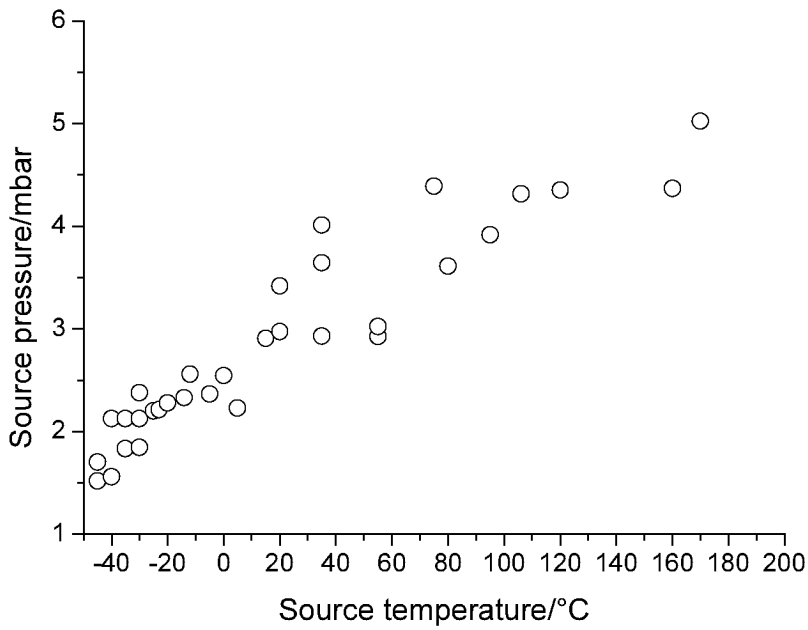

Figure 2.4. Experimentally used ion source pressures at different ion source temperatures.

It is important to elaborate on the ion source pressure range for best operation of this technique. Equilibrium HPMS studies require that ion residence times in the ion source are longer than equilibrium establishment times. This is achieved by trapping ions in the ion source with sufficiently high pressures of a carrier/buffer gas. However, if the ion source pressures are too high, then acceleration of the ions following escape from the ion source might lead to collisional dissociation through collisions with neutral gas molecules that have also escaped

from the ion source. Acceleration voltages as low as 1-3V may supply enough energy for collisional breakup. To remedy this situation, the pressures in the ion source at any given source temperature should be kept sufficiently low, yet high enough to observe equilibrium. As a general rule, the gas number density in the ion source was kept constant throughout the experimental temperature range. This meant having progressively lower pressures in the ion source at lower temperatures. Figure 2.4 shows our experimentally used pressures at different temperatures. With this HPMS instrument's gas lines and source slits conductances, methane flow rates in the range 1.5-5sccm were required to realize such pressures.

Chapter 3. Physical Conditions in the HPMS Ion Source

This chapter comprises a co-authored paper with Jamey Hovey that has been accepted for publication in the International Journal of Mass Spectrometry and entitled "On Mass Discrimination in High Pressure Mass Spectrometry: Potential Errors in Measurements Leading to Absolute Ion Abundances".

Abstract

Various thermochemical calculations require that mass spectrometric measurements provide absolute values for ratios of ion abundances. High-pressure mass spectrometric measurements normally employ a small slit between a high-pressure reaction chamber and the ion detection vacuum envelope. It is shown that the sampling of ions through a small slit depends classically on the square root of mass when flow through the slit can be characterized as molecular. Calculations that require ion intensity or abundance ratios, such as equilibrium constants or standard Gibbs energies of reaction, need to consider this mass effect. The nature of mass discrimination in high-pressure and stationary afterglow experiments has been characterized for traditional ion sampling through a thin slit and also for the various ion-diffusion processes present in these experiments. It has been shown that thermodynamic values obtained considering this effect are in better agreement with other measurements free of mass discrimination.

3.1 Introduction

Measurements leading to the thermodynamic properties of gas-phase ions are extremely important tools for the investigation of a variety of processes including ionic solvation, organic reaction mechanisms, and interstellar processes, to name a few [13]. Techniques that can lead to well-defined quantum and thermodynamic states are particularly useful in this regard. Pulsed-electron high-pressure mass spectrometry is one such technique whereby experimental conditions are well favored for thermodynamic measurements of a well-defined thermodynamic state for the system under investigation.

While several techniques can be used to determine gas-phase reaction energy profiles, only a few techniques (for example high-pressure mass spectrometry (HPMS) and ion-cyclotron resonance (ICR) mass spectrometry) lead directly to equilibrium distributions and hence the change in Gibbs free energy for these reactions. For experiments investigated by HPMS, it is believed that because of the high number density of neutral gas particles, a meaningful thermodynamic state, temperature, pressure, and thus reaction profile are defined. For both of these techniques, the change in standard state Gibbs energy $\Delta G°$ can be written

$$\Delta G° = -RT \ln K_{eq} \tag{3.1}$$

where K_{eq} is the equilibrium constant for the reaction under investigation. A typical reaction (in this case for proton transfer) can be written

$$B_1H^+ + B_2 = B_2H^+ + B_1 \tag{3.2}$$

where neutral species are designated as B_n. The thermodynamic equilibrium constant is written in terms of the activities of each participating species:

$$K_{eq} = \frac{a_{B_2H^+} \cdot a_{B_1}}{a_{B_1H^+} \cdot a_{B_2}} \tag{3.3}$$

In terms of gas-phase experiments at relatively low pressure, we can assume that the gases and ions behave as perfect gases. As such, after sufficient reaction time the thermodynamic equilibrium constant may be represented by:

$$K_{eq} = \frac{I_{B_2H^+} \cdot p_{B_1}}{I_{B_1H^+} \cdot p_{B_2}} \tag{3.4}$$

where I represents ion abundances as measured experimentally, and p represents partial pressures of neutral species, where both quantities are used to approximate number densities or absolute concentrations. K_{eq} is a function only of temperature when the various concentrations are represented by partial pressures (perfect gases) and as such it is assumed that the ratio of ionic abundances equals the ratio of partial pressures of the ions.

The enthalpy of a reaction is related by the temperature dependence of the equilibrium constant:

$$\left(\frac{\partial \ln K_{eq}}{\partial T} \right)_p = \frac{\partial H°}{RT^2} \tag{3.5}$$

Variation of temperature in certain mass spectrometric experiments allow calculation of $\Delta H°$

and subsequently $\Delta S°$ via

$$\left(\frac{\partial \Delta G°}{\partial T}\right)_p = -\Delta S° \tag{3.6}$$

HPMS experiments normally use this derivative technique to determine the associated enthalpies for reactions of type given by Eq. (3.3), whereas ICR experiments normally rely on an extra thermodynamic assumption of the entropy change to allow calculation of the change in enthalpy.

A high ion source pressure in the HPMS experiment favors equilibrium (when appropriate for a given set of reaction conditions) as opposed to long ion-trapping times favoring reaction and equilibrium during the ICR experiment. Whereas ICR allows all ions to be sampled with near identical efficiency [14] because of the *in situ* nature of ICR, in HPMS and other forms of mass spectrometry, ions are sampled through a small orifice or slit [6], and are often subject to external or internal (space-charge) fields that may alter the "detection efficiency" of the sample. It is in these cases where potential problems associated with mass discrimination occur.

Most techniques involving mass spectrometry (especially those employing quadrupole mass filters) have considered mass discrimination during ion sampling. However, even though implied in early discussions, it appears that a quantitative discussion of ionic mass discrimination during sampling (prior to the mass discrimination inherent in detection systems) in HPMS and other related techniques, has largely been ignored. Grimsrud and coworkers [15-17], however, have considered the ion sampling process in HPMS in some detail. They have identified several sources of errors including the discrimination due to the preferential depletion of lighter mass neutral molecules in the HPMS experiment [15, 16].

3.2 Theory

3.2.1 Brief background

Various authors have presented accounts of the HPMS experiment but none as complete as the main developer Kebarle [6]. It is important here to consider the nature of the HPMS experiment including the average dimensions and conditions existing inside a typical reaction chamber.

An HPMS experiment consists of a short electron pulse acting on a mixture of a small amount of reactant in a large excess of bath gas. The bath gas is present in the HPMS experiment as a thermalizer (ions and electrons), to aid in the ionization process and as a source

for 3rd body collisions. Following a short electron pulse, the conditions inside the HPMS source can be described as an electrical plasma containing electrons, positive ions and negative ions. A detailed description of this condition has been presented by Kebarle [6] and by Hiraoka [18]. There is a wealth of information [19] that has been published regarding mobilities of ions and electrons in neutral gases, that can be used to directly determine the conditions and potential mass discrimination of HPMS and stationary afterglow experiments of which HPMS is an example.

A discussion of mass discrimination must first begin by consideration of the energy or velocity distribution of ions and gases. More than 100 years ago Graham [20] noted that the escape of gases through small orifices was a function of the gas density (hence pressure) and on the square root of the mass of the gas. Graham's law can be expressed:

$$\frac{f_1}{f_2} = \left(\frac{M_2}{M_1}\right)^{1/2} \tag{3.7}$$

where f is the flux of gas leaving the orifice and M_i are the respective molecular weights of the gases.

A convenient starting point in the discussion of gaseous physical properties rests in the kinetic theory of gases [21]. In the absence of any external fields, the Maxwellian velocity distribution can be written:

$$\frac{dn}{dv} = \frac{2N}{\sqrt{\pi}}\left(\frac{m}{2kT}\right)^{3/2} v^2 \exp\left(\frac{mv^2}{2kT}\right) \tag{3.8}$$

that results in an average particle velocity $\bar{v}$:

$$\bar{v} = \left(\frac{8kT}{\pi m}\right)^{1/2} \tag{3.9}$$

where n is the number of particles with mass m, v is the velocity, N is the total number of particles, k is Boltzmann's constant, and T is the absolute temperature. Eq. (3.9) is an important result as it immediately shows the dependence of the gas velocity on the square root of mass that appears in a variety of gaseous flow equations.

3.2.2 Stationary afterglow

Although most stationary afterglow experiments have been replaced by the more versatile flowing afterglow experiments, there are a variety of results pertaining to static afterglow experiments of which HPMS can be considered. The characterization of an afterglow as having

a substantial number of ionized particles following initial ionization is true in the HPMS experiment.

We begin by considering Fick's law of diffusion even though it is inherently based on a system of identical particles interacting only through short-lived two-body collisions [22]. Because the concentration of ions is normally significantly less than the neutral bath gas, the individual ions can be considered to be interacting only with neutral gas and as such Fick's law should apply. Fick's law can be written for the diffusion of a gas in the absence of any externally applied fields and shall be denoted as free diffusion:

$$\Gamma_i = -D_i \nabla n_i \tag{3.10}$$

where Γ_i is the diffusion current density that is proportional to the free diffusion coefficient D_i multiplied by the gradient and concentration of ions n_i. In the presence of an electric field, Γ_i becomes the sum of free diffusion (driven by a concentration gradient) and field-induced diffusion (driven by a permanent or induced electric field) for particles of type *i* by:

$$\Gamma_i = -D_i \nabla n_i + n_i \mu_i E \tag{3.11}$$

where $D_i \nabla n_i$ is the contribution to diffusion due to the concentration gradient, and $n_i \mu_i E$ is the contribution due to the field-induced mobility of the particle and μ_i is the corresponding ionic mobility.

In a stationary afterglow or HPMS experiment characterized by an ionization pulse for sufficient ion density, the electrical plasma thereby created is characterized initially by ambipolar diffusion of positive ions and electrons. In the special case of only one positive ion, or of several positive ions with the same ionic mobility, the fluxes can be written:

$$\Gamma^+ = -D^+ \nabla n^+ + n^+ \mu^+ E \tag{3.12}$$

$$\Gamma_e = -D_e \nabla n_e - n_e \mu_e E \tag{3.13}$$

and after appropriate algebraic rearrangement considering that fluxes of positive ions and electrons are approximately equal [22], and elimination of the electric field E leads to the standard ambipolar diffusion equation:

$$\Gamma = -D_a \nabla n \tag{3.14}$$

where

$$D_a = \frac{D^+ \mu_e + D_e \mu^+}{\mu_e + \mu^+} \tag{3.15}$$

The ionic mobilities can be substituted into this ambipolar diffusion equation (for a Maxwellian distribution and equal electron and ion temperatures):

$$D = \frac{\mu kT}{e} \tag{3.16}$$

and therefore

$$\frac{D^+}{\mu^+} = \frac{D_e}{\mu_e} = \frac{kT}{e} \tag{3.17}$$

then

$$D_a = \frac{2D^+\mu_e}{\mu_e + \mu^+} \approx 2D^+ \tag{3.18}$$

and D_a is approximately equal to D^+ because of the very large difference between electron and ion mobilities: $\mu_e \gg \mu^+$. Ambipolar electron-ion diffusion is, however, only valid whilst an electrical plasma is maintained (the case where $\left|n^+ - n_e\right| \ll n_e$).

In an experiment with several long-lived ions (as is normally the case for HPMS experiments) and electrons, for the case of 2 positive ions (denoted by subscripts 1 and 2), we can write:

$$\Gamma_1^+ = -D_1^+\nabla n_1^+ + n_1^+\mu_1^+ E \tag{3.19}$$

$$\Gamma_2^+ = -D_2^+\nabla n_2^+ + n_2^+\mu_2^+ E \tag{3.20}$$

$$\Gamma_e = -D_e\nabla n_e - n_e\mu_e E \tag{3.21}$$

at sufficiently high electron densities, the ion fluxes are controlled by the ambipolar diffusion coefficients as discussed above. In a similar fashion, the electron density can be related to an effective diffusion coefficient D^* by:

$$\Gamma_e = D^*\nabla n_1 \tag{3.22}$$

where

$$D^* = \frac{D_e\left(\mu_1 + K\mu_2\right) + \mu_e\left(D_1^+ + KD_2^+\right)}{\mu_1 + K\mu_2 + \mu_e} \tag{3.23}$$

which is exactly analogous to a weighted ambipolar diffusion coefficient given by Eq. (3.15) if the two positive ion concentrations can be related arbitrarily by $K = n_1 / n_2$ (as can be assumed at some point in an equilibrium reaction) and that if only two cations are present,

$$\Gamma_e = \Gamma_1^+ + \Gamma_2^+ \tag{3.24}$$

noting that D^* reduces to D_a when $n_1 = n_2$.

At sufficiently long times following the finite ionization pulse or event, the diffusion of ionic species changes from cation-electron ambipolar to cation-anion ambipolar diffusion [23] or to free diffusion if the concentrations of ionic species are too low. It is of primary importance here to consider the flux of ions reaching the wall as a function of experimental conditions. Following Massey [24] a simple afterglow experiment can be characterized by the time-dependent concentrations of the species. Assuming that HPMS will ordinarily have a minimum of 2 positive ions (concentrations designated by n_1 and n_2), some number of metastable species n_m in early stages, and some number of negative ions ($n\_$) in later stages, we can derive region specific formulae.

3.2.3 Region I: Ionization and cation-electron ambipolar diffusion

A simple plot defining each of the three main regions in a typical HPMS (at high ionization) or stationary afterglow is given in Figure 3.1. Region I is characterized by initial ionization and decay of metastable species leading to cation-electron ambipolar diffusion. It is sufficient here to start with two ionic species present initially and not reacting with each other to any great extent. Time dependent diffusion equations can be written for the two ionic species in the absence of sources or sinks for these species:

$$\frac{\partial n_1(r,t)}{\partial t} = -D_{1a}\nabla^2 n_1(r,t) \tag{3.25}$$

$$\frac{\partial n_2(r,t)}{\partial t} = -D_{2a}\nabla^2 n_2(r,t) \tag{3.26}$$

Negative ion diffusion to the walls is hindered because of the self-field created by positive ions and electrons, and ionic distributions here are assumed free of metastables. These equations can be solved easily for the case of a spherical geometry (for example in our mass spectrometer we have a slightly complicated cylindrical shape that is easily approximated to a sphere with the same characteristic length as the cylinder). For a spherically symmetric ionic concentration distribution, we can write [25]:

$$\frac{dn(r,t)}{dt} = \frac{D_a}{r^2}\frac{\partial}{\partial r}\left[r^2 \frac{\partial r}{\partial n(r,t)}\right] \tag{3.27}$$

that can be solved (with regard to the boundary condition that ion intensity should vanish at the

walls) to yield:

$$n(r,t) = c_2 \exp\left(D_a c_1 t\right) \sin\left(\sqrt{-c_1} r\right) / r \tag{3.28}$$

where c_1 and c_2 are constants (determined by the boundary conditions) and we take here only the lowest (fundamental) solution of the equation (noting that periodic solutions in multiples of π correspond to higher modes of diffusion that decay more rapidly than the fundamental mode and can for the most part be ignored). Since this equation describes most regions of ionic diffusion, it is extremely informative to show the solution of this equation in Figure 3.2. The solution of this equation is the ion density maximum of the center node representing the center of the spherically symmetric ionic distribution. The ionic intensity is seen to decay exponentially with time (becoming a flatter sine curve) and in addition the approach to higher modes of diffusion are shown. It can be shown that the ambipolar diffusion coefficients D_a and time allowed for diffusion have the same effect on this plot although appropriate boundary conditions would provide quantitative values for the various profiles. Figure 3.2 thus depicts the qualitative shape for all time-dependent ionic distributions to be discussed in following sections.

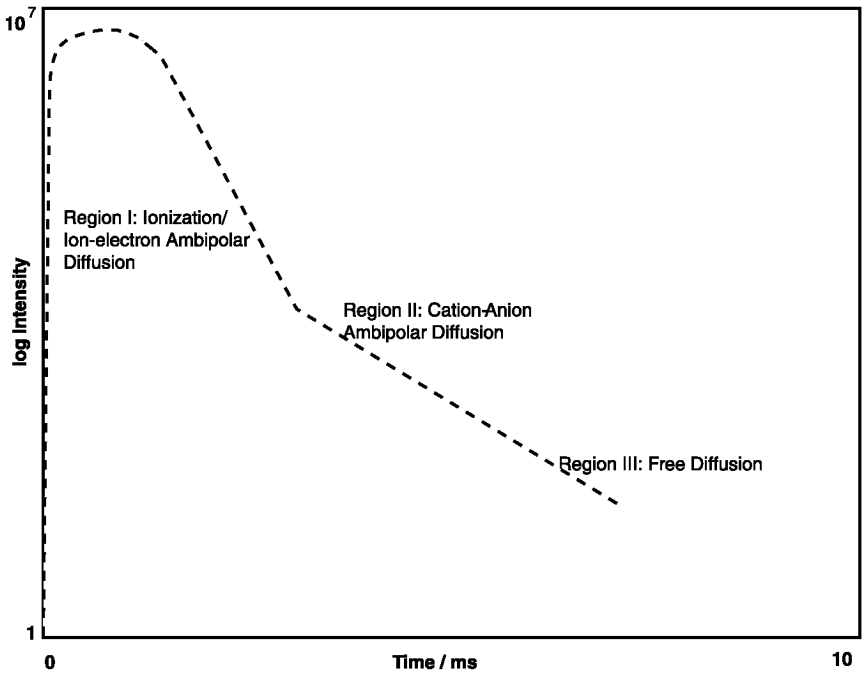

Figure 3.1. Qualitative display of regions for various modes of diffusion in a typical HPMS experiment with initially high ionization density (at t=0).

It is of current interest to examine the nature of detected species, thus the nature of the wall current. In stationary afterglow experiments, it is normally assumed that the wall current is driven by the space charge field generated by the large difference in electron and cation mobilities, and thus potential mass discrimination can only occur due to differences in the ambipolar diffusion coefficients if the process is diffusion controlled. A small mass discrimination is possible in this region due to differences in ambipolar diffusion coefficients, however, it is not customary to perform equilibria measurements in this region because of the presence of the space charge field. Unknown ambipolar diffusion coefficients can be reliably approximated to $2D^+$ as given by Eq. (3.18), and subsequently free diffusion coefficients for ions in an excess of neutral gas (as is the case for HPMS experiments) can be approximated theoretically to the classical result from Chapman and Enskog [26]:

$$D = \frac{3}{8 n_g Q_d}\left[\frac{\pi kT\left(m + m_g\right)}{m m_g}\right]^{1/2} \tag{3.29}$$

where n_g is the concentration of neutral, m and m_g are masses of ionic and neutral components, and Q_d is the momentum transfer cross section assumed here to be constant [26]. Because the momentum transfer cross section will be similar for similar ions in the same neutral gas, the ratio of two ambipolar diffusion coefficients can be written

$$\frac{D_{1a}}{D_{2a}} \approx \frac{D_1^+}{D_2^+} = \left[\frac{m_2\left(m_1 + m_g\right)}{m_1\left(m_2 + m_g\right)}\right]^{1/2} \tag{3.30}$$

If it is assumed that the wall current is the ionic flux resulting from the diffusion process, then the mass discrimination is small and ordinarily less than any normal experimental uncertainties. For example, experiments involving the first hydration step of Li^+ would have a maximum ratio [Eq. (3.30)] of about 0.7 leading to a difference in Gibbs energy of about 0.8 $kJ \cdot mol^{-1}$, although at masses higher than 30, this effect would be less than 0.93 (in the ratio of diffusion coefficients where a ratio of 1 would be indicative of no mass discrimination) in terms of hydration reactions. These differences in mass represent a small change in the evaluated standard Gibbs energy of reaction and can be ignored here as it is not customary to carry out measurements in the presence of such a large space charge field because of other potential problems. Naturally, *a priori* knowledge of the ionic mobilities would alleviate the need for any corrections as knowledge of rates of diffusing species would then be known.

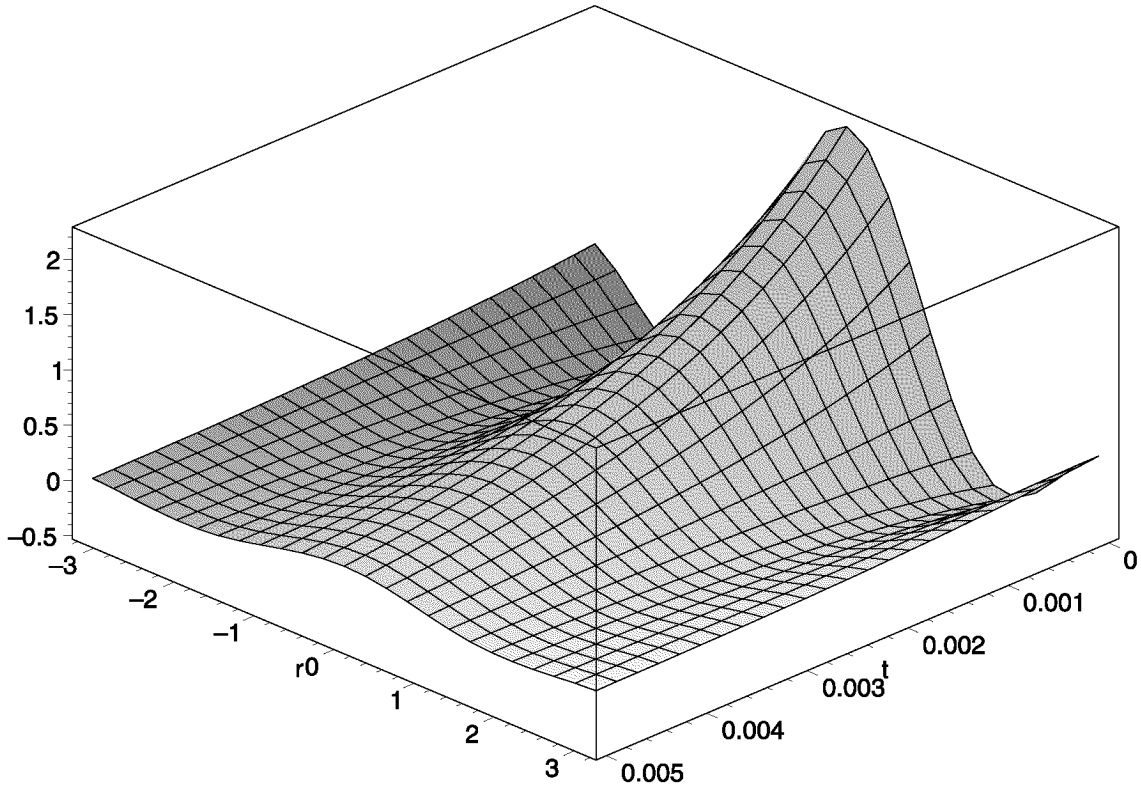

Figure 3.2. Representative solution of diffusion equation (3.28) for typical HPMS experiment. Clearly shown is the exponential ion density decay with time and the ionic distribution from the center (r=0) as well as the start of higher diffusion modes.

3.2.4 Region II: Cation-anion ambipolar diffusion

The elevated diffusion of ionic species because of cation-electron ambipolar diffusion in early stages of stationary afterglow experiments eventually leads to a breakdown in the space charge field when the number density of electrons decreases below a critical value. At this point (shown schematically in Figure 3.1) there is an accompanied slope change in plots of ln n vs. t curves corresponding to the boundary between these two processes [27]. In this region the ionic intensities of two ionic species can be written

$$\frac{\partial n_1(r,t)}{\partial t} = -D_{1i}\nabla^2 n_1(r,t) \tag{3.31}$$

$$\frac{\partial n_2(r,t)}{\partial t} = -D_{2i}\nabla^2 n_1(r,t) \tag{3.32}$$

where D_{1i} and D_{2i} refer to the cation-anion ambipolar diffusion coefficients given

analogously to the electron-ion coefficients by [23]:

$$D_{ni} = 2\frac{D^+D^-}{D^+ + D^-} \tag{3.33}$$

As such, any mass discrimination that may occur here would be a function of the ratio of D_{1i} / D_{2i} where it should also be noted that D_{1i} and D_{2i} have values intermediate between the free diffusion coefficients D^+ and D^-.

To analyze the "worst-case" scenario, we assume that the mass of the anionic species is located somewhere between the two cationic species. As an example considering the hydration of a low mass ion such as Li^+, the maximum mass discrimination would be a function of the ambipolar diffusion coefficient ratio of approximately 0.83 corresponding to a difference in free energy of approximately 0.4 kJ·mol^{-1}. Equilibria involving higher mass ions would have a significantly smaller mass effect (for example, for hydration of an ion of mass 30, the ratio of ambipolar diffusion coefficients would be less than 1.04 corresponding to a difference of less than 0.08 kJ·mol^{-1} that would tend to zero at higher masses). As such, in the cation-anion ambipolar diffusion region, the potential mass discrimination due to differences in free-diffusion coefficients of the ions can be ignored [6].

3.2.5 Region III: Free diffusion

Eventually as in the case of electron-cation ambipolar diffusion, the concentration of anions and hence the overall ionic concentration falls below the critical level (temperature dependent) to maintain cation-anion ambipolar diffusion. Virtually indistinguishable from anion-cation diffusion would be the resultant free diffusion process:

$$\frac{\partial n_1(r,t)}{\partial t} = -D_1^+ \nabla^2 n_1(r,t) \tag{3.34}$$

$$\frac{\partial n_2(r,t)}{\partial t} = -D_2^+ \nabla^2 n_2(r,t) \tag{3.35}$$

where D_1^+ and D_2^+ are the *free*-diffusion coefficients of cations 1 and 2. It can be clearly seen that any potential mass discrimination in an experiment controlled by free diffusion would be given by the ratio D_1^+ / D_2^+, the same mass discrimination as illustrated for the case of cation-electron ambipolar diffusion. Examination of the shape of ln *n* versus *t* plots would indicate that the slope between Region II (given by the cation-anion ambipolar diffusion coefficient) and Region III (given by the free-diffusion coefficient) would be virtually indistinguishable. This

corresponds to a ratio of slopes of D_{1i} / D_1^+ that can be estimated to be less than < 1.2 for very low mass ions, and < 1.02 for ions of mass above 30. As such, this 2% change in slope is unlikely to be discernible considering the low ion abundances in the free diffusion region. Clearly all of these regions can be accentuated for reactions involving large mass differences between reactant and product ions. Again it can be seen here, especially for higher masses, that any effect due to mass discrimination would be significantly less than normal experimental uncertainties.

3.3 Detected ions

It is clear from the above description that the ion flux is produced by the small concentration gradient present in any reaction chamber and is dependent on the magnitude of the ionic mobilities. However, superimposed on this relatively slow diffusional motion is the thermal motion of the various ions and gases. A typical HPMS or stationary afterglow experiment incorporates a small sampling orifice normally designed to promote molecular flow through the ion exit slit. For example, typical ion exit slit widths of 10μm [6] and typical operating pressures of 3 mbar would normally lead to molecular flow through the slit. Under these conditions the mean free path of a common bath gas, methane, would be 18μm. If an ionic species such as Na^+ behaved as a perfect gas particle, its mean free path in methane would be 24μm, where the contribution due to ion density would be negligible [28]. The mean free paths of ions in the presence of a polarizable neutral are altered due to the mutual potential energy $-(\kappa - 1)e^2 / 8\pi N r^4$ between the pair, where κ is the dielectric constant of the gas, e the charge of the ion, and N the number density. As such, the mean free paths of the ions may be reduced by a factor of 3 or more [29], dependent naturally on the polarizability of the neutral molecule. It is likely that for certain common HPMS experimental conditions outlined above ($p \leq 3$ mbar) employing ion exit slits of 10μm or less, that the flow can indeed be classified as molecular. The situation for molecular flow becomes even more favorable at higher temperatures. Various HPMS experiments have employed slightly larger slits or orifices in the attempt to improve ion signal levels. The discussion that follows pertains only to those cases where molecular flow characterizes the ion exit conditions.

The average thermal velocity of ions (assuming a Maxwellian distribution) was given by Eq. (3.9). The displacement $|\bar{x}|$ of a cloud of ions through a gas by diffusion is given by the

Einstein relation [30]:

$$\left|\bar{x}\right| = \left(\frac{4Dt}{\pi}\right)^{1/2} \tag{3.36}$$

This leads directly to the average velocity as a function of time t:

$$\bar{v} = \left(\frac{D}{\pi t}\right)^{1/2} \tag{3.37}$$

Substitution of appropriate values into Eq. (3.9) (thermal) and (3.37) (diffusional) shows immediately that the thermal velocity of the ions far exceeds the average velocity due to diffusion. The average lifetime of a diffusing ion can be written:

$$\tau = \frac{1}{D}\left(\frac{r}{\pi}\right)^2 \tag{3.38}$$

where τ is the lifetime of the ionic species (time required to reach the wall/slit) and r is the relevant container dimension or distance to the wall/slit. The diffusion velocity at the slit can be simply calculated by:

$$\bar{v}_{slit} = \sqrt{\pi}\frac{D}{r} \tag{3.39}$$

A typical diffusion coefficient, for example NO^+ (in 1 Torr NO) has a coefficient of 42 cm^2/s [23] that leads to a diffusional velocity at the slit of $\bar{v}_{slit} = 149$ cm/s. However, the thermal velocity of NO^+ under these same conditions is approximately 300 times larger than the diffusional velocity.

3.3.1 Particle exit: Near slit behavior

In a system of equilibrated particles of differing masses, the Maxwell velocity distribution yields [21]:

$$N_{\text{mf}} = \frac{pA}{(2\pi mkT)^{1/2}} \tag{3.40}$$

where N_{mf} is the number of particles of mass m leaving a slit of area A at a pressure p under molecular flow conditions per unit time. In the absence of any electric fields, the subsequent detected ion abundance is mass dependent:

$$I_x = c_1 \frac{p_x A}{(m_x kT)^{1/2}} \tag{3.41}$$

where c_1 is some system dependent constant. As such, it is clear that in the absence of any

other processes, ions with lighter masses will be sampled more often than those of higher masses in the ratio: $\left(m_{high}/m_{low}\right)^{1/2}$ directly related to the equation derived by Graham [20]. For this case of molecular flow, a well-characterized mass discrimination results. For the case of a well-defined continuum flow, no mass discrimination would take place [15, 16], although this often is not an advantageous experimental condition. For certain HPMS experiments, especially those involving clustering equilibria, it is possible that collisions between ionic and other species in the region close to the slit and outside of the ion source may alter the equilibrium distribution of ionic species for continuum flow through the slit. It is also clear that effects of adiabatic cooling become non-negligible for high flow regimes [6].

It should be noted that although mass discrimination may occur via the diffusion process itself, that this will be associated by a change in the slope of ln n vs. t plots. However, mass discrimination of the type created by the near-slit thermal motion of the ions, will lead only to different absolute values (consistent with time) of the detected individual ion abundances so long as depletion of the source concentrations is controlled more by diffusion to the wall than out of the slit.

3.3.2 Calculations and experimental comparisons

The equilibrium constant of a typical HPMS experiment was given by Eq. (3.4). However, according to Eq. (3.41), the actual ion intensities need to be weighted by the square root of mass. As such, we can define the corrected equilibrium constant K_{eq}^{corr} in terms of these corrected ion intensities:

$$K_{eq}^{corr} = \frac{I_{B_2H^+} \cdot p_{B_1}}{I_{B_1H^+} \cdot p_{B_2}} \times \left(\frac{m_{B_2H^+}}{m_{B_1H^+}}\right)^{1/2} \tag{3.42}$$

It is clear that the described mass discrimination would affect the calculated standard free energy and entropy changes of a reaction, but not the enthalpy change. Using Eq. (3.42) as a guide, corrected equilibrium constants, standard free energies and entropies are given (for a reaction Ion1 + Neutral1 = Ion2 + Neutral2) by:

$$K_{eq}^{corr} = K_{obs}\left(\frac{m_2}{m_1}\right)^{1/2} \tag{3.43}$$

$$\Delta G_{eq}^{\circ,corr} = \Delta G_{obs}^{\circ} - \frac{RT}{2}\ln\frac{m_2}{m_1} \tag{3.44}$$

$$\Delta S^{\circ,\mathrm{corr}}_{\mathrm{eq}} = \Delta S^{\mathrm{o}}_{\mathrm{obs}} + \frac{R}{2}\ln\frac{m_2}{m_1} \qquad (3.45)$$

where experimentally determined quantities are listed as "obs" and the true or corrected quantities as "eq, corr." As an example, for the hydration of Li^+, $m_1 = 7$, $m_2 = 25$, the correction to $\Delta G^{\circ}_{\mathrm{eq}}$ would be 3.2 kJ·mol^{-1} at 600 K, significantly larger than the normal stated HPMS uncertainty of ± 0.8-1.0 kJ·mol^{-1}.

Kebarle and Hogg [31] have measured the conductances of their ion source exit orifice for He, air and Xe and noted that the ratio of conductances was inversely proportional to the ratio of the square roots of the molecular weight. They concluded that observed ionic abundances depend on mass although this correction was not routinely reported in subsequent studies. As discussed earlier, Grimsrud and coworkers have considered the effects of mass discrimination of the neutral components [15, 16]. The present results suggest that not only neutral but also ionic mass discrimination be considered. For those reactions involving the measurement of ion abundances for ions of widely different mass, as results from measurement of clustering and other exchange equilibria, this mass discrimination makes a significant contribution to measured abundances. For reactions involving higher mass ions, the effect is reduced. For these reactions, mass discrimination effects are often smaller than experimental errors. This is the case for equilibrium reactions involving highly solvated ion-clusters where the mass difference between reactant and product ions is small. However, for a large number of reactions this effect should be considered.

We have compared calculated standard free energy changes of reactions from HPMS measurements and those obtained using ion cyclotron resonance equilibria results. We have chosen to compare HPMS results with ion cyclotron resonance because of the reduced mass discrimination possibilities in ICR. Typical pressures in ICR measurements (approx. 10^{-5} mbar) prevent the achievement of equilibrium during normal ion trapping times (approx. 1s) for three-body association reactions but these conditions are appropriate for equilibrium transfer reactions. Both types of reactions are amenable to HPMS but we are restricted in comparing only those reactions derived from both methods. Most ICR experiments involve essentially *in situ* ion detection thereby removing any mass discriminatory effects of having ions pass from the source through a small ion exit slit. Because the majority of HPMS measurements have been obtained at elevated temperatures and ICR measurements mostly near ambient, comparison of results from the two methods is not normally direct.

Ideally comparisons for reaction equilibria measured by both techniques under identical conditions would yield the most meaningful results. However, this was not possible and most often elevated temperature data from HPMS were compared to ICR measurements using the appropriate change in standard entropy (from the same experimental investigation). The elevated temperatures of the HPMS experiments assist in making conditions closer to true molecular flow. We have compared the free energy changes for several common reactions that appear in both HPMS and ICR thermochemical ladders [32-34]. We have limited these comparisons to ratios of m_1 / m equal to or greater than 2. The majority of comparisons were based on indirect calculations involving the use of thermodynamic cycles. This may have a slight advantage in that the free energy changes might be more reliable since they are averaged over 2-3 thermodynamic cycles although there are also associated additive experimental uncertainties. The results of these comparisons are presented in Table 3.1. There are 18 independent reactions and 27 comparisons in total available in Table 3.1 to compare HPMS and ICR results, with limited duplicated HPMS data for certain reactions. Of the 27 reactions considered, the mass correction improved the agreement in 21 cases, 6 corrections made the agreement worse. It should be noted that the HPMS measurements of Szulejko and McMahon [32] may not have had strictly molecular flow conditions because of the slightly larger ion exit orifices used, but a flow intermediate between molecular and continuum. This was also the case for Meot-Ner and Sieck [35] who used 60μm orifices. However, under most conditions, especially those at elevated temperatures, the flow can be stated to be predominantly molecular where these corrections should improve agreement between HPMS and ICR measurements. Figure 3.3 shows graphically the improvement of the HPMS free energies from Szulejko and McMahon [32] and Meot-Ner and Sieck [35] and the ICR ladder of Wolf [34] from Table 3.1.

We have also compared results from HPMS and ICR experiments for association reactions as listed in Keesee and Castleman's compilation [36]. Comparisons of these results are presented in Table 3.2 where all HPMS results stem from direct measurements. Results for ICR experiments were obtained from ICR data for specific transfer equilibria involving a reference compound combined with HPMS data for the formation of the reference. As an example, Cl^- transfer to benzene is easily measured by HPMS:

$$Cl^- + C_6H_6 = Cl(C_6H_6) \tag{3.46}$$

whereas ICR results were derived from a cycle involving:

$$Cl(C_6H_6)^- + \text{t-BuOH} = Cl(\text{t-BuOH})^- + C_6H_6 \tag{3.47}$$

and auxiliary equilibrium information for

$$Cl(\text{t-BuOH})^- = Cl^- + \text{t-BuOH} \qquad (3.48)$$

was taken from HPMS experiments.

Table 3.1. Thermochemical data comparison for proton transfer reactions.

Reaction:	ΔG^{o}_{HPMS}	$\Delta G^{o,\,corr,\,a}_{HPMS}$	$\Delta G^{o,\,b}_{ICR}$	$\left\lvert \frac{\delta\Delta G^{o}_{corr}}{\delta\Delta G^{o}_{orig}} \right\rvert^{c}$	HPMS ref.[d]
$CF_3CH_2NH_3^+ + NH_3 = NH_4^+ + CF_3CH_2NH_2$	-8.92	-6.64	-8.03	1.57	B
$C_6H_5CHCH_3^+ + NH_3 = NH_4^+ + C_6H_5CHCH_2$	-12.05	-9.71	-9.82	0.05	B
$CH_3CO_2C_2H_6^+ + NH_3 = NH_4^+ + CH_3CO_2C_2H_5$	-15.43	-13.31	-15.17	7.28	A
	-17.84	-15.72	-15.17	0.20	B
$(CH_3)_2SH^+ + NH_3 = NH_4^+ + (CH_3)_2S$	-17.94	-16.28	-15.62	0.28	B
$(C_2H_5)_2OH^+ + NH_3 = NH_4^+ + (C_2H_5)_2O$	-15.73	-13.83	-16.51	3.43	A
$CH_3CO_2CH_4^+ + NH_3 = NH_4^+ + CH_3CO_2CH_3$	-28.37	-26.47	-27.22	0.66	A
	-36.55	-34.65	-27.22	0.80	B
$(CH_3)_2COH^+ + NH_3 = NH_4^+ + (CH_3)_2CO$	-31.65	-30.07	-32.13	4.28	A
	-40.54	-38.97	-32.13	0.81	B
$i\text{-}C_4H_9^+ + NH_3 = NH_4^+ + i\text{-}C_4H_8$	-39.97	-38.44	-38.38	0.04	A
	-45.76	-44.22	-38.38	0.79	B
$i\text{-}C_3H_7CNH^+ + NH_3 = NH_4^+ + i\text{-}C_3H_7CN$	-39.57	-37.76	-41.51	1.93	A
	-50.19	-48.39	-41.51	0.79	B
$(CH_3)_2OH^+ + NH_3 = NH_4^+ + (CH_3)_2O$	-50.53	-49.26	-49.09	0.12	A
	-58.78	-57.50	-49.09	0.87	B
$C_2H_5CNH^+ + NH_3 = NH_4^+ + C_2H_5CN$	-59.58	-58.07	-50.43	0.84	B
$C_6H_5CH_4^+ + NH_3 = NH_4^+ + C_6H_5CH_3$	-59.72	-57.54	-57.13	0.16	A
	-69.34	-67.15	-57.13	0.82	B
$CH_2CHCNH^+ + NH_3 = NH_4^+ + CH_2CHCN$	-73.69	-72.23	-60.70	0.89	B
$CH_3HCO_2H^+ + NH_3 = NH_4^+ + CH_3HCO_2$	-60.41	-58.79	-61.59	2.37	A
	-71.21	-69.59	-61.59	0.83	B
$CH_3CNH^+ + NH_3 = NH_4^+ + CH_3CN$	-78.19	-77.06	-64.71	0.92	B
$CH_3SH_2^+ + NH_3 = NH_4^+ + CH_3SH$	-84.57	-83.24	-69.62	0.91	B
$CH_3CHOH^+ + NH_3 = NH_4^+ + CH_3CHO$	-88.10	-86.88	-73.64	0.92	B
$C_6H_7^+ + NH_3 = NH_4^+ + C_6H_6$	-85.99	-84.03	-84.80	0.64	A
	-101.39	-99.42	-84.80	0.88	B

All the values are in $kJ \cdot mol^{-1}$ at 320K. [a]HPMS data corrected for mass discrimination. [b]All ICR data are from ref. [34] and recalculated for 320K. [c]The absolute value of the ratio of the difference between corrected HPMS and experimental ICR data and the difference between experimental HPMS and ICR data. Values smaller than one indicate improved agreement between HPMS and ICR data after the correction has been applied. [d]HPMS data: A – from ref. [32], B – from ref. [35].

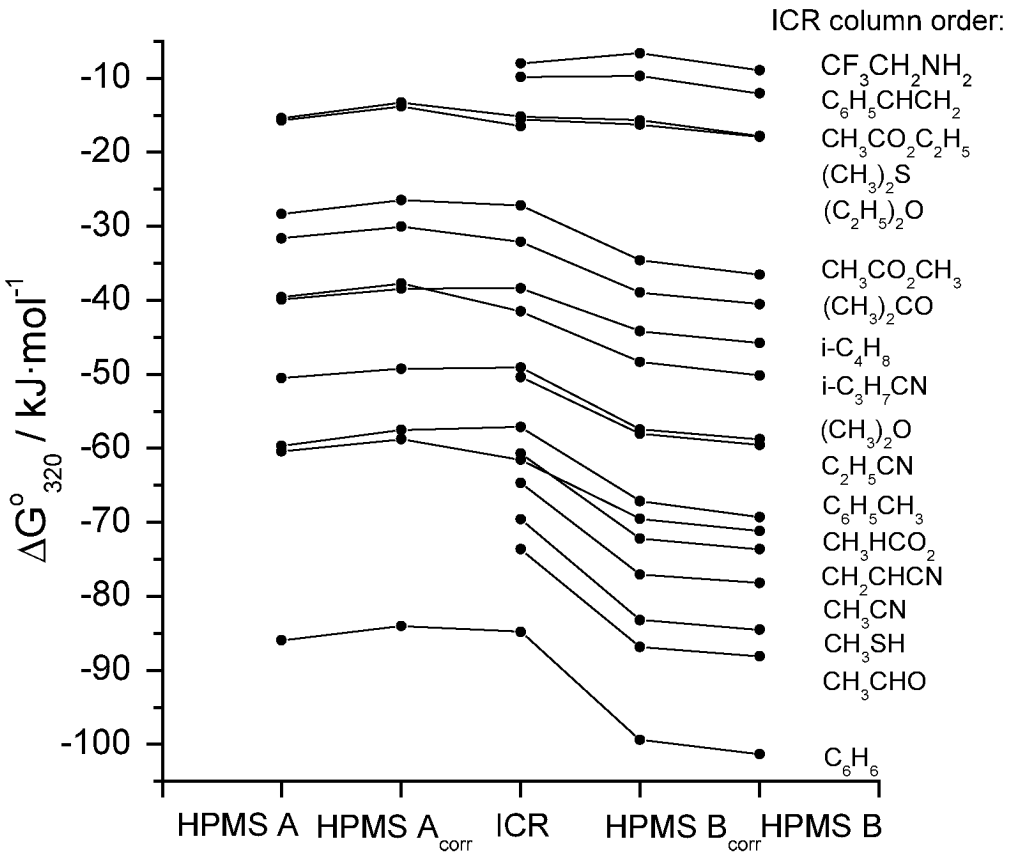

Figure 3.3. Thermochemical ladder comparison for proton transfer reactions at 320K relative to ammonia. The data are taken from Table 3.1. HPMS A data are from ref. [32], HPMS B data from ref. [35], ICR data from ref. [34] recalculated at 320K [33].

Combining reactions (3.47) and (3.48), leads to the desired reaction given by Eq. (3.46). In this case, both HPMS and the ICR-cycle data had to be corrected for mass discrimination as the ICR-cycle contained results from an HPMS experiment. Reactions whose corrections for both HPMS and ICR were identical were not considered. The agreement between ICR and HPMS improved for 66% of the reactions considered after applying the appropriate mass corrections. These improvements were small and did not affect the average agreement as observed for the reactions listed in Table 3.1 because of a few widely disparaging values obtained by HPMS and ICR and because of the various cumulative experimental uncertainties in making these calculations.

Table 3.2. Thermochemical data comparison for association reactions.

Reaction:	$\Delta G^{o,\,a}_{HPMS}$	$\Delta G^{o,\,corr,\,b}_{HPMS}$	$\Delta G^{o,\,corr,\,c}_{ICR}$	$\Delta G^{o,\,d}_{ICR}$	$\left\lvert\frac{\delta\Delta G^{o}_{corr}}{\delta\Delta G^{o}_{orig}}\right\rvert^{e}$	Ref. complex[f]
$Cl^- + C_6H_4F_2 = Cl^-(C_6H_4F_2)$	-32.22	-34.02	-34.05	-32.64	0.07	Cl^--t-BuOH
$Cl^- + C_6H_5Cl = Cl^-(C_6H_5Cl)$	-27.20	-28.99	-30.29	-28.87	0.78	Cl^--t-BuOH
$Cl^- + C_6H_6 = Cl^-(C_6H_6)$	-15.90	-17.36	-21.50	-20.08	0.99	Cl^--t-BuOH
$Cl^- + C_6H_6 = Cl^-(C_6H_6)$	-15.06	-16.52	-21.49	-20.08	0.99	Cl^--t-BuOH
$Cl^- + CH_2Cl_2 = Cl^-(CH_2Cl_2)$	-37.24	-38.75	-39.90	-38.49	0.91	Cl^--t-BuOH
$Cl^- + CH_2O_2 = Cl^-(CH_2O_2)$	-84.10	-85.15	-78.40	-76.99	0.95	Cl^--t-BuOH
$Cl^- + CH_2O_2 = Cl^-(CH_2O_2)$	-106.27	-107.31	-78.39	-76.99	0.99	Cl^--t-BuOH
$Cl^- + CH_3Cl = Cl^-(CH_3Cl)$	-17.15	-18.25	-27.35	-25.94	1.04	Cl^--t-BuOH
$Cl^- + CH_3CN = Cl^-(CH_3CN)$	-37.24	-38.20	-40.74	-39.33	1.21	Cl^--t-BuOH
$Cl^- + CH_3CN = Cl^-(CH_3CN)$	-38.49	-39.45	-40.74	-39.33	1.53	Cl^--t-BuOH
$Cl^- + CHCl_3 = Cl^-(CHCl_3)$	-45.19	-47.01	-48.27	-46.86	0.75	Cl^--t-BuOH
$Cl^- + CHCl_3 = Cl^-(CHCl_3)$	-49.37	-51.20	-48.27	-46.86	1.17	Cl^--t-BuOH
$Cl^- + H_2O = Cl^-(H_2O)$	-36.82	-37.33	-36.55	-35.15	0.47	Cl^--t-BuOH
$Cl^- + H_2O = Cl^-(H_2O)$	-37.66	-38.17	-36.55	-35.15	0.64	Cl^--t-BuOH
$Cl^- + H_2O = Cl^-(H_2O)$	-34.31	-34.82	-36.55	-35.15	2.07	Cl^--t-BuOH
$Cl^- + HAc = Cl^-(HAc)$	-66.11	-67.35	-71.28	-69.87	1.05	Cl^--t-BuOH
$Cl^- + HCl = Cl^-(HCl)$	-69.87	-70.75	-68.35	-66.94	0.82	Cl^--t-BuOH
$Cl^- + MeOH = Cl^-(MeOH)$	-42.68	-43.48	-42.83	-41.42	0.52	Cl^--t-BuOH
$Cl^- + MeOH = Cl^-(MeOH)$	-41.00	-41.81	-40.29	-39.33	0.91	Cl^--CH_3CN
$Cl^- + MeOH = Cl^-(MeOH)$	-42.68	-43.48	-40.29	-39.33	0.95	Cl^--CH_3CN
$Cl^- + MeOH = Cl^-(MeOH)$	-41.00	-41.81	-42.83	-41.42	2.44	Cl^--t-BuOH
$Cl^- + NH_3 = Cl^-(NH_3)$	-15.06	-15.55	-20.24	-18.83	1.24	Cl^--t-BuOH
$Cl^- + SO_2 = Cl^-(SO_2)$	-62.34	-63.63	-62.91	-61.50	0.86	Cl^--t-BuOH
$Cl^- + C_3H_6O = Cl^-(C_3H_6O)$	-33.05	-34.56	-35.73	-34.31	0.93	Cl^--t-BuOH

All the values are in $kJ \cdot mol^{-1}$ at 300K. [a]All HPMS data are taken from ref. [36]. [b]HPMS data corrected for mass discrimination. [c]Indirect ICR data corrected for mass discrimination in used HPMS reference data. [d]All ICR data are taken from ref. [36]. The data are indirect and are referenced to the scale based on a complex indicated in (f). [e]The absolute value of the ratio of the difference between corrected HPMS and ICR data and the difference between experimental HPMS and ICR data. Values smaller than one indicate improved agreement between HPMS and ICR data after the corrections have been applied. [f]Reference complex relative to which ICR data in (d) was calculated.

From the classical theoretical discussion provided earlier and supported by comparisons provided in Table 3.1, it is suggested that the correction due to mass discrimination during ion sampling in HPMS or other similar experiments when a ratio of ion abundances are required be applied. Even though experimental uncertainties are often larger than this correction, it is not

normally insignificant except for the special case of identical or near-identical mass ions (charge transfer reactions). In some cases it might also be appropriate to include corrections due to differences in ionic mobility, but these corrections (as discussed above) are smaller than those due to sampling and for the most part can be ignored (especially at higher mass). Because of the tendency for further mass discrimination related to the ionic flux to the slit, it is suggested that this well-characterized discrimination be considered.

It is desirable to make a comparative study of specific reactions under identical conditions with large mass ratios of reactant and product ions by HPMS and ICR or similar methods. Such experiments with our newly constructed high-pressure mass spectrometer equipped with a highly stable and known ion source temperature are planned once we can also attempt similar experiments using ICR or some other non discriminatory technique.

3.4 Conclusions

We have examined and characterized the time-dependent ionic profiles that occur in traditional high-pressure mass spectrometric and stationary afterglow experiments. It has been shown that the nature of ionic flow out of an ion source leads to a mass discrimination effect related directly to the average velocities of each individual ionic species during conditions normally present in an HPMS or stationary afterglow experiment. These mass discrimination effects are easily calculated and affect standard free energy and entropy changes, but not the corresponding standard enthalpy changes. It was shown that experimental results corrected for mass discrimination are (on average) in better agreement with results from non-mass discriminated measurements (for example from ICR). As such, it is believed that results from HPMS measurements should be consistently corrected for mass discrimination dependent on the type of flow present. It also appears less problematic to correct molecular flow results for this mass discrimination than continuum flow results for other problems [6].

Chapter 4. Experimental Study of Hydration of Halides

4.1 Introduction

There have been a number of previous investigations of the thermodynamics of halide hydration using HPMS. Early equilibrium studies determined enthalpies and entropies for the reaction

$$X^-(H_2O)_{n-1} + H_2O = X^-(H_2O)_n \quad (4.1)$$

where X=Cl (n=4), I (n=3) [37, 38], and X=F (n=5), Br (n=4) [38]. A later comprehensive investigation [39] extended the range of experimentally determined enthalpies and entropies to larger cluster sizes (n=9 for F, n=6 for Cl and Br, n=4 for I). Enthalpies for an additional hydration step for each of these halides beyond the experimentally determined steps mentioned above were estimated in ref. [39] using an assumed value for the entropy change and experimental values for the free energy change determined at one or two temperatures. All of the previous investigations used ion sources based upon the original Kebarle designs and similar to the one used in ref. [38]. The results obtained in these studies are in rather good agreement.

We have tried to further extend the range of experimentally observed cluster sizes for Cl^-, Br^-, I^- and the number of hydration steps measured under equilibrium conditions using our newly constructed ion source of what is believed to be an improved design.

4.2 Experimental

The measurements were performed with our high-pressure pulsed electron beam mass spectrometer described in Chapter 2. The samples were prepared in the gas handling plant by injecting distilled water containing traces of CCl_4 (0.5% vol.), CH_2Br_2 (0.45% vol.) or CH_3I (0.82% vol.) with a microliter syringe into a 5L gas mixing glass bulb kept at 140°C and filled with methane. After an equilibration period of ~20min., the mixture was allowed to flow from the bulb through the ion source. Water partial pressures in the source were generally in the range 0.02-0.35 mbar. Halogen anions are formed by dissociative electron capture from CCl_4, CH_2Br_2 or CH_3I that are all efficient electron-capture agents. Exothermic association reactions of the type described by Eq. (4.1) require third-body collisions for removal of the excess energy from the initially excited products. Following an electron pulse, ions diffuse to the walls

through the major neutral component at the same time engaging in the following reaction:

$$X^-(H_2O)_{n-1} + H_2O + CH_4 = X^-(H_2O)_n + CH_4 \qquad (4.2)$$

In addition to being a third-body agent in this reaction, methane also serves to thermalize the electrons and trap the ions in the ion source for a time sufficient to establish equilibrium for reaction (4.2). The range of overall pressures in the ion source at different temperatures was shown in Figure 2.4.

Ionizing electron pulse widths of 5-70μs and electron gun filament currents of 4-5A were employed. It is undesirable to deliver too many electrons to the ion source since the resulting ionic profiles may display several changes of slope, as discussed in Chapter 3 and shown in Figure 3.1 and are somewhat difficult to analyze. It was not realized in early experiments that the electron gun required re-tuning of deflection electrodes when the temperature of the ion source was changed by more than 20-30°C. The time between electron pulses was normally adjusted to 13-20ms. This time was, in general, chosen to be 3 times longer than the ion residence time in the ion source that could be evaluated from ionic profiles (2-5ms). It might be argued that a fraction of the ions might still remain in the source at times longer than the estimated residence time, which would lead to erroneous results. The equilibrium ionic ratio is determined from detected ion counts and any ion currents that are below the inherent detection limit should not change it to any significant extent. Tests with time periods varying up to 50ms were done and yielded identical results to the shorter times periods. The multichannel scaler channel dwell time was normally set to 10μs and the reactions were monitored for 5-10ms. Between two and ten thousand pulses were sufficient to obtain reasonable ionic profiles. Data acquisition was performed in a programmed mode. Each ion was monitored for ~30sec in succession, then this sequence was repeated several times. Comparison of several profiles for each ion allowed assessment of the overall stability of conditions in the ion source during the course of the experiment.

At low ion source pressures, the reactants and products may be assumed to behave as perfect gases. For a standard state pressure of 1000 mbar the equilibrium constant for reaction (4.1) is given by:

$$K_n = \frac{I_n \cdot 1000}{I_{n-1} \cdot p(H_2O)} \qquad (4.3)$$

where $p(H_2O)$ is the water partial pressure, and I_n and I_{n-1} are measured intensities of $X^-(H_2O)_n$ and $X^-(H_2O)_{n-1}$, respectively, after equilibrium has been established. The ratio of

measured ionic intensities should remain constant when equilibrium conditions apply.

The various experiments were performed over a temperature range +170°C to -45°C. This lower temperature limit was a result of the saturated water vapor pressure becoming too low producing some water vapor condensate inside the ion source.

4.3 Results and discussion

Typical ionic profiles are shown in Figure 4.1. It can be seen that 0.6ms after the electron beam pulse, the profiles become parallel and equilibrium is probably established. The overall decay in ionic intensities is caused by loss of ions through diffusion to the ion source walls and consecutive discharge.

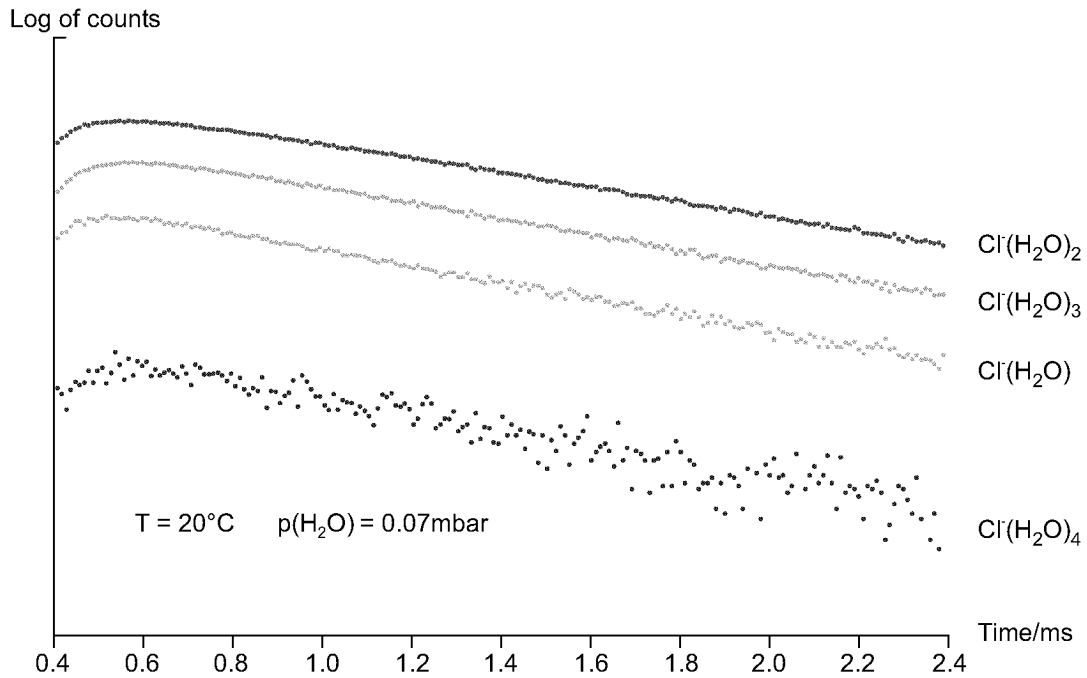

Figure 4.1. Typical ionic profiles.

A more convenient examination of the profiles results when individual ionic intensities are normalized to the total ion intensity [40]. Normalized profiles for a representative system are shown in Figure 4.2. It can be seen that the profiles become truly parallel and equilibrium is established only 1.2ms after the electron beam pulse. Examination of both raw and normalized ionic profiles was used to determine the onset of equilibrium and the time interval over which the ratio of ion intensities should be averaged for calculation of equilibrium constants.

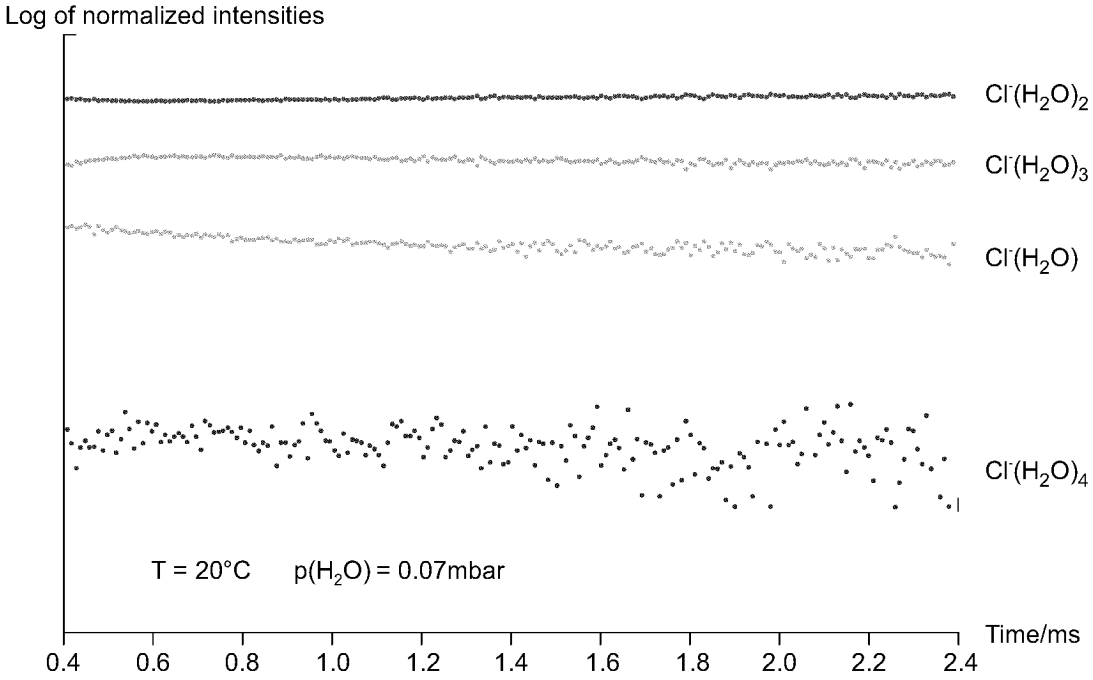

Figure 4.2. Ionic profiles normalized to total ion intensity.

Tests were performed to verify that equilibrium was indeed established by varying the water partial pressure and the total pressure in the ion source. Figure 4.3 shows the results of such tests for the (2,3) hydration step for Cl^-. Similar behavior was observed for the other halides. The data points on this plot were obtained not only at different partial pressures of water, but also at different total ion source pressures within the ranges shown in Figure 2.4.

Discussion of experimental errors in HPMS

Before the experimental results are presented, it is necessary to review the sources of potential experimental error under certain conditions in the HPMS technique. The expression for the equilibrium constant (4.3) involves the ratio of ionic abundances and the partial pressure of water in the ion source. Errors in the partial pressure of water, apart from errors in the sample preparation and errors in measurements of the total ion source pressure, might arise from mass discrimination in the gas exiting the ion source [15, 16]. It is assumed that the ratio of partial pressures of methane and water in the ion source is the same as in the gas handling plant. However, due to mass discrimination there will be an enrichment of the heavier component in the ion source. The maximum magnitude of the enrichment is characterized by the square root of the ratio of masses of water and methane. Although this ratio is already close to unity (1.06), the mass discrimination is further reduced by the flow-through design of the ion

source. In our case, the ratio of the gas flow into the source to the outflow through the electron entrance and ion exit slits was in the range 1.5-1.8 depending on the source temperature and pressure. In this configuration errors in the water partial pressure due to mass discrimination are negligible. Experiments involving heavier ligands should use a carrier gas in mass close to the ligand. Systematic errors in the water partial pressure lead mostly to errors in the entropy, but not the enthalpy.

Early on in the development of the HPMS technique, problems that affect measured ionic ratios were recognized [41]: (a) adiabatic cooling of the cluster ions following exit from the ion source and non-equilibrium cluster growth, (b) collision-induced dissociation (CID) caused by high gas densities near the ion exit aperture, and (c) unimolecular dissociation of ions during mass analysis. In addition, there are problems associated with mass discrimination in reference to sampling through the ion exit slit that have been previously discussed in Chapter 3. One further uncertainty related to errors in temperature measurement will also be considered.

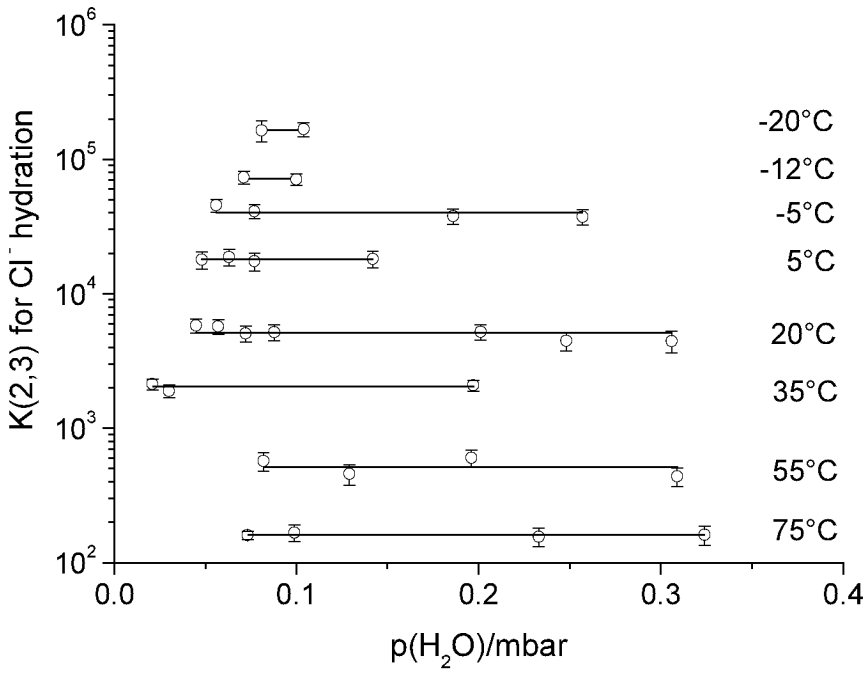

Figure 4.3. Equilibrium constants vs. partial water vapor pressure.

Adiabatic cooling is avoided by ensuring that molecular flow occurs through the ion exit slit that requires a slit width to be smaller than the mean free path of ions under the appropriate experimental conditions. The implementation of molecular flow also reduces collision-induced dissociation, although, it will always occur to some extent. The number of gas molecules leaving the ion source at any time is considerably larger than the number of exiting ions. A weak electric field is always present outside the source that draws ions into the acceleration section of the mass spectrometer. Some of the ions will inevitably collide with the neutral gas molecules. Due to the requirement of energy and momentum conservation, the maximum energy of an ion colliding with a gas molecule available to overcome the energy barrier for dissociation is limited to:

$$\mathrm{E}=eV\frac{m_{\mathrm{gas}}}{m_{\mathrm{ion}}+m_{\mathrm{gas}}} \tag{4.4}$$

where eV is the kinetic energy of the ion acquired by moving through a potential difference V. Evaluation of Eq. (4.4) with $m_{\mathrm{ion}}=50$, $m_{\mathrm{gas}}=16$ (methane), and the typical ion-water clustering reaction value for the dissociation threshold of 45 kJ·mol^{-1} shows that only 1.8V acceleration is sufficient for the ion to acquire enough energy to achieve dissociation. The effect of CID on van't Hoff plots has been examined previously [9]. Here the derivation of a more complete expression for the effects of CID on observed equilibrium constants that considers not only the effect of the degree of dissociation, but also the partial pressures of the neutral clustering ligand, will be given.

Some simplifying assumptions are required here and the accuracy of these assumptions will be discussed later in this chapter. We assume that a fraction α of ions that dissociates collisionally is identical for n and n-1 clusters. The second assumption is that all dissociation occurs before the ions are appreciably accelerated. For this case, dissociating n+1 and n clusters will be detected as n and n-1, respectively. If the second assumption is invalid, then ions that dissociate after acquiring considerable kinetic energy will not be detected if an electrostatic analyzer is present in the system, as the ESA will energy filter these ions. In the absence of an electrostatic analyzer the dissociated ions will be detected at different nominal masses, not corresponding to the mass of any of the cluster ions. The third assumption is that α is independent of the internal energy of the ions that is defined by the ion source temperature. Recalling that n-1 clusters dissociate to n-2 clusters, Eq. (4.3) can be rewritten as

$$K_{n,\mathrm{obs}} = \frac{1000\left[(1-\alpha)I_n + \alpha I_{n+1}\right]}{p(\mathrm{H_2O})\left[(1-\alpha)I_{n-1} + \alpha I_n\right]} \tag{4.5}$$

where $K_{n,\mathrm{obs}}$ is the observed equilibrium constant. After algebraic rearrangement and substitution of relevant equilibrium constants defined by Eq. (4.3), Eq. (4.5) becomes

$$K_{n,\mathrm{obs}} = \frac{1000(1-\alpha) + \alpha K_{n+1} p(\mathrm{H_2O})}{\alpha p(\mathrm{H_2O}) + 1000/K_n} \tag{4.6}$$

Now the manner in which the partial pressure of ligand and the degree of dissociation will affect the measured equilibrium constants and, hence, the van't Hoff plots can be explored. Figures 4.4 and 4.5 show how the observed equilibrium constant for the Cl^- (2,3) hydration step differs from the true equilibrium constant at high and low temperatures as a function of α and the partial water vapor pressure. The minimum value for α used in these plots was 0.001. It can be clearly seen that, for $\alpha > 0$, the equilibrium constant rapidly decreases with increasing partial pressure of ligand. The decrease is much larger at low temperatures where larger clusters are normally present. Therefore, measurements of larger clusters are much more prone to errors resulting from CID than are measurements of smaller clusters.

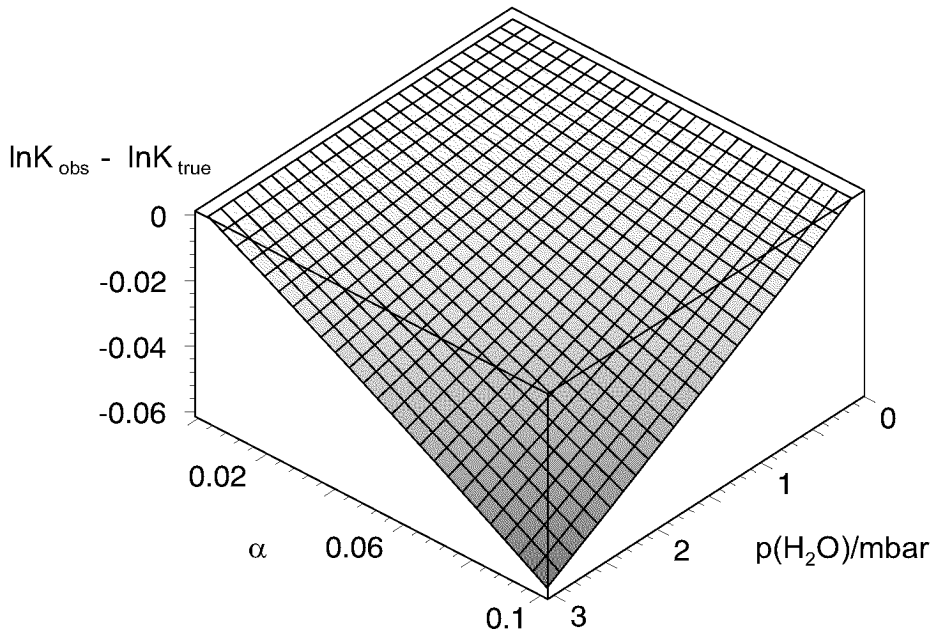

Figure 4.4. Effect of collision-induced dissociation on K(2,3) for Cl^- hydration at 75°C.

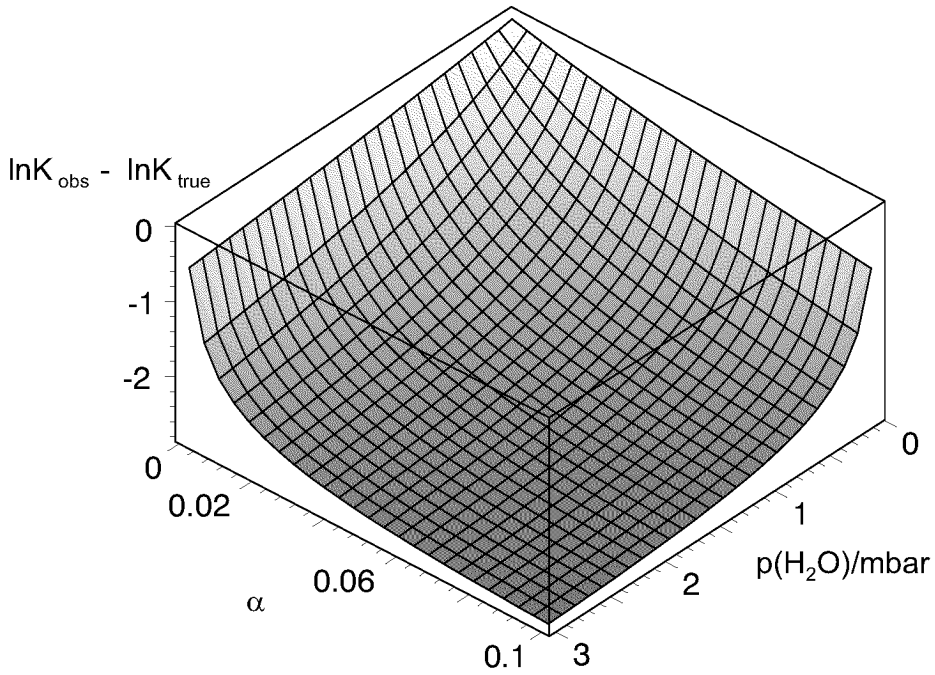

Figure 4.5. Effect of collision-induced dissociation on K(2,3) for Cl^- hydration at -25°C.

Figure 4.6 shows a family of van't Hoff plots for the same reaction calculated at a fixed partial water pressure. This figure demonstrates that if measurements are taken over a sufficiently narrow temperature range, a curved van't Hoff plot can be mistaken for a linear one that would lead to smaller absolute values of calculated enthalpy and entropy changes for the studied reaction. If the degree of CID is high enough $(\alpha \geq 0.3)$, the plots have inflection points. Experimental scatter of measured equilibrium constants at different temperatures naturally makes it more difficult to distinguish CID.

The equilibrium constants shown in Figure 4.3 reveal a tendency to decrease with increasing partial pressure of water vapor. A similar tendency was observed for other reactions measured using our HPMS instrument. If the reason for this behavior was CID, values of α calculated from these results should be in the range 0.04-0.15 for different ion source pressures. However, van't Hoff plots with these values of α would have considerable curvature at low temperature that was not observed for our experimental results. In addition, a linear dependence of calculated values of α on the ion source pressure was not observed, as would be expected from the argument that α should be proportional to the gas number density outside the source, and, therefore, pressure inside the source.

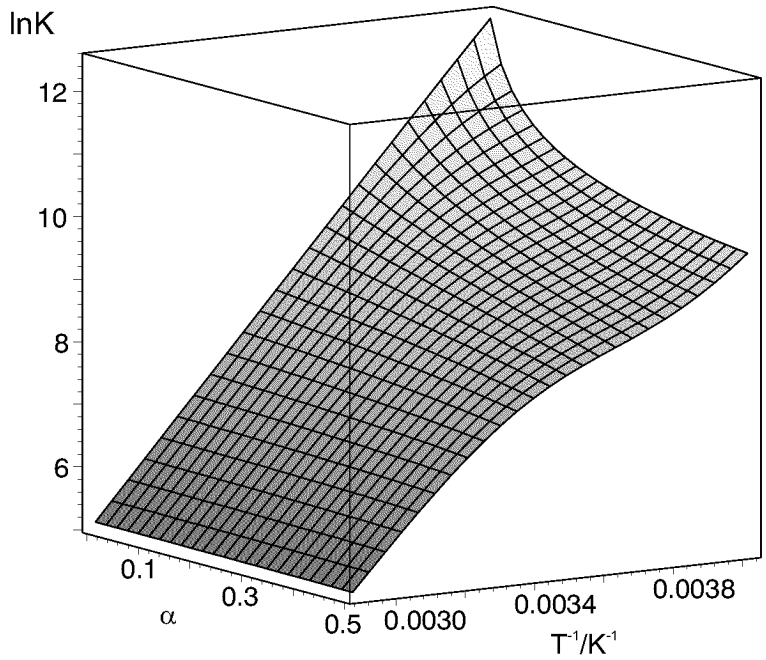

Figure 4.6. Family of van't Hoff plots for K(2,3) for Cl^- hydration at $p(H_2O)$=0.2mbar.

It was found that errors in our calculation of the ion source pressure were the cause of the observed behavior. The ion source pressure in our instrument is calculated from the pressures measured at both ends of the gas inlet and outlet line, whose conductances were calibrated together with the conductance of the source slits. The error in the calculated ion source pressure depends monotonically on the overall pressure, and is still within the assigned accuracy of the calibration (0.05 mbar). This was verified by back-calculating one pressure from the other for each pair of pressures used for the calibration.

The above analysis of CID is somewhat simplified and contains various assumptions. The CID phenomenon, however, is much more complex. The degree of dissociation α is higher for larger clusters and also increases with the internal energy of clusters determined by the ion source temperature [42]. The full analysis of the effect of CID on van't Hoff plots is rather complicated and will depend on exact experimental conditions used to obtain each equilibrium constant on a van't Hoff plot. However, one important result is that HPMS measurements should be undertaken at the lowest possible partial pressures of clustering ligand and overall ion source pressures, as well as an extremely high vacuum in the analyzer. We tried to follow these guidelines in our experiments and the obtained results do not seem to be affected by CID to any appreciable extent.

The problem of unimolecular dissociation has been previously considered in great detail [43]. Ions leaving the ion source have a thermal energy distribution corresponding to the temperature of the ion source that is not preserved in vacuum due to the absence of thermalizing collisions. The energy stored in activated vibrational and rotational energy levels can be used to overcome the dissociation barrier. The fraction of ions that will have enough energy to exceed the threshold energy for unimolecular dissociation is denoted f_{ex}. Depending on the rate constant for unimolecular dissociation at the temperature of the distribution, a larger or smaller part of that fraction will dissociate during the time required for mass analysis.

Once vibrational frequencies and moments of inertia of a cluster are known, the excited fraction can be calculated [43]:

$$f_{ex} = 1 - \frac{1}{Q}\sum_{E_i=0}^{\Delta H} P(E_i)\exp\left(\frac{-E_i}{kT}\right) \tag{4.7}$$

where ΔH for the cluster formation reaction approximates the threshold energy, Q is the partition function, and $P(E_i)$ is the multiplicity of the state with energy E_i. Zero-point energy is the reference energy level. These calculations were performed for all halide clusters measured experimentally using the results from quantum chemical calculations described in Chapter 5. Because of the requirement for angular momentum conservation, the overall rotations were assumed to be unable to provide energy for dissociation. As such, only vibrational frequencies were used in energy calculations and sums of states. Experimental measurements were done at sufficiently low temperatures such that f_{ex} did not normally exceed 0.01. The only exception was the (7,8) hydration step for Cl^-. Even at -80°C the excited fraction for Cl^- cluster with 8 water molecules was calculated to be 0.05. The rigorous method to correct for unimolecular dissociation is to first calculate unimolecular dissociation rate constants from RRKM theory, and use these results to calculate the fraction of f_{ex} that will dissociate during mass analysis. Such calculations were reported by Sunner and Kebarle [43]. However, for these calculations assumptions regarding the properties of the activated complex involved in the dissociation reaction, and in particular its vibrational and rotational states, must be made. This and the use of RRKM theory would introduce errors in addition to the errors in the calculated vibrational frequencies and moments of inertia. For simplicity, it was assumed in our calculations that the entire excited fraction f_{ex} dissociates during mass analysis and the majority of dissociating ions does so only after the acceleration and is rejected by the mass analyzer that includes an ESA in our case. The errors in the corrected ionic ratio due the above

assumptions partially cancel. In addition, the estimated difference between our correction and the correction calculated using unimolecular dissociation rate constants [43] was comparable to observed experimental errors.

Errors in measurements of equilibrium ionic ratios leading to equilibrium constants at a given temperature have been discussed. Another source of experimental error in calculated enthalpy and entropy changes for clustering reactions are errors in temperature measurement. Here we consider two cases: a) errors associated with a temperature sensor itself and b) errors in measuring the reaction temperature. Previous studies using HPMS, normally had temperature measured using a thermocouple, often not calibrated against any temperature standard. When resistance of our ion source PRT is converted to temperature using the manufacturer's conversion tables, the discrepancy between this obtained value and the value from our own calibration data can be as large as 10 degrees at 600K. This stresses the importance of a true rigorous calibration of a temperature sensor. In addition, there is always the question of whether a temperature sensor actually measures true experimental temperature. In HPMS experiments a preheated gas mixture is allowed to flow through the ion source. A common HPMS ion source design incorporates a massive stainless steel block and temperature measured close to the reaction chamber inside the block is taken to be equal to the experimental temperature of the ion source gas. It is possible and indeed probable that the temperature of the gas inside a reaction chamber differs appreciably from the temperature measured by a thermocouple when ion source temperatures are markedly different from the temperature of the preheated gas and especially if the whole source block material is a poor thermal conductor such as stainless steel. The real temperature of the experiment in this case will be closer to the temperature of the preheated gas entering the source than the temperature measured by a thermocouple.

Figure 4.7 shows the dramatic effect that temperature measurement error has on calculated enthalpy changes for two hypothetical reactions with true enthalpy changes having typical values of 48 $kJ \cdot mol^{-1}$ and measured over the temperature ranges 240K-300K and 300K-450K. It was assumed that no temperature measurement error exists at 300K, and that true experimental temperatures at 240K and 450K were closer to 300K than the measured temperatures, 240K and 450K. As shown in Figure 4.7, uncertainties in temperature measurement introduce large errors in calculated enthalpy and entropy changes for a studied reaction. It should be noted that the difference in temperature of gas in the reaction chamber and the source block, if it exists, is expected to become larger at low temperatures because thermal velocities become smaller and

gas densities higher. Under these conditions, longer times are required for the gas to cool down to the temperature of the surrounding ion source block. Figure 4.7 also demonstrates that errors in temperature measurement introduce larger errors in measurements of higher solvation steps, since they are carried out at lower temperatures.

To minimize the possibility of errors due to inaccurate measurement of the temperature, we adopted a slightly different design for the ion source that has been discussed in detail in Chapter 2. The ion source itself is a very small thin-walled stainless steel spool embedded in a massive copper block. The gas inlet and outlet lines are buried in the block over a distance of approximately 10cm immediately adjacent to the source.

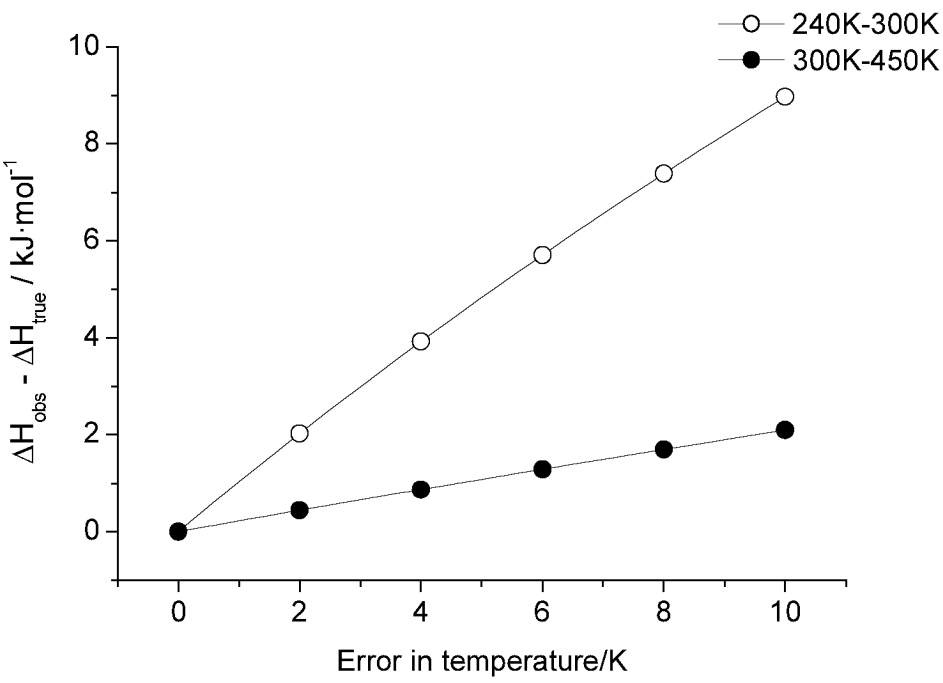

Figure 4.7. Effects of temperature errors on resultant enthalpy changes for two reactions measured over the temperature ranges indicated. It is assumed that there is no temperature error at 300K and the true experimental temperatures at 450K and 240K are closer to 300K than measured by the value plotted on the horizontal axis.

This should ensure that gas entering and leaving the ion source has approximately the same temperature as the ion source itself. The temperature was determined using a 4-wire resistance

method for the PRT embedded directly in the source gas. This PRT was calibrated against a secondary temperature reference standard traceable to NIST ITS-90 standards.

Experimental results

The results for experimentally measured equilibrium constants for Cl^-, Br^-, and I^- stepwise hydration reactions are presented in several van't Hoff plots shown in Figure 4.8. For each of these halides one additional solvation step beyond ones previously measured was directly achieved, as opposed to ref. [39], where equilibrium constants for those reactions were measured at only one or two temperatures and enthalpy changes were calculated using assumed values for the entropy change. For Cl^- two additional steps were successfully measured. As mentioned previously, the last measured hydration step for Cl^- was corrected for unimolecular dissociation using the theoretically calculated excited fraction. As can be seen in Figure 4.8, all data in the van't Hoff plots are linear and no curvature can be distinguished within the experimental scatter. Therefore, enthalpy and entropy changes for halide stepwise hydration reactions calculated from van't Hoff plots and given in Table 4.1 and Table 4.2 are independent of temperature within the observed experimental errors. Errors due to mass discrimination in sampling, as described in Chapter 3, are small compared with experimental errors and, therefore, quantities were not corrected for mass discrimination.

Equilibria containing higher ligand numbers cannot be measured accurately with the present HPMS method. Observation of such equilibria would require low temperatures and high water partial pressures in the source. There is a lower bound of the experimentally usable temperature as water begins to condense in the ion source when its pressure becomes equal to the saturated water vapor pressure at that temperature. Increasing the water partial pressures at higher temperatures will allow observation of larger clusters. However, at high temperatures a significant fraction of large clusters will undergo undesirable unimolecular dissociation during mass analysis and even though measured ionic ratios could be corrected theoretically, such results would be of significantly lower accuracy. In addition to the uncertainty of the unimolecular dissociation correction, the use of high partial water pressures would strongly enhance the collision induced dissociation effect on measured ionic ratios as was shown previously in Figures 4.4 and 4.5. The effect of CID is more difficult to estimate quantitatively and the accuracy of the ionic ratios corrected for both unimolecular dissociation and CID would be even lower.

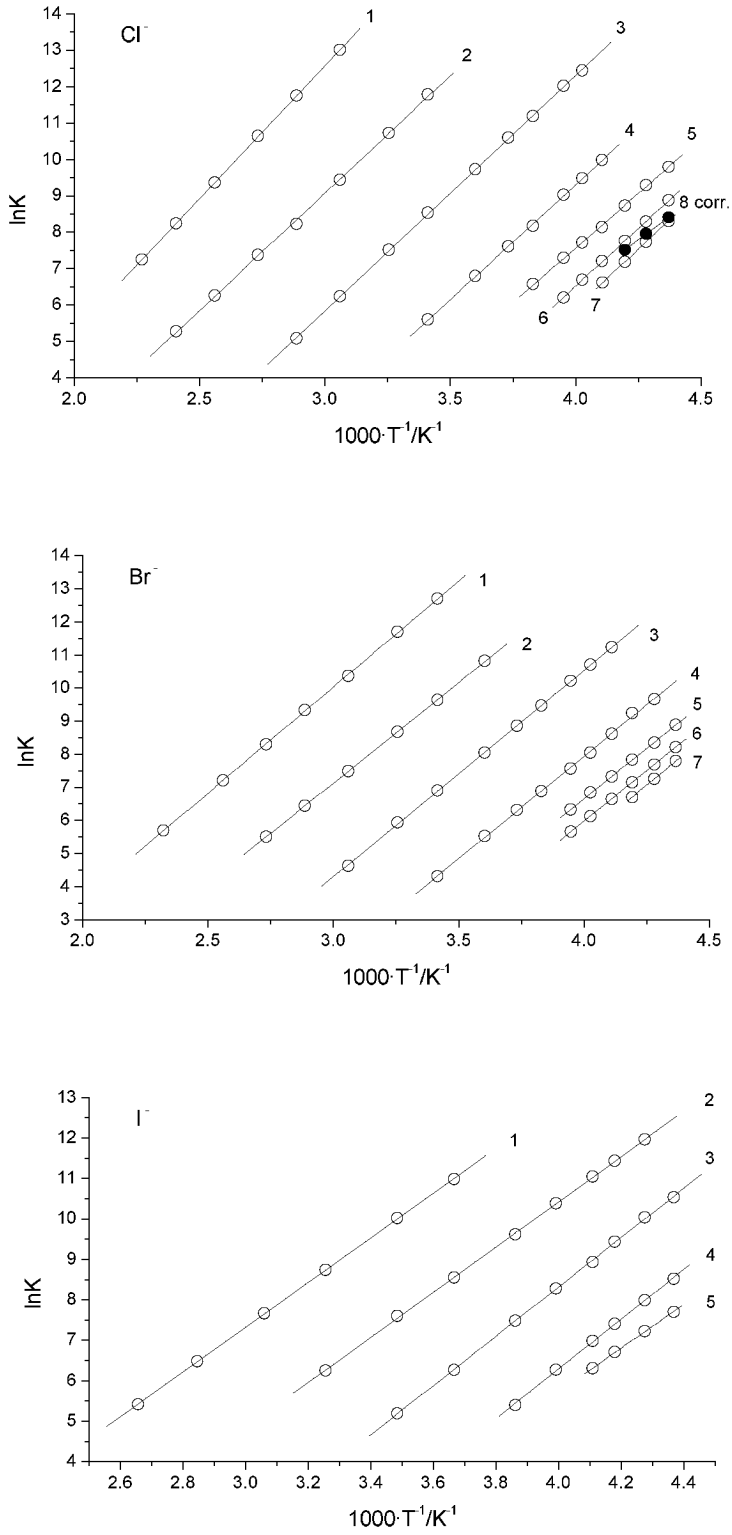

Figure 4.8. Experimental van't Hoff plots for halide water clusters.

n	Cl^-	Br^-	I^-
1	60.7±2.1	53.4±1.7	46.0±1.7
2	53.6±1.3	50.6±1.3	46.5±1.7
3	53.8±1.7	52.0±1.3	50.7±2.1
4	52.5±1.7	51.6±1.7	51.1±2.5
5	49.7±2.1	50.5±2.1	44.9±2.5
6	52.7±2.5	50.9±2.5	—
7	53.3±2.5	52.4±2.9	—
8	42.5±5.0	—	—
8	(49.8)	—	—

Table 4.1. Experimentally determined values for $-\Delta H°_{n-1,n}$ [$kJ \cdot mol^{-1}$] for halide hydration reactions (4.1). Standard pressure is 1000 mbar. Values in parenthesis are data not corrected for unimolecular dissociation.

n	Cl^-	Br^-	I^-
1	77.5±6.3	76.7±6.3	77.0±4.2
2	85.5±5.0	92.5±4.2	99.1±4.2
3	112.7±5.9	120.3±4.2	133.5±8.4
4	132.6±6.3	140.3±6.3	152±11
5	136.0±7.5	146.6±8.4	132±11
6	156.6±8.4	153.7±8.4	—
7	163.9±8.4	164±11	—
8	116±17	—	—
8	(152)	—	—

Table 4.2. Experimentally determined values for $-\Delta S°_{n-1,n}$ [$J \cdot mol^{-1} \cdot K^{-1}$] for halide hydration reactions (4.1). Standard pressure is 1000 mbar. Values in parenthesis are data not corrected for unimolecular dissociation.

Comparisons of our data with previous experimental results and density functional theory (DFT) calculations are shown in Figures 4.9 through 4.11. There is obvious disagreement between the present results and earlier experimental data for higher hydration steps but good agreement with DFT calculations, especially for the stepwise trends in enthalpy and entropy changes. Results for enthalpies are shifted upward compared with previous results and exhibit non-monotonic dependence with cluster size. The upward shift is most likely a result of uncertainties in temperature measurement in earlier HPMS designs.

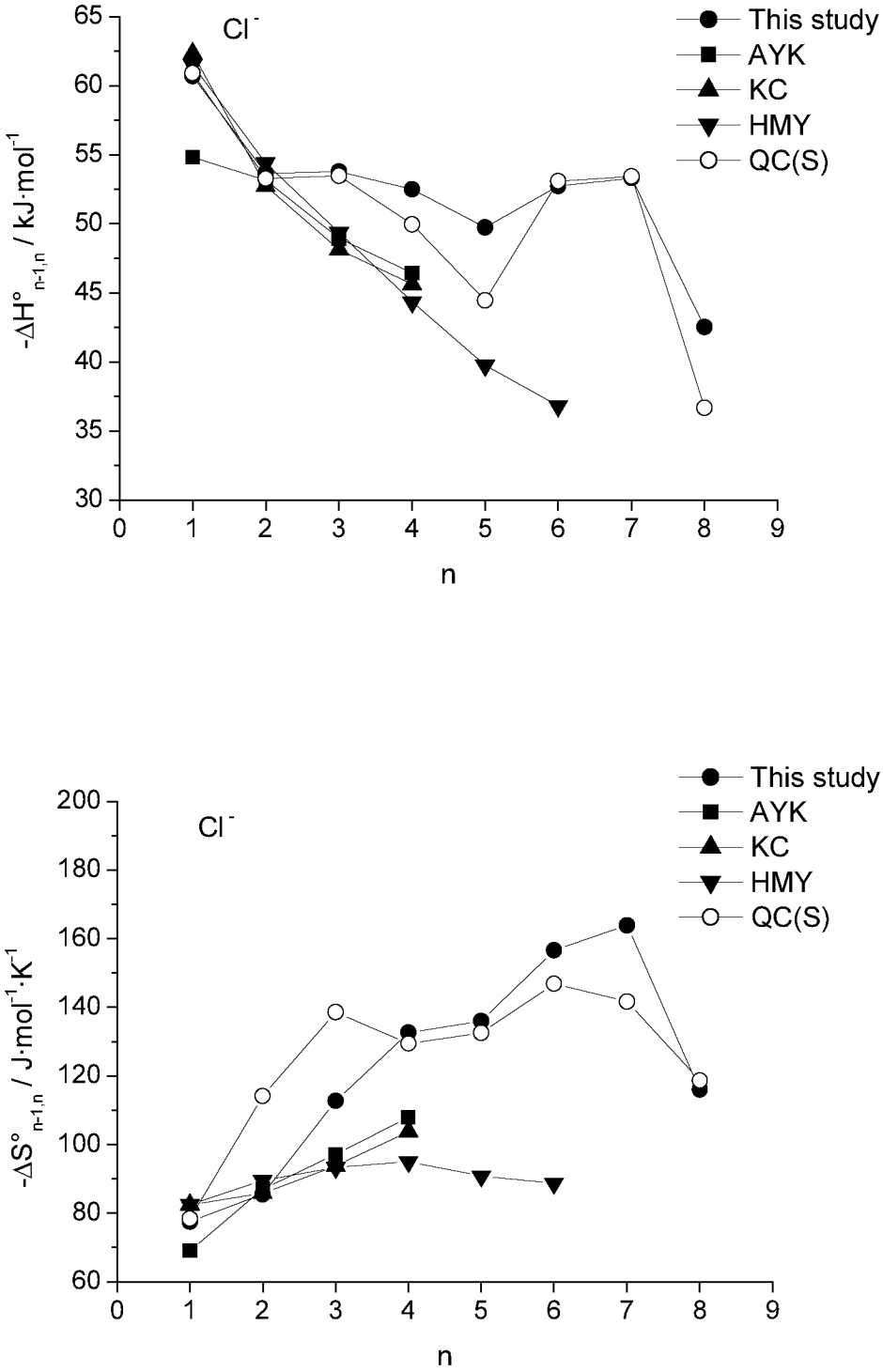

Figure 4.9. Comparison of enthalpy and entropy changes for Cl^- hydration reactions obtained in this work with previous data and calculations. AYK – data from ref. [38], KC – data from ref. [37], HMY – data from ref. [39], QC(S) - DFT calculations for surface geometries from Chapter 5.

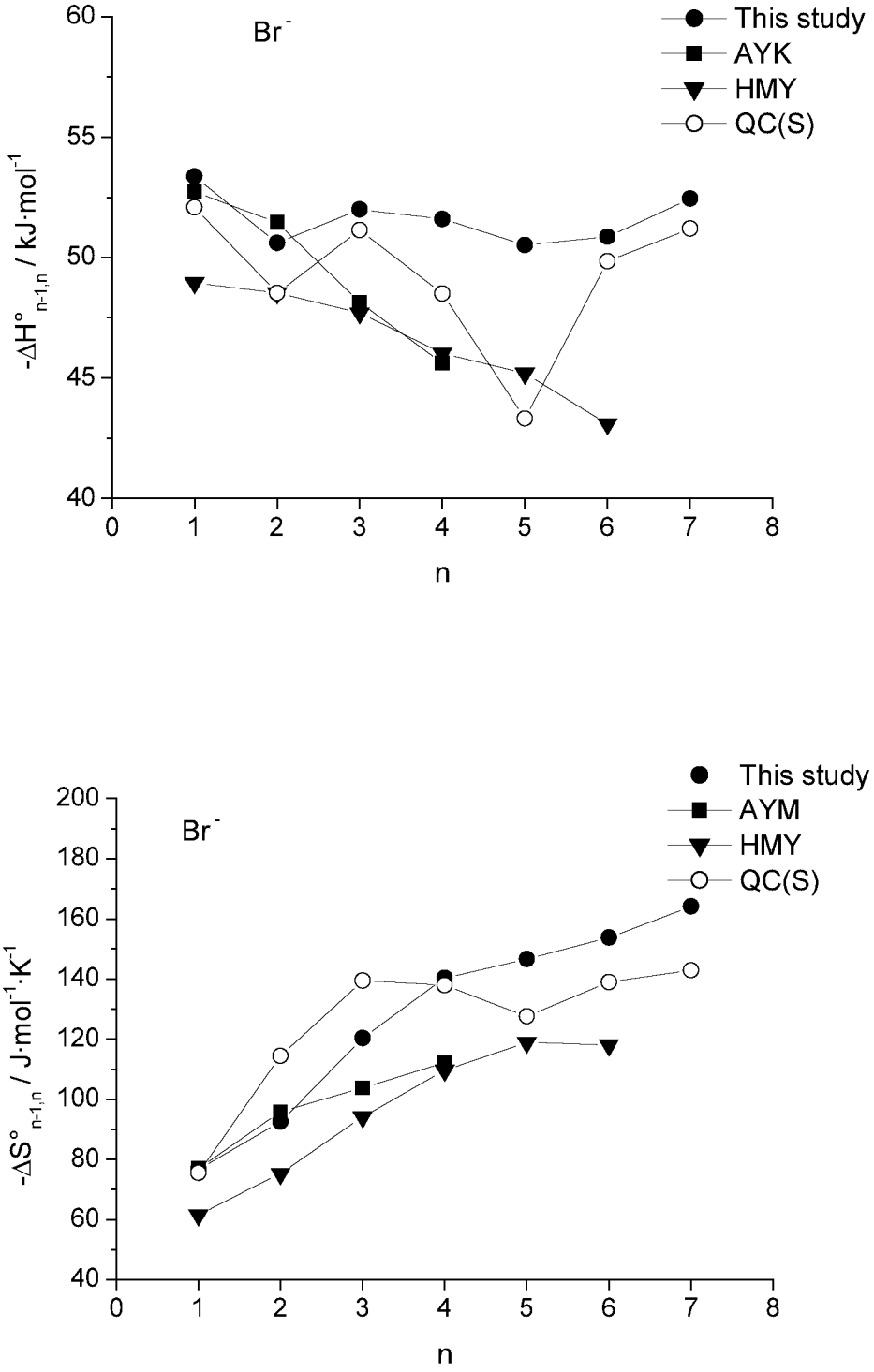

Figure 4.10. Comparison of enthalpy and entropy changes for Br^- hydration reactions obtained in this work with previous data and calculations. AYK – data from ref. [38], HMY – data from ref. [39], QC(S) - DFT calculations for surface geometries from Chapter 5.

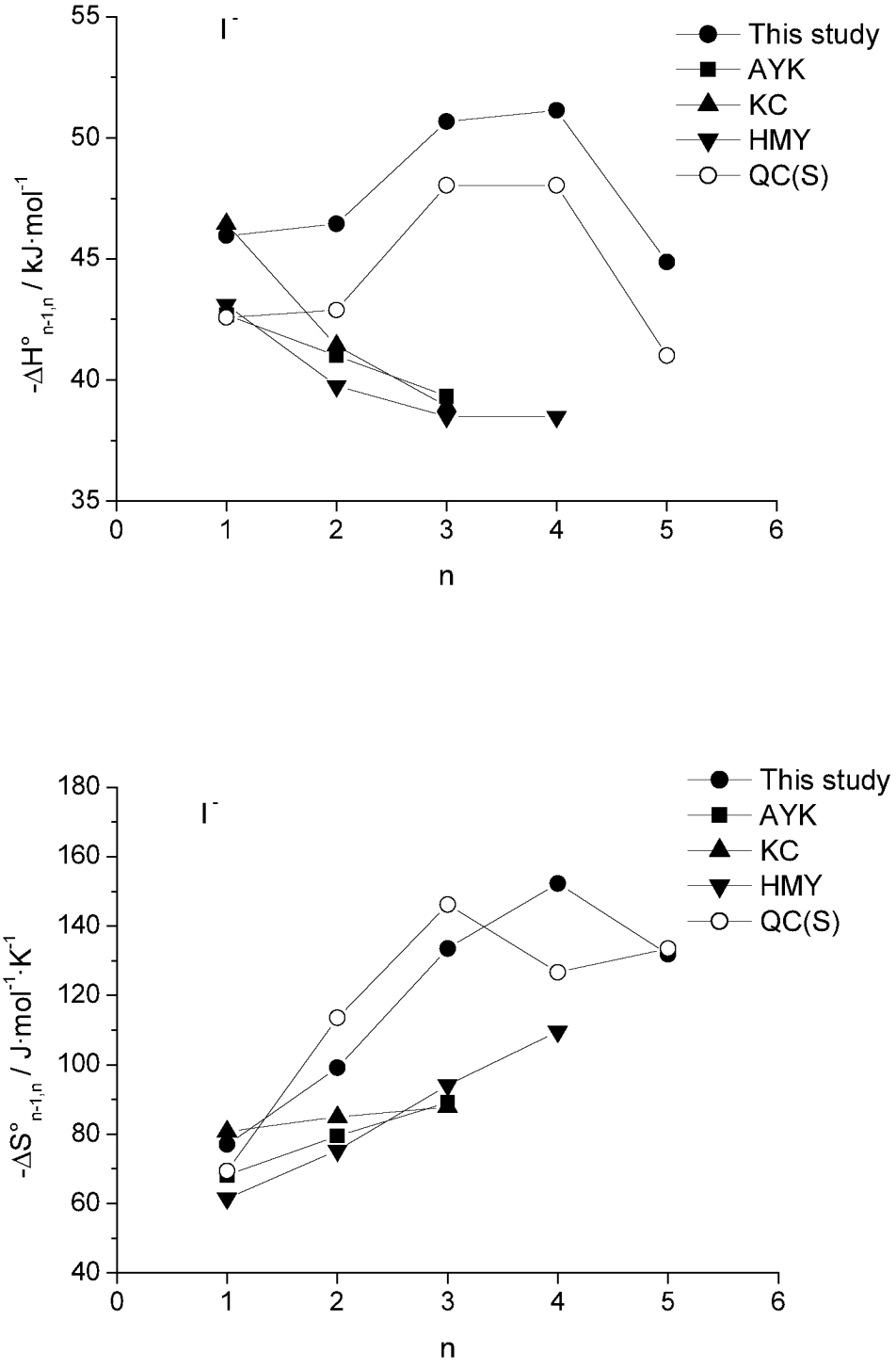

Figure 4.11. Comparison of enthalpy and entropy changes for I^- hydration reactions obtained in this work with previous data and calculations. AYK – data from ref. [38], KC – data from ref. [37], HMY – data from ref. [39], QC(S) - DFT calculations for surface geometries from Chapter 5.

The effect of temperature accuracy on the van't Hoff plots and subsequently calculated thermodynamic quantities has been previously discussed in this chapter. The disagreement is largest for reactions measured at low temperatures, which is consistent with the assumption of temperature measurement errors as is shown in Figure 4.7. In addition to temperature errors, a smaller contribution to the differences between present and earlier data might arise from possible CID problems in previous determinations. The effect of CID on van't Hoff plots and calculated thermodynamic quantities has also been discussed in detail earlier in this chapter. Ion source pressures of 3-4 Torr cited in ref. [37-39] might be too high for measurements at low temperatures. For comparison, pressure ranges used at different temperatures for these results are shown in Figure 2.4. The absence of non-monotonic trends for higher solvation steps in previous determinations should not have resulted from temperature errors alone, as these last steps are normally measured over similar temperature ranges. The appearance of the non-monotonic trends in our results is attributed in part to an improved energy resolution in the present HPMS setup. This is a result of an increased sensitivity of the mass spectrometer due to higher acceleration voltages, improved ion optics, and the use of a data system for unambiguous mass tuning.

Obtained gas-phase data can be compared with thermochemical data for bulk solvation through consideration of differential integrated thermochemical values for gas-phase hydration. Such comparisons were previously reported by Kebarle [38]. Measurement of the total enthalpy of solvation in bulk solvent necessarily involves a cation and an anion due to the requirement of electroneutrality. Taking differences of such enthalpies of solvation for two anions having a common cation cancels the contribution of the cation.

In gas-phase measurements, integrated enthalpy of hydration data for a cluster of size n is defined as a sum of enthalpy changes for all hydration steps up to n:

$$\Delta H^{\circ}_{0,n}(\mathrm{X}) = \sum_{i=1}^{n} \Delta H^{\circ}_{i}(\mathrm{X}) \tag{4.8}$$

The differential integrated enthalpy of hydration is then defined as the difference between integrated enthalpies of hydration of two anions, X_1 and X_2:

$$\Delta H^{\circ}_{0,n}(\mathrm{X}_1,\mathrm{X}_2) = \Delta H^{\circ}_{0,n}(\mathrm{X}_1) - \Delta H^{\circ}_{0,n}(\mathrm{X}_2) \tag{4.9}$$

The differential integrated enthalpy as a function of cluster size n approaches that for bulk solvation at sufficiently large n. The results of such a treatment are shown in Figure 4.12. The values for bulk solvation at $n=\infty$ were calculated from enthalpies of transfer of halogen anions

from gas-phase to water using the NBS tables [44]. Differential enthalpies of solvation in the liquid phase can be calculated using the Born equation that yields free energies of solvation involving only the ionic radius and dielectric constant of water. The value of entropy needed for calculation of the enthalpy is obtained by taking the partial derivative of the free energy with respect to temperature at constant pressure using the dielectric constant formulation of Archer and Wang [45] that employs Hill's equation of state for water [46]. Differential enthalpies calculated using the Born equation are given on the right hand side of Figure 4.12. The ionic radii in these calculations were obtained from the calculations described in Chapter 5. As can be seen, the gas-phase enthalpies are still removed from the values for bulk hydration even at n=7. It is worth noting that the differential integrated enthalpies with n=3 or 4, corresponding to the number of water molecules directly bound to the anion, combined with the differential enthalpies calculated using the Born equation are close to differential enthalpies for bulk solvation. This combination of an explicitly treated first solvation shell and a continuum representation of the rest of solvent forms a useful basis for a solvation theory [1-3].

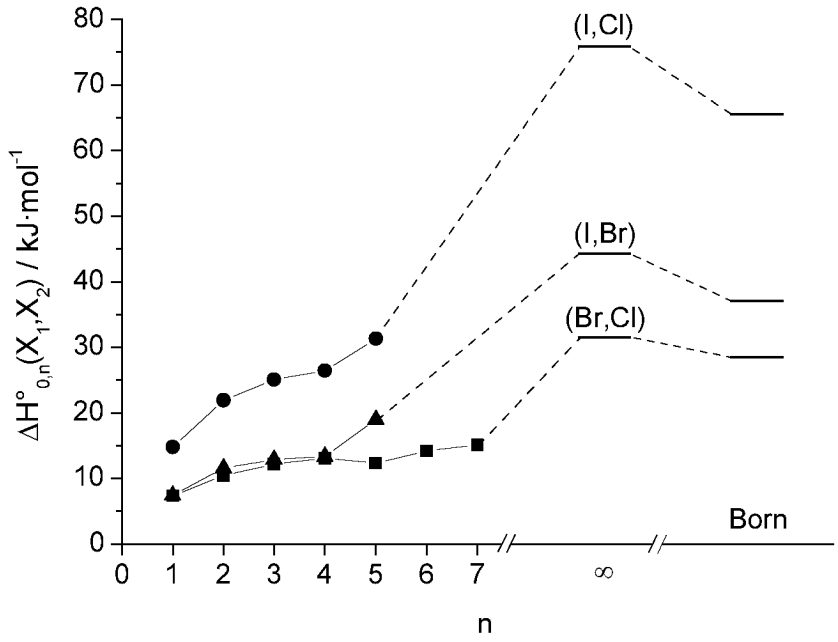

Figure 4.12. Pairwise differential integrated enthalpies of hydration for halides and comparison with ultimate (n=∞) differential enthalpies for transfer of halogen anions from gas phase into aqueous solution calculated using experimental data from the NBS tables [44] and the Born equation.

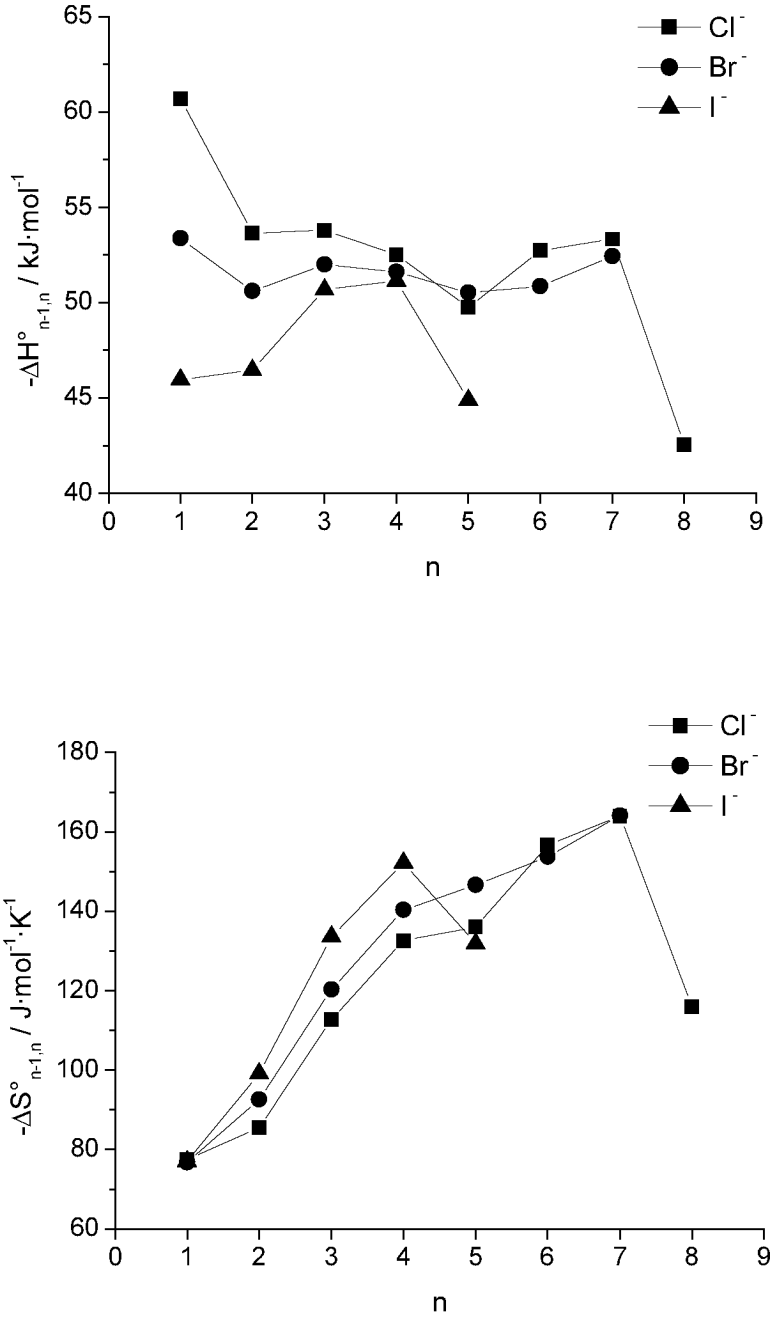

Figure 4.13. Comparison of stepwise enthalpies and entropies of hydration for studied halides.

Stepwise enthalpies and entropies of hydration for halides studied are plotted together in Figure 4.13. The hydration strength decreases from Cl^- to I^- with an increase in ionic radius, as

expected. This conclusion can also be reached indirectly by the fact that at the lowest experimental temperature, the largest observed cluster for Cl^- was n=8, whereas for I^- the largest cluster was n=5 under similar experimental conditions. Common to all studied halides is the non-monotonic behavior of stepwise enthalpies and entropies with cluster size.

Water molecules in halide water clusters are attached to the anion and other water molecules through hydrogen bonds. As a result, ion-solvent and solvent-solvent interactions in these clusters can be approximately of the same magnitude. Non-monotonic dependence of stepwise thermochemical values on cluster size demonstrates the competition between these two types of interactions. Oscillations in the thermochemical values are superimposed on the gradual decrease in negative enthalpies and gradual increase in negative entropies. The magnitudes of stepwise enthalpy approach the value 45 $kJ \cdot mol^{-1}$ for large n, which is comparable to the molar enthalpy of evaporation of water at room temperature. As suggested in ref. [38], the increase in negative stepwise entropies reflects the restriction in freedom of water molecules with increasing cluster size. A meaningful interpretation of the trends in stepwise thermochemical values requires knowledge of cluster structures and is given in Chapter 5.

4.4 Conclusions

Stepwise hydration reactions of halide water clusters were investigated using a newly constructed high-pressure mass spectrometer. Clusters of larger size than have been previously reported were observed and studied. The largest experimentally observed clusters were n=8 for Cl^-, n=7 for Br^-, and n=5 for I^-. Stepwise enthalpy and entropy changes calculated from these experimental data show a non-monotonic dependence on cluster size. Such behavior is consistent with quantum mechanical calculations, but inconsistent with earlier experimental investigations. The present results also show an overall shift in enthalpy changes compared with previous data. It is suggested that these differences are the result of an improved temperature accuracy and increased mass spectrometer sensitivity in the present HPMS apparatus compared with earlier HPMS designs. Non-monotonic behavior of thermochemical values demonstrates the competition between ion-solvent and solvent-solvent interactions. Gas-phase differential integrated enthalpies of solvation calculated from the obtained results approach quantities for bulk solvation with increasing cluster size, but are still expectedly removed even for the largest pair of clusters with n=7.

Chapter 5. Quantum Mechanical Calculations on Halide Water Clusters

5.1 Introduction

Numerous theoretical and experimental studies have been concerned with the stepwise solvation of positive and negative ions. Such investigations of microsolvation provide extremely important information for understanding the behavior of ions in solutions. Recent extensive theoretical investigations include those of Combariza *et al.* [47-49] for the investigation of $X^-(H_2O)_n$ clusters, (X=Cl, Br, I; n=1-6 for Cl and Br and n=1-8 for I) at the MP2 level with SCF geometries and Ayala *et al.* [50] for the investigation of $Br^-(H_2O)_n$ (n=1-8) using DFT (B3LYP). A large number of reported calculations by other authors were concerned with smaller clusters up to 4 water molecules and studied the effects of various computational methods and basis sets on resultant optimized geometries. Here results from our DFT quantum-chemical study of hydration of halides in clusters $X^-(H_2O)_n$, (X=Cl, Br, I; n=1-8) are presented. These calculations were carried out in conjunction with the high-pressure mass spectrometric measurements on the same chemical systems to aid in interpretation of the results.

5.2 Computational methods

Full geometry optimizations and frequency calculations were performed with the hybrid B3LYP method using GAUSSIAN98 [51] software. The Cl, Br, H, and O atoms were described using GAUSSIAN98's built-in 6-311++G** basis set that includes polarization and diffuse functions. For iodine the CRENBL ECP effective core potential basis set [52] was used. Starting with n=2, two distinct geometry types were considered for each of the halides: one with the anion surrounded by water molecules, corresponding to interior solvation (I) and the other with the anion bound to the surface of a water cluster, corresponding to surface solvation (S). We considered one isomer of each type (surface and interior) for each cluster size. Structures similar to those reported by previous investigations [47-50] were used as starting geometries for the optimizations. Subsequent frequency calculations were used to verify that a

resultant optimized structure is indeed a minimum on the potential energy surface and to obtain thermochemical information as a function of temperature. All frequencies were scaled using a common factor of 0.89. Use of a scaling factor of 1.0 does not change calculated enthalpies and entropies for stepwise hydration reactions significantly. Typical changes for enthalpy and entropy are only 0.8 $kJ \cdot mol^{-1}$ and 2 $J \cdot mol^{-1} \cdot K^{-1}$, whereas typical experimental uncertainties are 2 $kJ \cdot mol^{-1}$ and 4 $J \cdot mol^{-1} \cdot K^{-1}$, respectively.

5.3 Results and discussion

Cluster geometries

Optimized geometries are shown in Figure 5.1. All of the geometries correspond to local minima on potential energy surfaces, as verified by the frequency calculations. The maximum size for optimized clusters for all halides was n=8 for both surface and interior states. No stable interior type geometry could be found for n=8 for iodide. In addition, no interior structures could be found for bromide for n=2,3. For n=2 the optimized geometry was a saddle point on the potential energy surface and for n=3 the initial interior type geometry converged to that of the surface type. It would appear from Figure 5.1 that there is an apparent anomaly among the interior geometries at n=5 and n=7. It seems more likely that iodide clusters would form structures more similar to bromide than chloride. Results of these calculations, however, suggest that for iodide the Br-like geometry at n=5 was more stable by 4 $kJ \cdot mol^{-1}$ over the Cl-like structure. The Br-like initial geometry for iodide at n=7 converged to the Cl-like geometry. This is attributed to basis set effects, since an ECP basis set was used for iodide, while Cl and Br were described by the 6-311++G** basis set. Accordingly for the same reason, no stable interior type geometries could be resolved for bromide at n=2,3, whereas for n=3 a stable interior structure was found by Ayala *et al.* [50] using a smaller basis set. It should be noted that optimized geometries in Figure 5.1 are representative and hopefully are the most stable geometries for each type, surface or interior. Potential energy surfaces, however, have many local minima corresponding to structures of both types, the number of which rapidly increases with increasing cluster size. A molecular dynamics investigation of chloride water clusters [53] found at least 40 local minima for n=6.

Figure 5.2 shows the distances between halogen anion and oxygen atoms for all clusters shown in Figure 5.1. As expected, the anion-oxygen distances increase with increasing ionic radius. The distances for water molecules directly bound to an anion decrease with cluster size for the surface structures and increase for interior structures. The outermost water molecules

tend to push the innermost waters closer to the anion in surface clusters, whereas for the interior clusters considered all water molecules are directly bound to the anion.

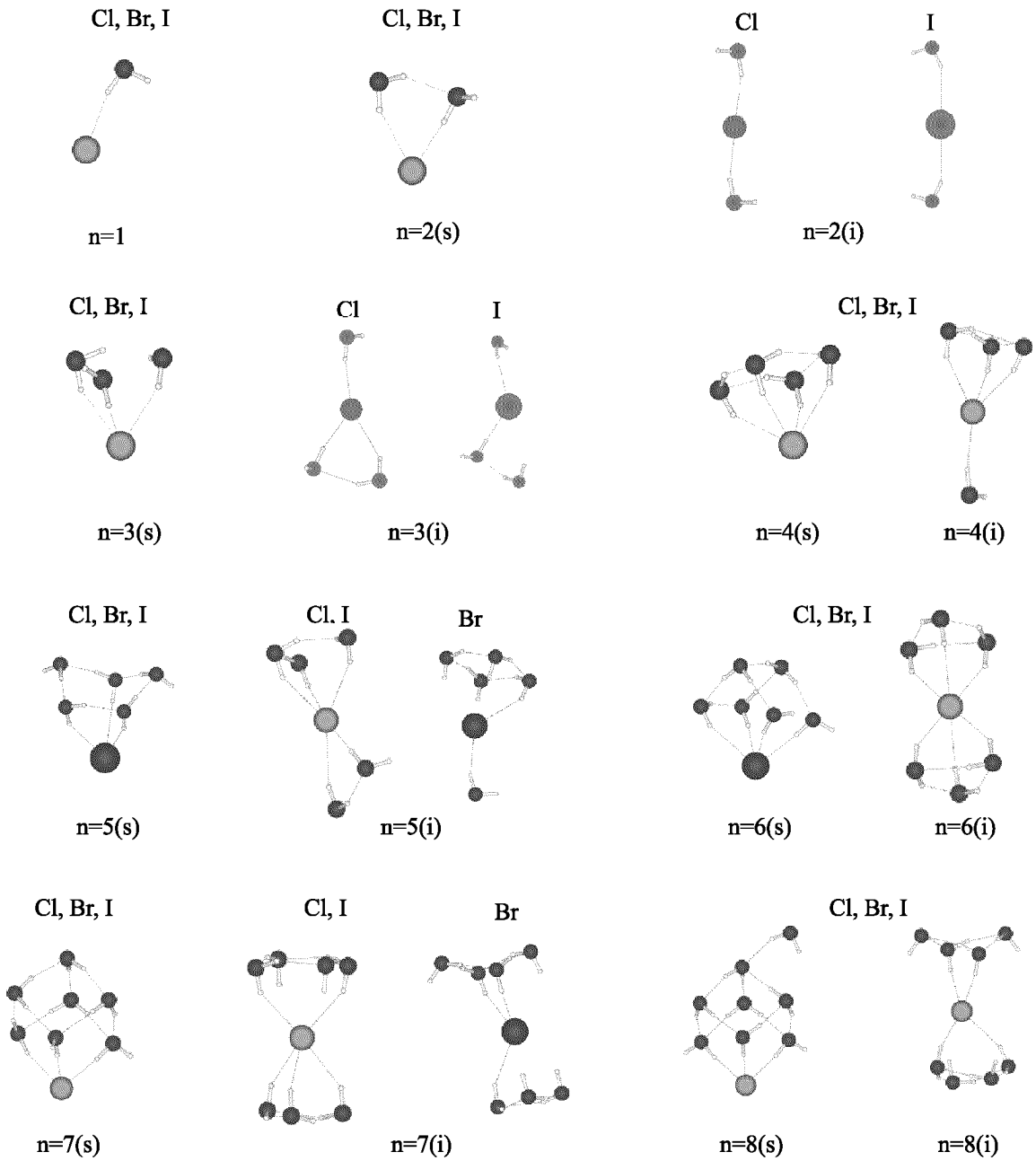

Figure 5.1. Optimized surface (S) and interior (I) solvation geometries for halide water clusters.

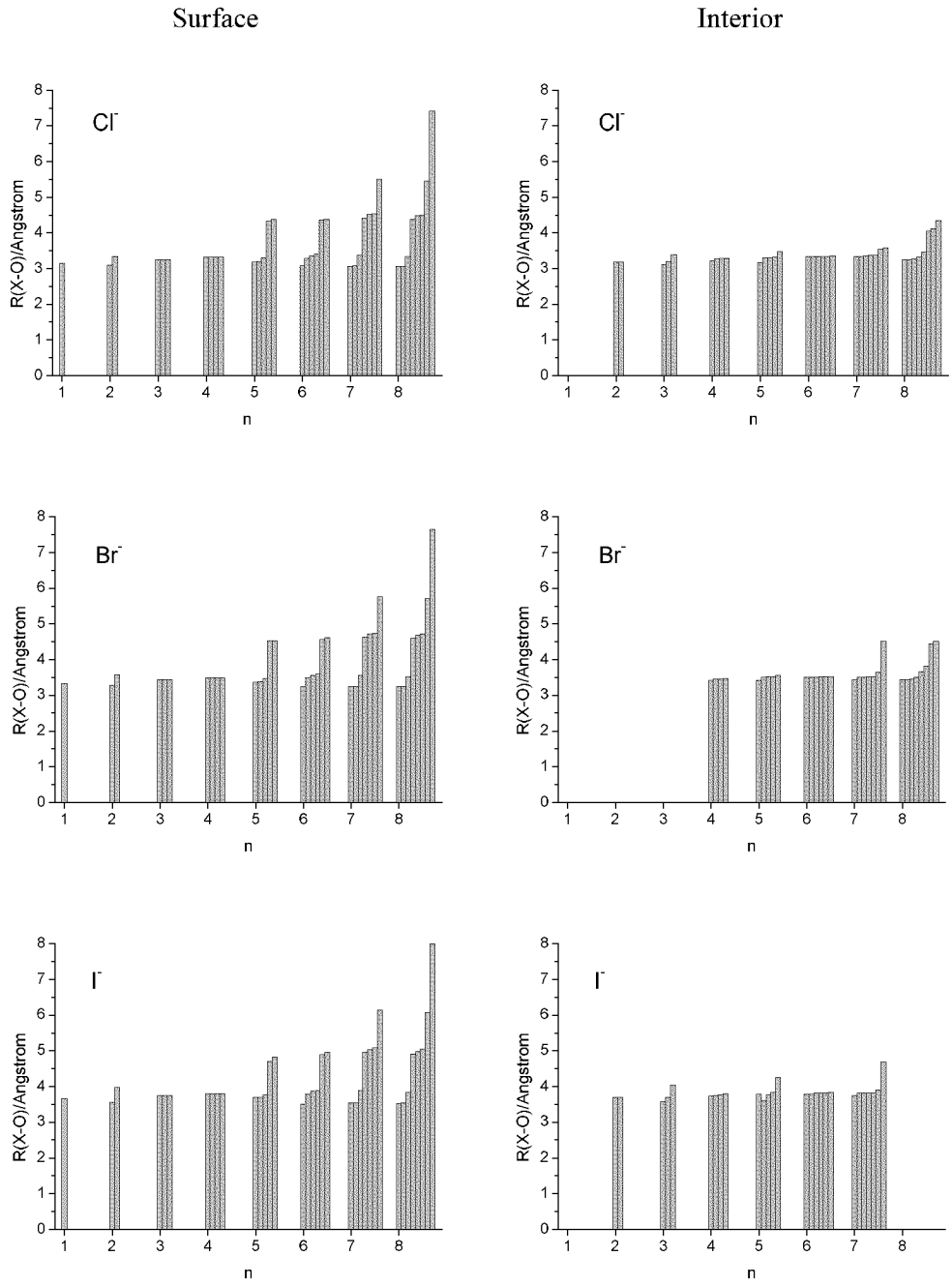

Figure 5.2. Halide-Oxygen distances for surface and interior clusters.

Calculation of the excited fraction

The knowledge of cluster vibrational frequencies and moments of inertia allows for calculation of the energy distribution for the clusters and, in particular, calculation of the fraction f_{ex} of clusters having energies above the dissociation threshold energy. This information is important for experimental studies that measure clustering equilibria as it allows

the choice of experimental conditions where clusters are most stable and hence will not undergo unimolecular dissociation during mass analysis. The problem of unimolecular dissociation in high-pressure mass spectrometry was considered in detail previously by Sunner and Kebarle [43].

Once vibrational frequencies and moments of inertia of a cluster are known, the exited fraction f_{ex} can be calculated by:

$$f_{ex} = 1 - \frac{1}{Q} \sum_{E_i=0}^{\Delta H} P(E_i) \exp\left(\frac{-E_i}{kT}\right) \tag{5.1}$$

where $-\Delta H$ for the cluster formation reaction approximates the threshold energy, Q is partition function, and $P(E_i)$ is multiplicity of a state with energy E_i. Zero-point energy is the reference energy level and the sum is taken over all states with energies ranging from 0 to $-\Delta H$. Because of the requirement that angular momentum is conserved, the overall rotations were assumed to be unable to provide energy for dissociation. As such, only vibrational frequencies were used in energy calculations and sums of states. Multiplicities of vibrational states were computed using the Beyer-Swinehart algorithm for counting states [54]. These calculations were carried out for all clusters shown in Figure 5.1. The temperature dependence of the excited fraction for halide water clusters is shown in Figure 5.3. With only a few exceptions, the excited fraction at any temperature is larger for interior structures than for the corresponding surface structures. This is a consequence of normally smaller stepwise hydration enthalpies for interior clusters compared with surface clusters, as will be discussed in the next section.

Surface versus interior solvated states

As previously mentioned, many stable isomers of surface and interior type structures corresponding to local minima of various depth and shape on a potential energy surface exist. At elevated temperatures all minima are populated to some varying extent and can be considered to be a statistical ensemble. The question of which geometry type prevails in halide water clusters has been the subject of considerable interest in recent years. Quantum mechanical calculations can only explore a limited number of local minima. A structure close to that corresponding at a minimum has to be provided as an input to the geometry optimization for each minimum on the potential energy surface, consequently, all minima have to be known *a priori*.

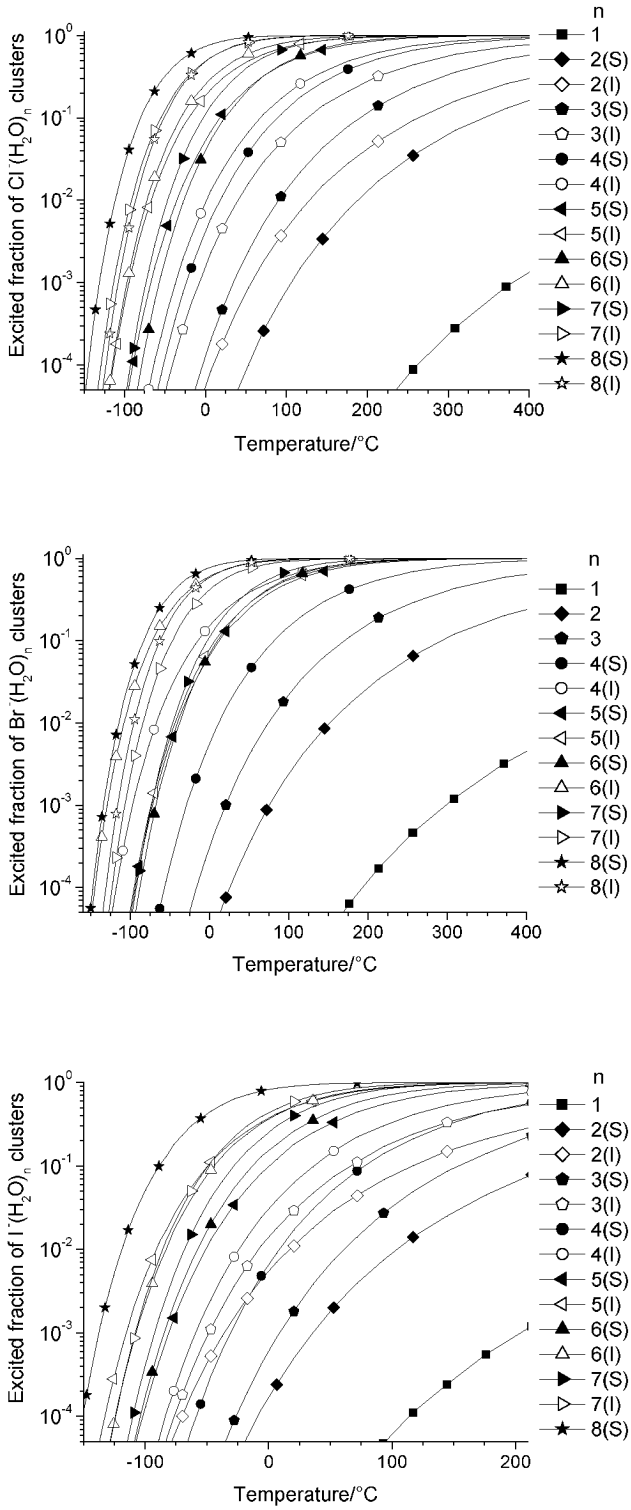

Figure 5.3. Fraction of clusters with energies exceeding the dissociation threshold.

While quantum mechanical results are suitable for a comparative analysis of selected geometries and can qualitatively describe the temperature trends of the statistical ensemble, they do not provide sufficient information to make quantitative predictions regarding which geometry type prevails under a given set of conditions. In contrast, molecular dynamics simulations allow a more detailed sampling of the potential energy surface. Results from MD simulations are often strongly dependent on the interaction potentials used. Most MD simulations for halide water clusters postulate surface solvation for Cl^-, Br^-, and I^- clusters [55-59]. However, when different interaction potentials are used, MD simulations may also predict dominance of interior structures at elevated temperatures [60, 61].

Comparison of ground state and total energies for interior and surface clusters from Figure 5.1 shows that surface clusters are energetically more stable. The stabilization energies are plotted as a function of temperature and are shown in Figure 5.4. The stabilization energy is defined as the difference between total energies of surface and interior clusters. The differences between ground state energies and total energies of surface and interior structures obtained with the present combination of the B3LYP method and basis sets are larger than those obtained with the methods used by Combariza *et al.* [47-49] and are of the same sign. Interior structures were found to have lower vibrational frequencies than surface structures. This is due to the fact that water molecules in surface clusters form more rigid hydrogen-bonding networks [61]. This also implies that surface clusters correspond to deeper minima or quantum wells on the potential energy surfaces that would also have steeper potential walls. The abundance of low frequency normal modes in interior clusters leads to a higher density of states than existing in surface structures. As such, the result that surface states are more energetically stable does not guarantee that at finite temperatures surface states will be predominantly populated. As shown in ref. [61], the fraction of interior structures calculated for Cl^- clusters up to n=3 increases from 0 to nearly 100% as the temperature is raised. Following ref. [61], we have considered a hypothetical system consisting of one surface and one interior structure at each cluster size. In such a system the fraction of interior states, F, is given by:

$$F = \frac{Q_i}{Q_i + Q_s} \tag{5.2}$$

where Q_i and Q_s are partition functions for interior and surface states, respectively. The fraction of interior structures as a function of temperature is shown in Figure 5.5. For all studied ions and cluster sizes, interior structures dominate at higher temperatures within this model.

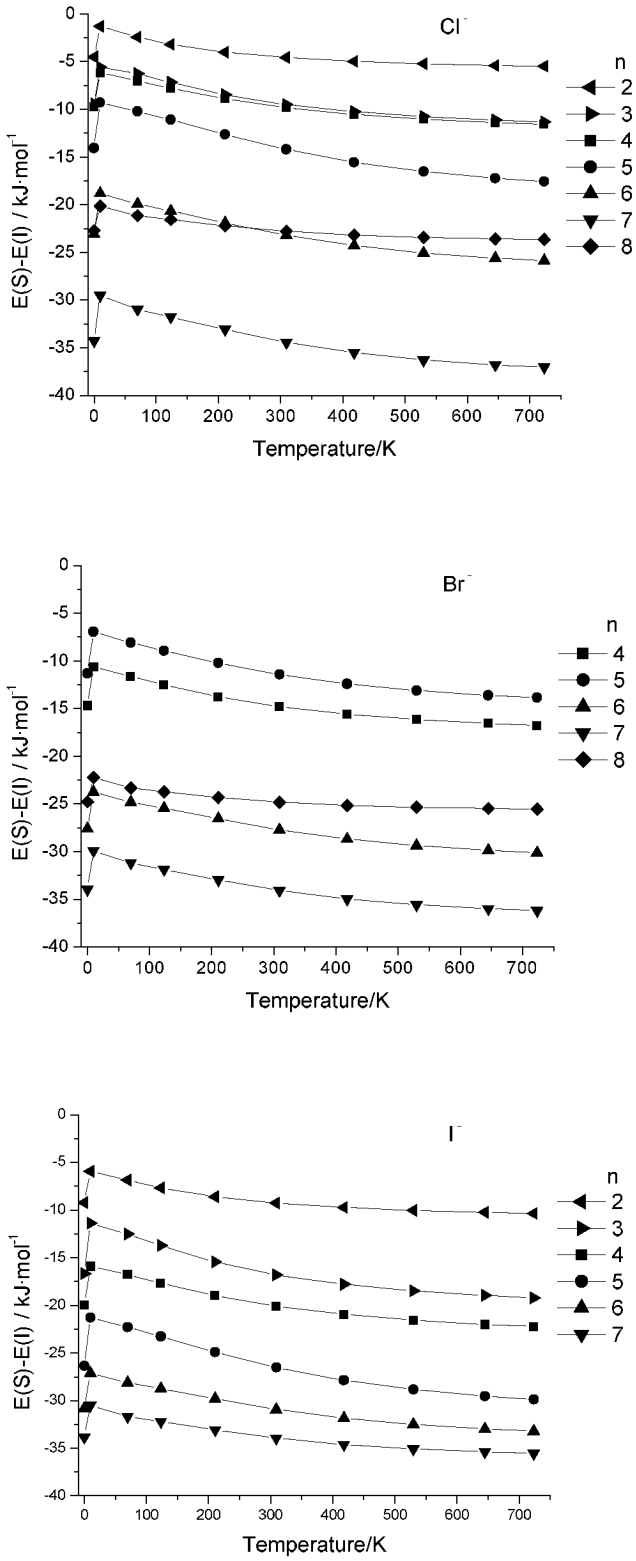

Figure 5.4. Stabilization energies for surface compared with interior clusters. Negative values correspond to surface structures being more stable.

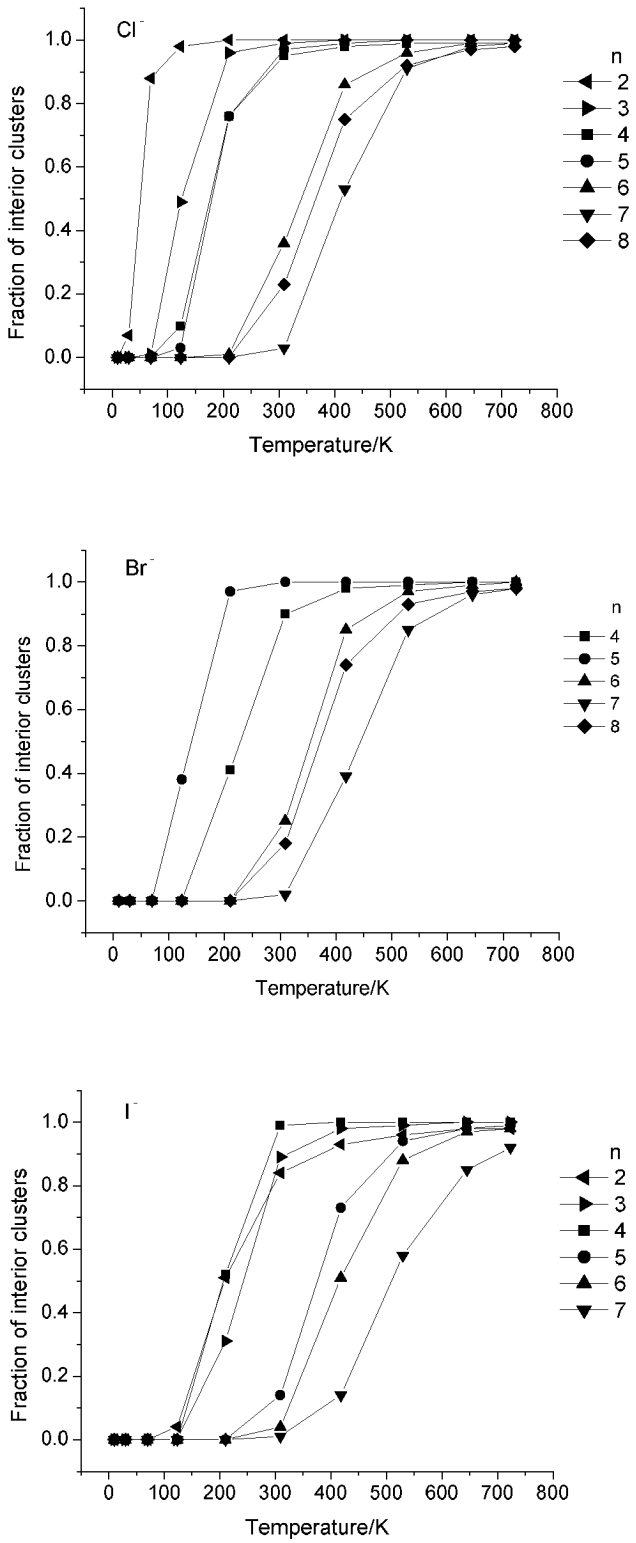

Figure 5.5. Fraction of interior structures in a model system with one surface and one interior isomer for each cluster size.

An attempt can be made to model the clustering equilibria measured with high-pressure mass spectrometric methods using this simple hypothetical system. The equilibrium concentrations of surface and interior clusters of size *n* inside a high-pressure ion source are related by Eq. (5.2). If a significant fraction of clusters exiting the ion source have energies above the dissociation threshold, a correction taking into account unimolecular dissociation must be made for detected ions. An exact treatment of unimolecular dissociation requires knowledge of the unimolecular dissociation rate constants as a function of cluster energy and also detailed knowledge of the electric potential profile along the ion trajectory of the mass spectrometer. The type of mass spectrometer also plays an important role. For a forward geometry magnetic sector mass spectrometer (EB) that was used in our experiments there are the following possibilities: a) clusters of size *n* that dissociate in the field-free region upon exit from the ion source yet before acceleration will be detected as *n-1* clusters; b) clusters dissociating after the acceleration but before the electrostatic analyzer will be rejected by the analyzer; c) clusters of size *n* that dissociate in the field-free region between the analyzer and the magnet will be detected as *n-1* clusters; d) clusters dissociating after the magnet will still be detected as clusters of size *n*. Because our post-source true field-free region is quite short and excited fractions decay exponentially with time, most clusters that dissociate will do so after acceleration electrodes but before the electrostatic analyzer and thus will be rejected by the analyzer. Since our model is quite simple, we will use the assumption that the entire excited fraction dissociates during mass analysis and does not get detected as clusters of size *n-1*. The detected fraction can thus be described by $\left(1-f_{ex}\right)$. Consequently, the observed equilibrium constant for the *n*-th hydration step is given by:

$$K_n^{\text{obs}} = \frac{1000\left[C_n^s\left(1-f_n^s\right)+C_n^i\left(1-f_n^i\right)\right]}{p\left(\mathrm{H_2O}\right)\left[C_{n-1}^s\left(1-f_{n-1}^s\right)+C_{n-1}^i\left(1-f_{n-1}^i\right)\right]} \tag{5.3}$$

where C_n's are equilibrium concentrations, f_n's the excited fractions, $p\left(\mathrm{H_2O}\right)$ is the partial pressure of water in mbar, the indices *i* and *s* designate interior and surface clusters, respectively and the 1000 refers to the standard state pressure in mbar. The equilibrium concentrations, C_n and C_{n-1}, for each geometry type are related by the "partial equilibrium constant":

$$K_n^a = \frac{1000C_n^a}{p\left(\mathrm{H_2O}\right)C_{n-1}^a} \tag{5.4}$$

where a designates the structure type and can be either i or s. The partial equilibrium constants for surface and interior structures can be calculated from the quantum mechanical results. After simple algebraic rearrangement, the observed equilibrium constant can be expressed in terms of these partial equilibrium constants, the excited fractions for interior and surface structures, and the fractions of interior states for n-1 and n clusters. Theoretical van't Hoff plots were constructed using the equilibrium constants described by Eq. (5.3). Enthalpy and entropy changes for stepwise hydration reactions for the model system containing both interior and surface clusters were calculated from these van't Hoff plots using the same experimental temperature ranges. In addition, enthalpies and entropies were calculated for reactions involving only surface and only interior clusters, again using experimental temperature ranges. Comparison of these theoretical and experimental results for stepwise hydration reactions of halides are given in Figures 5.6 through 5.8. Analysis of the interior states fraction within the experimental temperature ranges shows that for $n<6$ the population of interior states in the model system is significantly higher than that for surface states. Analysis of excited fractions within the experimental temperature ranges shows that for $n<5$ interior structures will not dissociate significantly during mass analysis. It follows from these results that for up to 4-5 clustering waters the experimentally measured equilibria involve predominantly interior clusters. However, as can be seen in Figures 5.6 through 5.8, the theoretical values for enthalpies and entropies of stepwise clustering reactions for surface structures agree much better with the experimental data than the values for the model system or values for interior clusters. The only exception might occur at $n=2$ for chloride, where both experimental enthalpy and entropy agree better with those for the model system. The model system is limited since it assumes an equal number of surface and interior geometries for each cluster size, whereas the number of surface structures for small clusters might be far greater than the number of interior structures [53]. Nevertheless, the model system does demonstrate the temperature-dependent competition between surface and interior states. While the experimental results suggest that surface structures prevail over interior structures for all but one of the clusters considered, a quantitative description of this phenomenon is not available. It seems clear that deviations between experimental and theoretical enthalpies and entropies in part stem from coexistence of these two types of structures in real systems at finite temperatures.

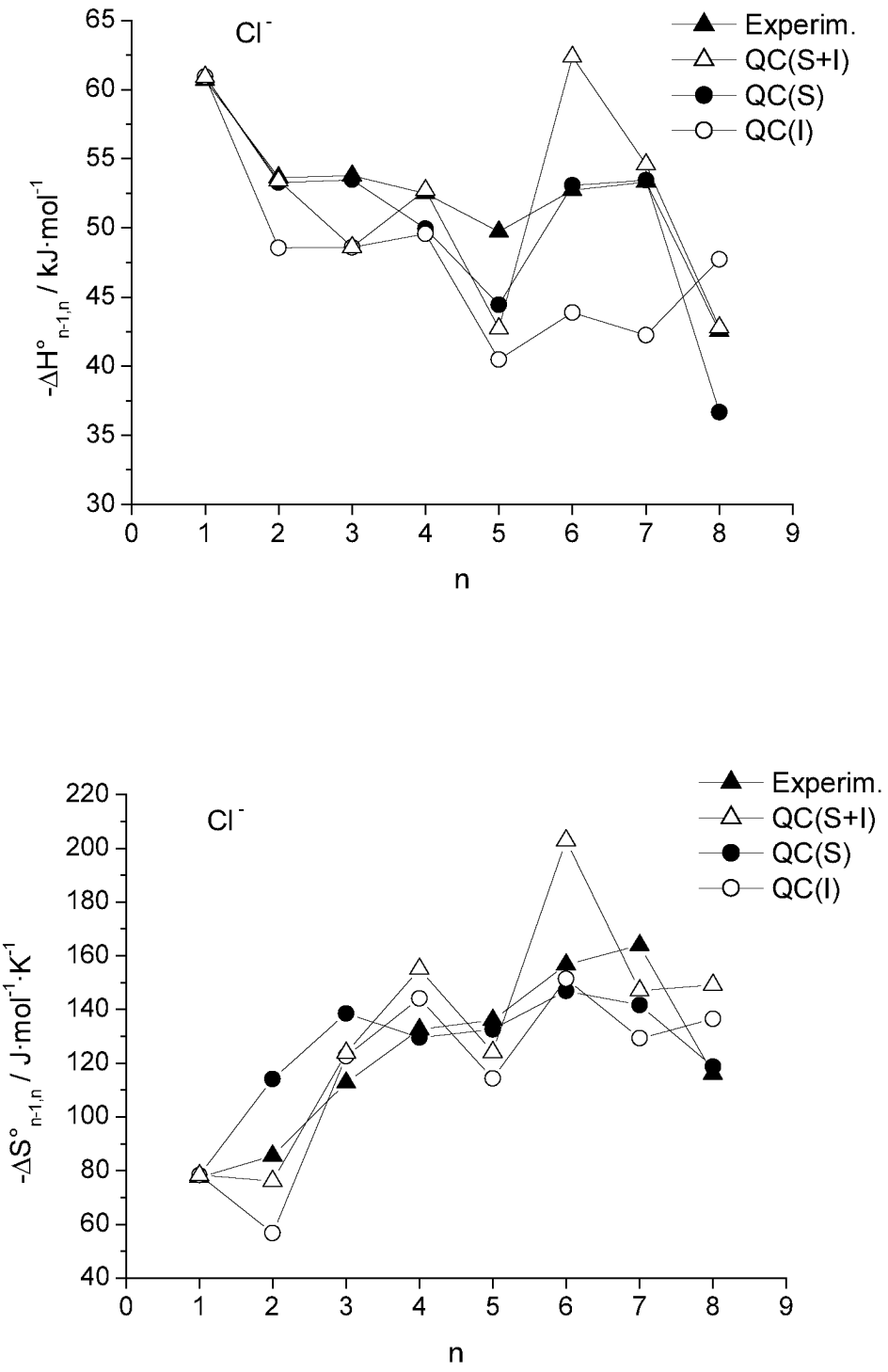

Figure 5.6. Comparison of theoretical and experimental thermochemical data for Cl^- hydration. QC(S) and QC(I) denote values for surface and interior clusters, respectively. QC(S+I) denotes values for the model system consisting of both structures.

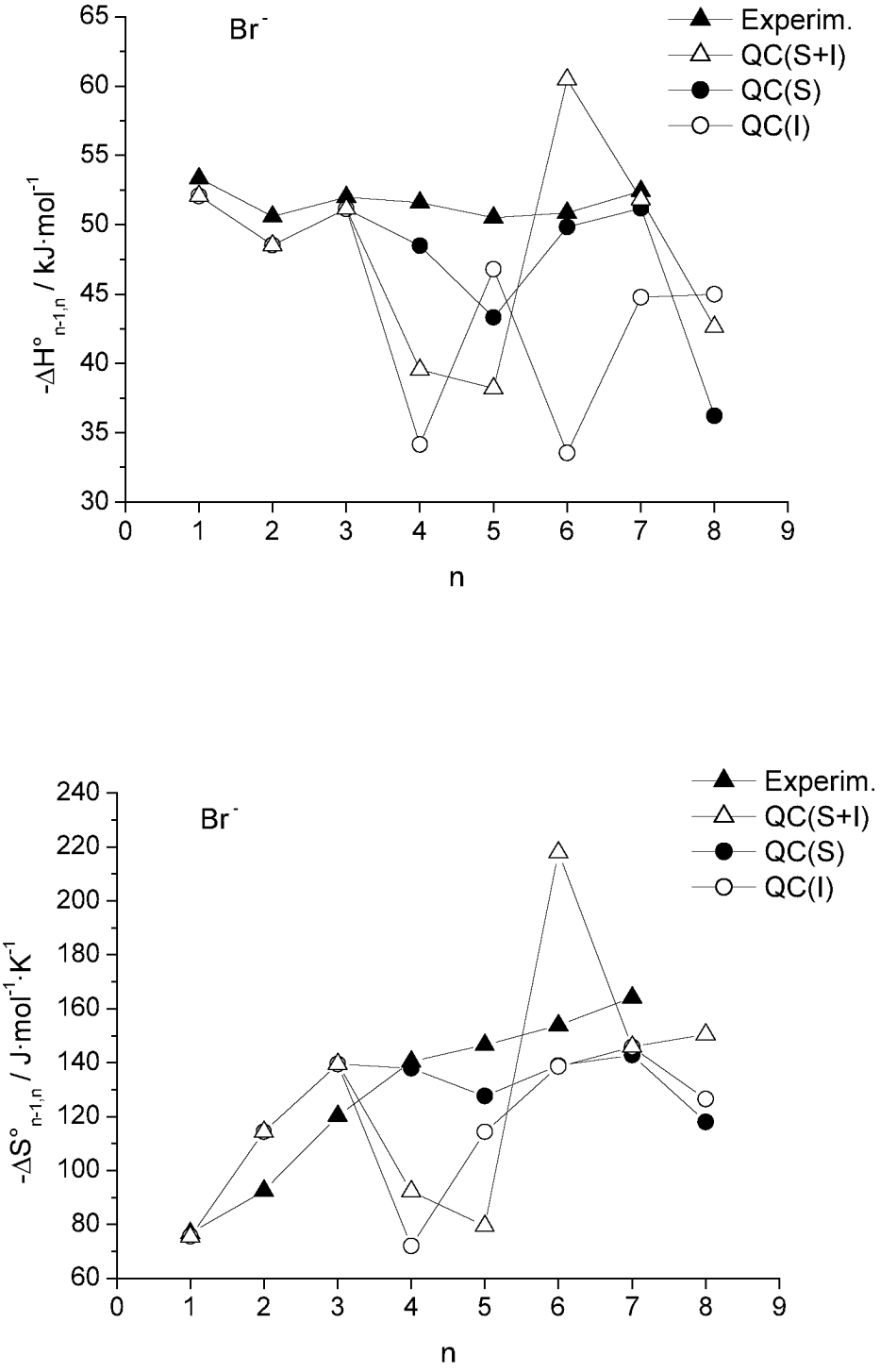

Figure 5.7. Comparison of theoretical and experimental thermochemical data for Br^- hydration. QC(S) and QC(I) denote values for surface and interior clusters, respectively. QC(S+I) denotes values for the model system consisting of both structures.

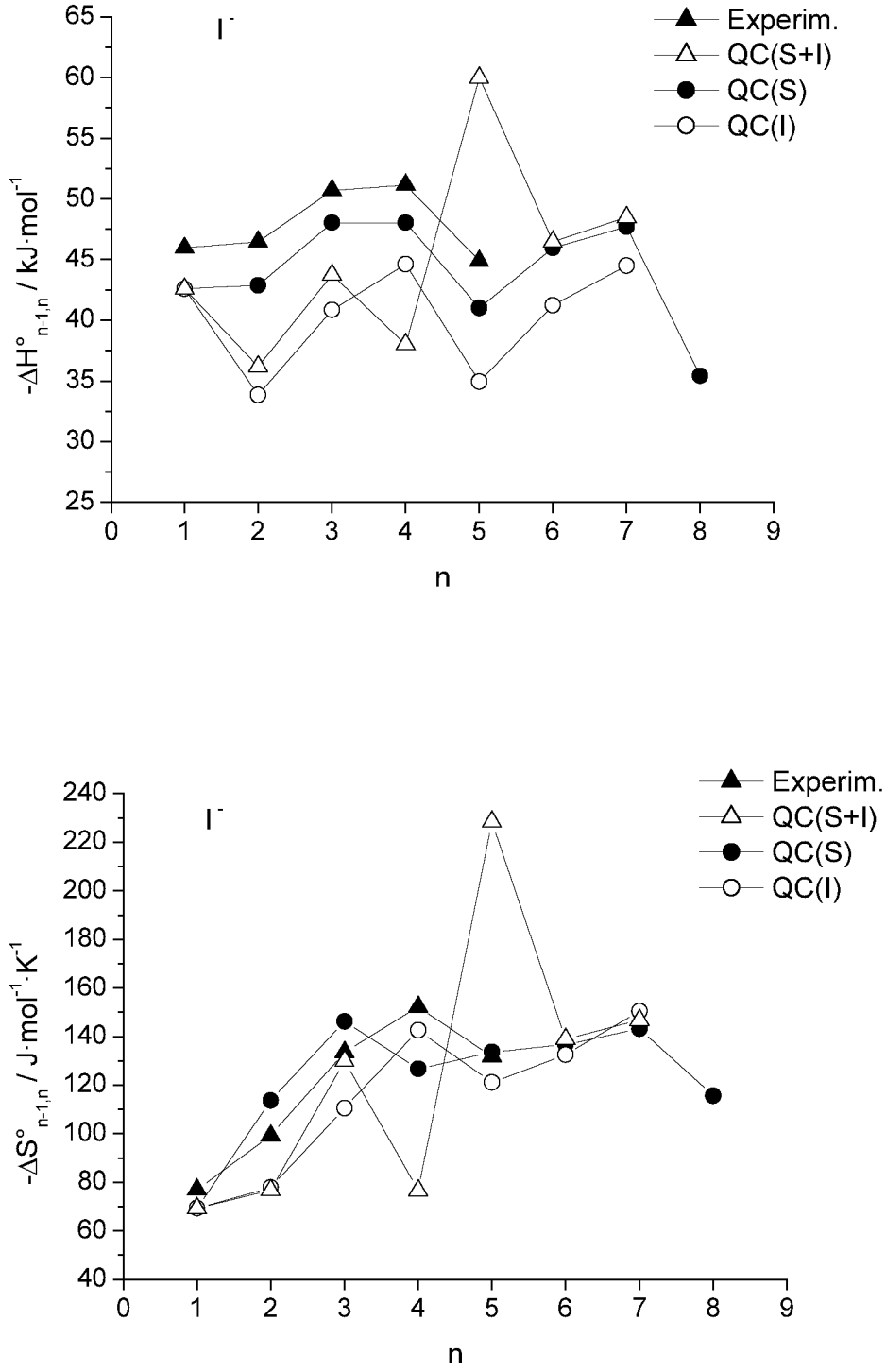

Figure 5.8. Comparison of theoretical and experimental thermochemical data for I^- hydration. QC(S) and QC(I) denote values for surface and interior clusters, respectively. QC(S+I) denotes values for the model system consisting of both structures.

Trends in stepwise thermochemistry of halide hydration

Stepwise hydration reactions are exothermic due to the stabilizing effect of the formation of hydrogen bonds during attachment of each new water molecule. The trends in stepwise enthalpies of hydration can be interpreted through consideration of the number of new hydrogen bonds formed at each step. There are two additional factors that affect the stepwise trends. One factor is that the strength of a hydrogen bond between an anion and water molecule decreases with increasing ionic radius from Cl^- to I^-, due to an increasing electron density around the anion leading to a more diffuse electrostatic bond. The equation for the interaction energy of an ion and a dipole indicates a rapid decrease in the mutual potential energy with the distance, r, that corresponds to ionic radius in this case:

$$V(r) = \frac{-(\varepsilon - 1)e^2}{8\pi n r^4} \tag{5.5}$$

where n is the number density, ε is the dielectric constant, and e is the charge of the ion.

Another factor governing the stepwise hydration enthalpies is that attachment of a new water molecule to a small cluster decreases the strength of the anion-water hydrogen bonds due to the increasing electron density surrounding the anion, although overall it has a stabilizing effect. This is true for direct bonding to the anion as is the case for surface bonding when directly bound water molecules are forced closer to the anion. The decrease in the strength of the anion-water hydrogen bonds is smaller for surface bonding when the new water molecule forms hydrogen bonds only with other water molecules because there are more possibilities to redistribute the electron density among the water molecules in this case. In going from n=0 to n=8 the numbers of new hydrogen bonds formed for surface clusters are given by the following sequence: 1,2,3,2,0,3,1,1. Experimental stepwise trends in enthalpy for iodide shown in Figure 5.8 are identical to the trends from the DFT calculations and can be quite well explained through the above sequence of additional hydrogen bonds. Because the hydrogen bonds are formed not only between the iodide and water molecules, but also among the water molecules themselves, it may be concluded that ion-solvent and solvent-solvent interaction in iodide water clusters are approximately equal in magnitude. The situation is different for chloride and bromide since they have smaller ionic radii and, consequently, stronger ion-solvent interactions. Addition of new water molecules weakens the direct ion-solvent interaction and the magnitude of the enthalpy change for stepwise hydration gradually decreases with cluster size. The changes in stepwise ΔH with cluster size for Cl^- and Br^- exhibit similar trends, but are smaller for Br^- than for Cl^-. This effect is due again to an increasing ionic radius. The two competing

factors in stepwise enthalpy trends are the number of new hydrogen bonds formed at each step and the weakening effect of the addition of a water molecule on the anion-water hydrogen bonds. The combination of these factors leads to the observed non-monotonic dependence of thermochemical values on the cluster size. As suggested in ref. [38], the increase in negative stepwise entropies reflects the increasing restriction in freedom of water molecules as they form more complex hydrogen bond networks with the increasing cluster size. A very stable structure is formed at n=7. At this step only one new hydrogen bond is formed as opposed to the three new bonds formed at n=6. However, the magnitude of the enthalpy change at n=7 is higher than for the previous step. This extra stabilization is due to the formation of the cage-like structure with only 3 water molecules directly bound to the anion. On the other hand, there are 4 water molecules bound to the anion at n=6. The increased electron density around the anion partially cancels the stabilizing effect of formation of the 3 new bonds at this step. A sharp decrease in the magnitude of the enthalpy change at n=8, where one new bond is formed similar to n=7, is caused by the new water molecule attaching on the outside of the cage-like structure and pushing the directly bound water molecules towards the anion, as can be seen from Figure 5.2. The decreased stability is also inferred from a sharp decrease in the magnitude of the entropy change compared to the previous step, which implies that water molecules lost less freedom in forming this cluster. As enthalpy characterizes ion-solvent and solvent-solvent interactions, the stepwise enthalpy plots for different halides are displaced, as can be seen in Figure 4.13. Entropy, however, characterizes the structures of clusters and since all halide clusters of same size have similar structures, the stepwise entropy plots in Figure 4.13 are much more similar.

The magnitudes of enthalpy change for interior clusters are almost always smaller than those for surface clusters. Up to n=3, the number of new hydrogen bonds formed at each step is higher for surface compared to interior structures. After n=3, however, this situation is reversed with very few exceptions. Interior structures have more anion-water bonds than surface structures and addition of a new water molecule at each step has a smaller stabilizing effect for interior clusters since it reduces the strength of anion-water hydrogen bonds.

5.4 Conclusions

Results of the DFT calculations for the structures of halide water clusters and the thermochemistry of hydration reactions have been reported. These calculations were carried out to enhance our experimental investigations of the same reactions. Two types of cluster geometries are possible for anionic water clusters – surface and interior. Surface clusters are

always more stable in terms of total energy for the clusters investigated here. Interior clusters have higher densities of vibrational states and in a simple model system consisting of one surface and one interior isomer, the population of interior states prevails at high temperatures. However, theoretical stepwise enthalpies and entropies for surface clusters are in significantly better agreement with the present experimental results. It is suggested that surface structures are preferred over interior ones due to the larger number of possible isomers. Interior structures are expected to be present in an unknown fraction. Enthalpies and entropies of stepwise hydration exhibit non-monotonic changes with the cluster size for small clusters. The stepwise trends are well explained through the number of additional hydrogen bonds formed at each hydration step and simultaneous weakening of ion-solvent interaction with increasing cluster size. For Cl^- the ion-solvent interaction is stronger than the solvent-solvent interaction due to the small ionic radius. The difference between the two types of interaction decreases for Br^-. For I^-, the ion-solvent and solvent-solvent interactions are of nearly the same magnitude. Finally, the fraction of clusters with energies above the dissociation threshold was calculated as a function of temperature. These calculations were used to check the cluster stability for a given set of experimental conditions.

Chapter 6. Protonated Water Clusters

6.1 Introduction

The stepwise solvation reaction of a proton by water molecules (6.1) has been the subject of considerable research effort in the past 30 years due to its occurrence in many natural processes and its importance as a fundamental chemical reaction.

$$H^+(H_2O)_{n-1} + H_2O = H^+(H_2O)_n \quad (6.1)$$

This reaction is important in describing ion chemistry in the ionosphere [62, 63] and electrical phenomena in the atmosphere [64, 65]. Past results of experimental investigations are summarized in refs. [36] and [66]. The HPMS technique allows the study of ion-molecule reactions under equilibrium conditions and can provide reliable thermochemical data. Kebarle and coworkers have been the primary investigators of reaction (6.1) by HPMS [42, 67, 68].

Results of experimental investigations of halide hydration using our newly constructed HPMS apparatus described in Chapter 4 suggested that inaccuracies in temperature measurement were possible major sources of error with earlier designs of the HPMS ion source. It was decided to examine clustering equilibria of a proton with water using this new ion source. Density functional calculations were carried out to aid in the choice of the best experimental conditions and assist in the interpretation of the experimental results.

6.2 Experimental and computational methods

Experiments were carried out using our new high-pressure mass spectrometer that was described in detail in Chapter 2. Techniques of sample preparation and measurement were also described in detail in Chapter 4. Briefly, the samples were prepared by injection of distilled water into a heated bulb filled with methane using a calibrated Hamilton microliter syringe. Ionizing electron pulse widths of 5-70μs and electron gun filament currents of 4-5A were used. The time between electron pulses was kept in the range 0.5-2ms. This time was normally chosen to be 20% longer than the overall lifetime of the ions in the ion source as determined by the decrease to zero intensity of measured ionic abundances. Tests were made using longer time periods that yielded identical ionic abundance ratios. On average, between 100 and 300 thousand pulses were necessary to collect reasonable ionic profiles. For this system, the ion signal in pulsing mode was weak due to rapid diffusion of the produced ions to the source

walls. It was concluded that a bigger internal ion source volume would be advantageous for proton hydration experiments. The measurements were taken over a temperature range from +540°C to -22°C. At this low temperature ion abundances became non-measurable. At 580°C, considerable spontaneous ionization was observed even when the electron gun and all ionization gauges were turned off. Partial water pressures of 0.04-0.3 mbar were used. The ion source pressure was kept in the range 1.5-6 mbar, where lower pressures were used at lower temperatures. These pressures were chosen to keep the gas number density in the ion source constant throughout the experimental temperature range. In an effort to ensure that equilibrium was indeed established, equilibrium constants were measured as a function of water partial pressure and overall ion source pressure. Reactions (6.1) were measured for n=2-7. Measurement of the first hydration step would require extremely high temperatures, as the calculated enthalpy change for this step is 710 kJ·mol^{-1}. Consequently, experimentally measured equilibria were those involving hydration of hydronium ion. We refer here to proton hydration since our quantum calculations also include the first hydration step.

Full geometry optimizations for $H^+(H_2O)_n$ clusters (n=1-8) were performed with the B3LYP DFT method and 6-311G** basis set using the GAUSSIAN98 [51] software package. Subsequent frequency calculations performed using the same level of theory were used to verify that an optimized structure was a minimum on the potential energy surface and for calculation of thermochemical data at different temperatures. All frequencies were scaled using a common factor of 0.89. Use of a scaling factor of 1.0 does not significantly change calculated enthalpies and entropies for stepwise hydration reactions. Typical changes for enthalpy and entropy are only 0.8 kJ·mol^{-1} and 2 J·mol^{-1}·K^{-1}, whereas typical experimental uncertainties are 2 kJ·mol^{-1} and 4 J·mol^{-1}·K^{-1}, respectively. Vibrational frequencies were used for calculation of the fraction of clusters with energies exceeding the dissociation threshold. A detailed description of this procedure was given in Chapter 5.

6.3 Results and discussion

Experimental results

Typical raw experimental and normalized ionic profiles for protonated water clusters are shown in Figure 6.1. Establishment of equilibrium was always extremely fast. As can be seen in Figure 6.1, equilibrium was established approximately 75μs after the electron pulse. Experimental results are presented as van't Hoff plots in Figure 6.2. Tables 6.1 and 6.2 list the

stepwise enthalpies and entropies calculated from the van't Hoff plots using the equations given in Chapter 4. Errors due to mass discrimination, as described in Chapter 3, were small compared with experimental errors and the corresponding corrections were not included here.

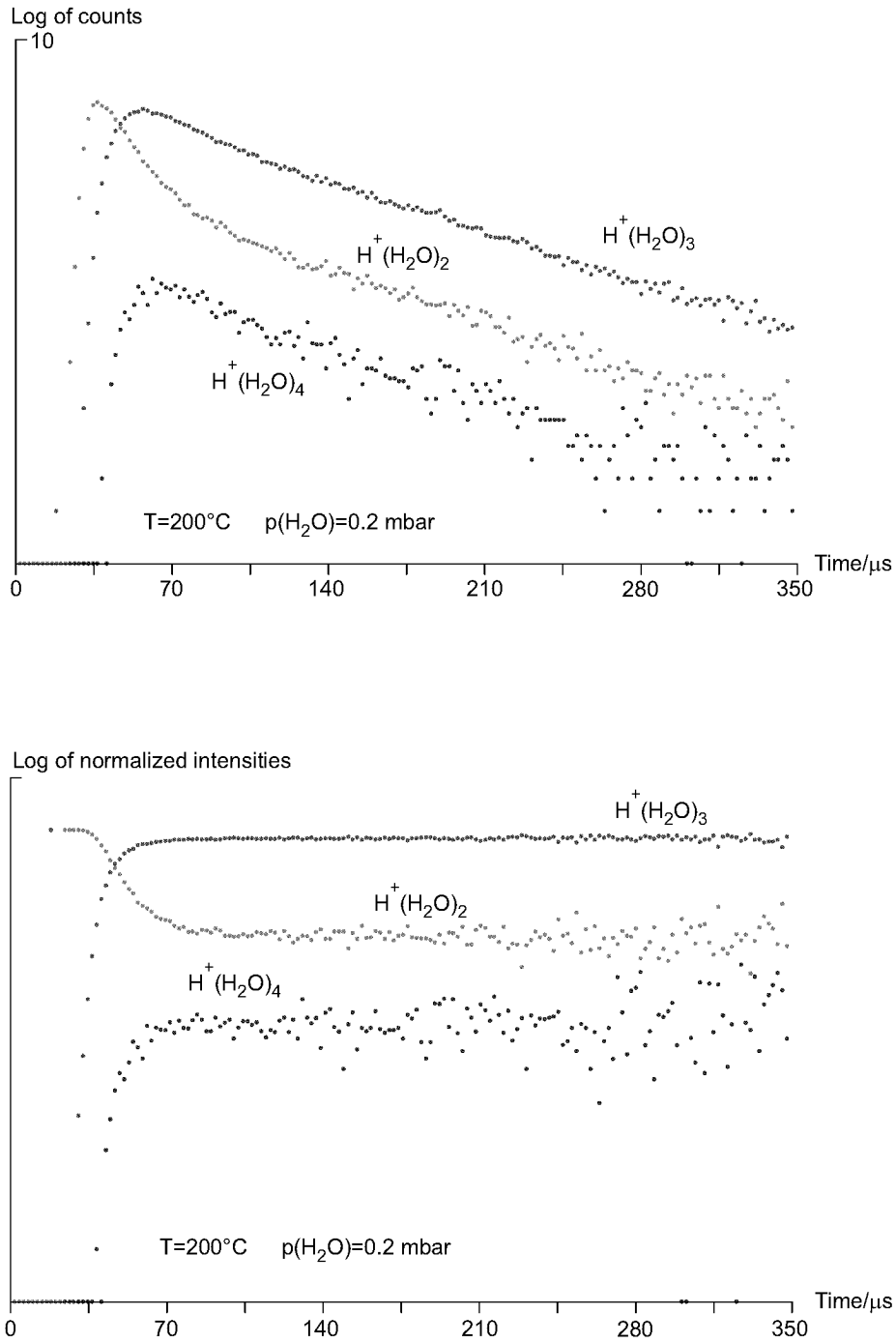

Figure 6.1. Raw and normalized profiles for protonated water clusters.

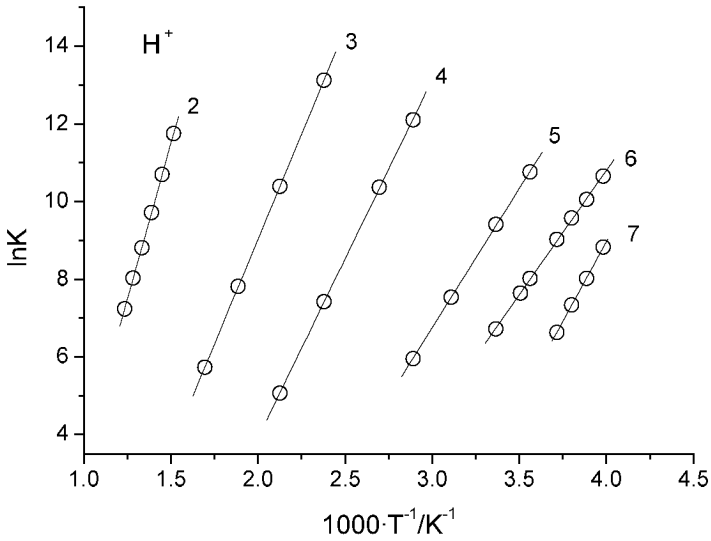

Figure 6.2. Experimental van't Hoff plots for proton hydration reactions.

n	Experimental	DFT
1	—	710.6
2	133.7±1.7	165.3
3	89.9±1.3	105.8
4	76.6±1.7	87.9
5	59.6±1.7	65.4
6	53.2±1.7	60.0
7	68.2±2.5	73.8
8	—	43.8

Table 6.1. Experimental and calculated values for $-\Delta H°_{n-1,n}$ [kJ·mol^{-1}] for proton hydration reactions (6.1). Standard pressure is 1000 mbar.

n	Experimental	DFT
1	—	14.3
2	105.0±5.0	108.9
3	104.7±4.2	92.5
4	120.7±4.2	112.3
5	122.7±4.2	109.4
6	123.1±5.0	101.0
7	198.3±5.0	196.1
8	—	52.4

Table 6.2. Experimental and calculated values for $-\Delta S°_{n-1,n}$ [J·mol^{-1}·K^{-1}] for proton hydration reactions (6.1). Standard pressure is 1000 mbar.

Results of DFT calculations

Optimized geometries are shown in Figure 6.3. Clusters with $n>1$ are formed around a very stable hydronium ion in which a proton forms a covalent bond with the water molecule. Because of the non-spherical central ion, protonated water clusters lack spherical symmetry, in contrast with water clusters of metal ions. The three hydrogen atoms of hydronium ion form hydrogen bonds with water molecules yielding loosely bound structures. Structures shown in Figure 6.3 were found to be the most stable isomers, although, there exists an increasing number of other stable isomers with increasing cluster size. Enthalpies and entropies calculated from the DFT results and averaged over corresponding experimental temperature ranges are given in Tables 6.1 and 6.2 along with experimental values.

Following the procedure given in Chapter 5, fractions of clusters with energies exceeding the dissociation threshold energy were calculated as a function of temperature and are shown in Figure 6.4. These results were used in the choice of the best temperature ranges where no significant fraction of observed clusters would dissociate during mass analysis.

Discussion

Comparison of the results from theoretical calculations and experimental thermochemical data for studied reactions is given in Figure 6.5. Overall agreement between the present and earlier experimental data is good, except for the last (6,7) hydration step. An analysis of the excited fractions within the experimental ranges used in ref. [68] shows that beginning with n=5, experiments in ref. [68] were done under conditions where excited fractions were larger than 5%. The effect of unimolecular dissociation on the results of HPMS measurements was discussed in detail in ref. [43]. If clusters of size n have larger excited fraction than clusters of size $n-1$, the observed stepwise enthalpy change will have a larger magnitude than the true value. This is also the case for the (4,5) step from ref. [68]. The magnitude of the enthalpy change for the (5,6) step from ref. [68] is only a slightly larger than in the present study. This may be due in part to compensation of unimolecular dissociation errors by errors in temperature measurement that was discussed in Chapter 4. Analysis of the excited fraction for ions involved in the (6,7) step shows that clusters with n=7 have a smaller excited fraction than clusters with n=6 within the temperature range used in ref. [68].

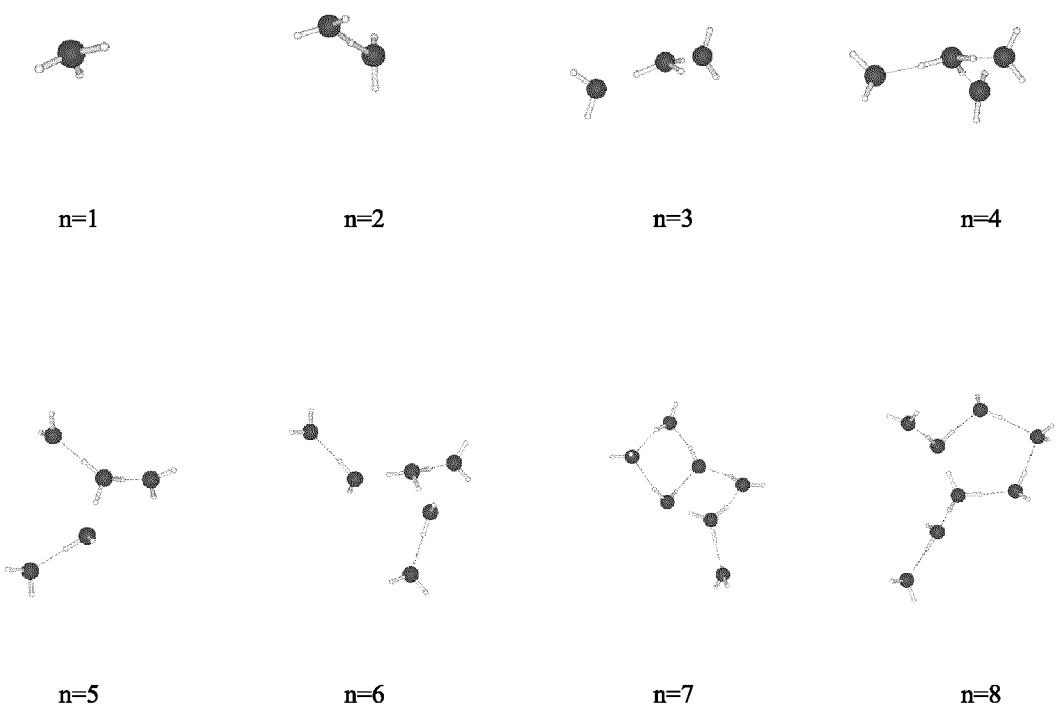

Figure 6.3. Optimized geometries for protonated water clusters.

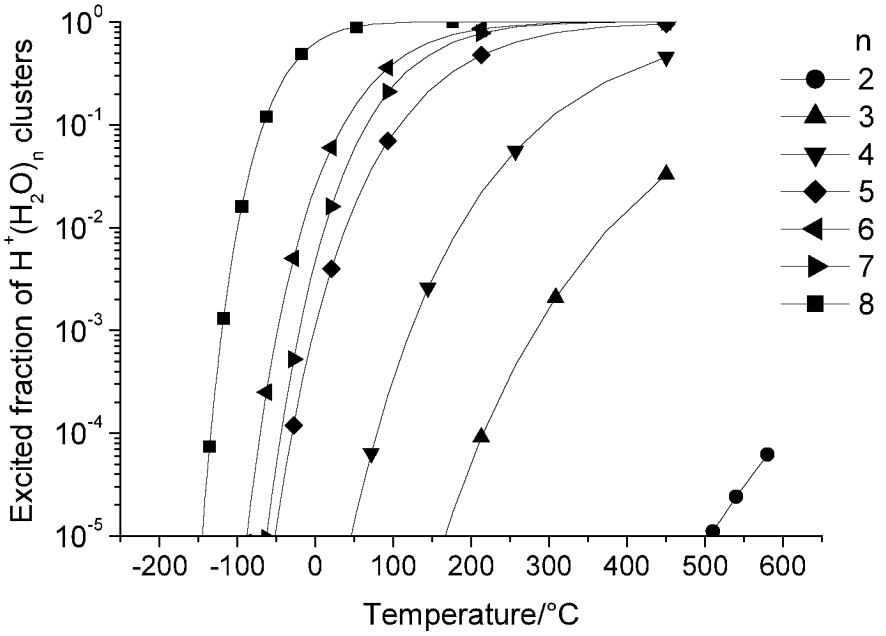

Figure 6.4. Fraction of protonated water clusters with energies exceeding the dissociation threshold.

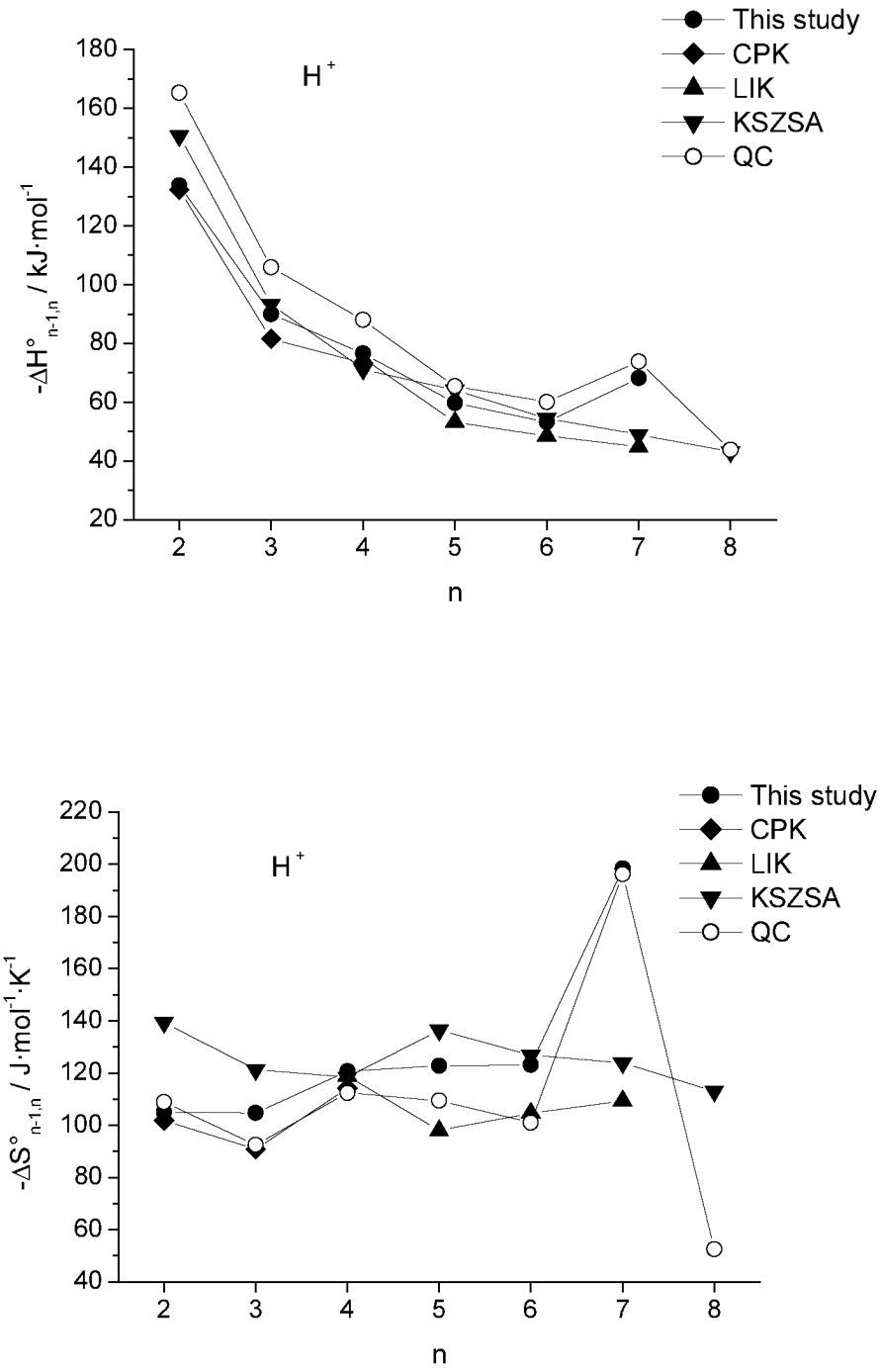

Figure 6.5. Comparison of enthalpy and entropy changes for proton hydration reactions obtained in this work with previous data by Kebarle and coworkers and DFT calculations. CPK – data from ref. [67], LIK – data from ref. [42], KSZSA – data from ref. [68], QC – our DFT calculations.

It follows that unimolecular dissociation for the (6,7) step within the given temperature range would lead only to a slight decrease in the magnitude of the enthalpy change. It appears that the large discrepancy between the enthalpy change for the (6,7) step from ref. [68] and our experimental and theoretical values stems from temperature uncertainties. The measurement of the (7,8) hydration step in ref. [68] was done over a temperature range where the excited fraction for n=8 is very large. The dependence of the excited fraction on temperature, however, is weak within this experimental temperature range. The net effect of unimolecular dissociation would be to shift the van't Hoff plot downward leading to a change only in the entropy. Indeed, the enthalpy change for the (7,8) step from ref. [68] agrees well with the DFT results, however, the magnitude of the entropy change is almost twice that predicted by the calculations.

Measurements in ref. [42] were done under conditions where no significant unimolecular dissociation was present. However, the lowest temperature in their experiments was -60°C, where water vapor could begin to condense on the ion source walls. We observed condensation at -45°C in our experimental study of halides, as did Hiraoka *et al.* [39]. The ice vapor pressure is 0.130 mbar at -40°C, 0.039 mbar at -50°C and only 0.011 mbar at -60°C [69]. If water condenses in the ion source then the real partial pressure of water is lower than expected and calculated equilibrium constants would be smaller. Since this effect would become more pronounced at lower temperatures, the van't Hoff plots would be less steep, leading to smaller magnitudes for the calculated enthalpy change. This might be an explanation for the large discrepancy between ref. [42] and our data for the (6,7) step and for smaller discrepancies for the preceding two hydration steps, since the corresponding van't Hoff plots from ref. [42] also extend into the lower temperature region for these reactions.

While our experimental enthalpies are systematically smaller in absolute value than the DFT results, they follow the same stepwise trends. These trends can be interpreted through the number of stabilizing hydrogen bonds formed at each step. As can be seen in Figure 6.3, the first solvation shell closes when n=4. The overall decrease in the absolute value of the enthalpy changes with increasing cluster size is due to the weakening of proton-water or hydronium-water hydrogen bonds when a new water molecule is introduced. For reactions with n=2 to n=6, one additional hydrogen bond is formed for each step and an overall decrease in the absolute value of the enthalpy change is accordingly observed. The break in slope in Figure 6.5 at n=4 corresponds to extra stabilization due to closure of the first shell. In the (6,7) hydration step there are not one, but three additional hydrogen bonds formed and instead of an expected decrease of about 6 kJ·mol^{-1}, the absolute value of the enthalpy change increases by 15 kJ·mol^{-1},

thus giving a total gain of 21 $kJ \cdot mol^{-1}$ or 10.5 $kJ \cdot mol^{-1}$ per hydrogen bond. An identical value of 10.5 $kJ \cdot mol^{-1}$ for the hydrogen bond in $Cl_3C–H\cdots OC(CH_3)_2$ in the liquid phase was reported in ref. [70], although a value of 16.7 $kJ \cdot mol^{-1}$ was reported for the hydrogen bond in $Cl_3C–H\cdots N(C_2H_5)_3$ in the liquid phase. The increased stability and ordering of molecules for the mesh-like structure at n=7 is more obvious when the entropy change is considered as it is almost twice that of the previous step. No new hydrogen bonds are formed in the (7,8) step. However, the rearrangement of the mesh-like structure observed at n=7 into a ring formed by 5 water molecules at n=8 adds some stabilization so that the decrease in enthalpy is not as sharp as might be expected. The stepwise enthalpy trends clearly demonstrate the competition between the weakening effect of adding a water molecule on the new and existing hydrogen bonds and the stabilizing effect of the formation of new hydrogen bonds.

Chapter 7. Conclusions

The construction details of a new high-pressure mass spectrometer featuring a novel ion source have been presented. The new ion source design is based on successful designs of high temperature calorimeters with special care taken to ensure minimal temperature gradients and excellent overall temperature stability. The most important feature of the new ion source is the accurate measurement of temperature of gas directly in the reaction chamber using a platinum resistance thermometer inset into the main source volume. Prior to installation in the ion source, the PRT was calibrated against a NIST traceable secondary standard temperature reference. The estimated accuracy of the PRT temperature is better than 0.05K. Use of higher acceleration voltages of 4kV, additional ion optics, and the mass spectrometer data system led to an increased sensitivity of the present HPMS apparatus. Results of experiments conducted on this mass spectrometer strongly suggest that this new design featuring improved accuracy of temperature measurement and an increase in the mass spectrometer sensitivity improves the overall accuracy of the HPMS technique. It was found that many further improvements could be made to the current ion source design. These include: direct measurement of the pressure inside the ion source; ion source temperature control should be of true DC current proportional type to exclude AC current effects of the heater current on electron gun focusing; the ion exit slit design should be improved such as to have a non-obstructed ion exit region to reduce CID; gas flow through the source should be increased compared with outflow through the slits to minimize enrichment of heavier components in the ion source due to mass discrimination effects.

The physical conditions and behavior of ions in a typical HPMS ion source have been examined theoretically. It has been shown that the HPMS feature of having molecular flow from the ion source leads to a mass discrimination affecting not only neutral molecules as thought previously, but all ions exiting the ion source. It was shown that experimental HPMS results corrected for mass discrimination are in better agreement with results from non-mass discriminating techniques. It is believed that results from HPMS measurements should be consistently corrected for mass discrimination dependent on the nature of gas outflow from the ion source.

Stepwise hydration reactions involving Cl^-, Br^-, and I^- have been investigated using this high-pressure mass spectrometer. Thermodynamic properties for cluster ions of larger size than have previously been examined were determined. The highest hydration steps measured

experimentally were n=8 for Cl^-, n=7 for Br^-, and n=5 for I^-. Quantum mechanical calculations using density-functional theory (DFT) have been carried out for these systems. In contrast with earlier experimental measurements, these quantum and experimental thermochemical quantities for halide water clusters exhibit a non-monotonic dependence of stepwise enthalpies and entropies of hydration on cluster size. Analysis of errors in the HPMS experiment has suggested that earlier designs of HPMS ion sources could have suffered from errors in temperature measurements leading to large errors in determined enthalpy and entropy changes.

Vibrational frequencies obtained from the quantum mechanical calculations were used for calculation of the fraction of clusters having energies exceeding the energy required for dissociation. These results were used in the choice of best experimental conditions where the fraction of clusters undergoing unimolecular dissociation would be minimized. Excited fraction data were used to correct experimentally observed ionic ratios to yield thermodynamic values for one specific reaction step for a highly solvated anion.

Two distinct structure types are possible for the halide water clusters, those of interior and surface. According to DFT calculations, surface clusters are more stable for all of the temperatures investigated. Interior clusters, however, have a higher density of vibrational states and in a simple model system consisting of one interior and one surface type isomer, the population of interior states prevails at higher temperatures. Nevertheless, stepwise enthalpies and entropies of hydration for surface clusters agree much better with the present experimental results. It is suggested that in natural systems of these types of halides, surface clusters prevail due to larger number of isomers of surface type, yet the interior structures should also be present in small amounts at elevated temperatures.

The stepwise hydration of the proton has been studied both experimentally using our high-pressure mass spectrometer and theoretically using density-functional theory. Protonated water clusters with water molecules ranging from 1 to 7 have been experimentally observed and examined. Clusters with up to 8 water molecules have been investigated theoretically. Comparison of these new results with previous experimental data revealed discrepancies believed to stem from inaccuracies in temperature measurement with earlier HPMS ion sources and, on some occasions, from inappropriate experimental conditions.

There is excellent agreement between the experimental and theoretical trends for stepwise enthalpies and entropies of hydration for all halide and proton water clusters. Both experimental and theoretically determined thermodynamic quantities exhibit the same non-monotonic behavior with increasing cluster size. The stepwise trends are interpreted in terms of

the number of additional hydrogen bonds formed at each hydration step and the weakening effect of an increasing cluster size on ion-solvent interactions. The competition between these two effects leads to the observed non-monotonic behavior. Ion-solvent interactions become weaker with an increasing ionic radius. Analysis of the experimental data suggests that the ion-solvent interactions are stronger than solvent-solvent interactions for chloride, but become similar for larger ions such as bromide and nearly equal for iodide.

Gas-phase differential integrated enthalpies of solvation for halide water clusters calculated from these experimental results approach bulk solvation values with increasing cluster size. It is clear that small clusters with 7-8 water molecules are still quite far from bulk solvation as expected, but these non-monotonic effects show difficulties in the modeling of the first and second solvation shells. Even though HPMS provides accurate thermochemical data, it is limited in the largest size of clusters that can be studied, typically a maximum cluster having about 10 ligands. The electrospray ionization technique allows production of much larger clusters. Large clusters undergo unimolecular dissociation under typical experimental conditions and for electrospray ionization to achieve the accuracy of the HPMS technique, an accurate method to quantitatively account for unimolecular dissociation must be incorporated.

In conclusion, improved accuracy of new experimental data measured with a newly constructed high-pressure mass spectrometer has led to excellent agreement with DFT calculations for selected systems. These have been the first HPMS data accurate enough to reproduce the non-monotonic trends predicted by quantum mechanical calculations, inherently related to the nature of bonding in the halide water clusters. Since a rigorous test in the evaluation of validity of quantum mechanical calculations is the comparison with experiment, the present agreement lends strong support to the validity of DFT calculations when used as a tool for obtaining structural and thermodynamic information for cluster ions where experimental results are lacking.

References

1. Tanger IV, J.C. and Pitzer, K.S., J. Phys. Chem., 1989, **93**: p. 4941.
2. Pitzer, K.S., J. Phys. Chem., 1983, **87**: p. 1120.
3. Pitzer, K.S., J. Phys. Chem., 1982, **86**: p. 4704.
4. Cramer, C.J. and Truhlar, D.G., *Continuum Solvation Models*, in *Solvent Effects and Chemical Reactivity*, Tapia, O. and Bertrán, J., Editors. 1996, Kluwer: Dordrecht. p. 1.
5. Durden, D.A., Kebarle, P., and Good, A., J. Chem. Phys., 1969, **50**: p. 302.
6. Kebarle, P., *Techniques for the Study of Ion-Molecule Reactions*, ed. Farrar, J.M. and Saunders Jr., W. 1988, Wiley: New York.
7. Hiraoka, K., Morise, K., Nishijima, T., Nakamura, S., Nakazato, M., and Ohkuma, K., Int. J. Mass Spectrom. and Ion Proc., 1986, **68**: p. 99.
8. Szulejko, J.E., Fisher, J.J., McMahon, T.B., and Wronka, J., Int. J. Mass Spectrom. and Ion Proc., 1988, **83**: p. 147.
9. Hiraoka, K. and Kebarle, P., J. Am. Chem. Soc., 1975, **97**: p. 4179.
10. Szulejko, J.E., Hop, C.E.C.A., McMahon, T.B., Harrison, A.G., Young, A.B., and Stone, J.A., J. Am. Soc. Mass. Spectrom., 1992, **3**: p. 33.
11. Chen, X., Oscarson, L., Cao, H., Gillespie, S.E., and Izatt, R.M., Thermochim. Acta, 1996, **285**: p. 11.
12. Mangum, B.W. and Furukawa, G.T., *Guidelines for realizing the ITS-90, NIST Technical Note 1265*. 1990, National Institute of Standards.
13. Franklin, J.L., *Kinetics and Dynamics*. 1978, Dowden, Hutchinson & Ross: Stroudsburg.
14. Bowers, M.T., Aue, D.H., Webb, H.M., and McIver, R.T., J. Am. Chem. Soc., 1971, **93**: p. 4314.
15. McGrew, D.S., Knighton, W.B., Bognar, J.A., and Grimsrud, E.P., Int. J. Mass Spectrom. and Ion Proc., 1994, **139**: p. 47.
16. Williamson, D.H., Knighton, W.B., and Grimsrud, E.P., Int. J. Mass Spectrom. Ion Processes, 1996, **154**: p. 15.
17. Zook, D.R. and Grimsrud, E.P., J. Phys. Chem, 1988, **92**: p. 6374.
18. Hiraoka, K., Morise, K., and Shoda, T., Int. J. Mass Spectrom. and Ion Proc., 1985, **67**: p. 11.
19. Massey, H.S.W., Burhop, E.H.S., and Gilbody, H.B., *Electronic and Ionic Impact Phenomena*. 2 ed. Vol. 1-4. 1971, Oxford: London.
20. O'Hanlon, J.F., *User's Guide to Vacuum Technology*. 1989, Wiley: New York.
21. Loeb, L.B., *The Kinetic Theory of Gases*. 1934, McGraw-Hill: New York.

22. McDaniel, E.W., *Collision Phenomena in Ionized Gases*. 1964, Wiley: New York. p. 489.
23. Lineberger, W.C. and Puckett, L.J., Phys. Rev., 1969, **186**: p. 116.
24. Massey, H.S.W., *Slow Collisions of Heavy Particles*, in *Electronic and Ionic Impact Phenomena*, Massey, H.S.W., Burhop, E.H.S., and Gilbody, H.B., Editors. 1971, Oxford: London. p. 1951.
25. Massey, H.S.W., *Recombination and Fast Collisions of Heavy Particles*, in *Electronic and Ionic Impact Phenomena*, Massey, H.S.W., Burhop, E.H.S., and Gilbody, H.B., Editors. 1974, Oxford: London. p. 2157.
26. Massey, H.S.W., *Slow Collisions of Heavy Particles*, in *Electronic and Ionic Impact Phenomena*, Massey, H.S.W., Burhop, E.H.S., and Gilbody, H.B., Editors. 1971, Oxford: London. p. 1302.
27. Puckett, L.J. and Teague, M.W., J. Chem. Phys., 1971, **54**: p. 2564.
28. Dushman, S., *Scientific Foundations of Vacuum Technique*. 1949, Wiley: New York. p. 38.
29. Loeb, L.B., *Fundamental Processes of Electrical Discharge in Gases*. 1939, Wiley: New York. p. 56.
30. Mason, E.A. and McDaniel, E.W., *Transport Properties of Ions in Gases*. 1988, Wiley: New York. p. 11.
31. Kebarle, P. and Hogg, A.M., J. Chem. Phys., 1965, **42**: p. 668.
32. Szulejko, J.E. and McMahon, T.B., J. Am. Chem. Soc., 1993, **115**: p. 7839.
33. Lias, S.G., Liebman, J.F., and Levin, R.D., J. Phys. Chem. Ref. Data, 1984, **13**: p. 695.
34. Wolf, J.F., Staley, R.H., Koppel, I., Taagepera, M., McIver Jr., R.T., Beauchamp, J.L., and Taft, R.W., J. Am. Chem. Soc., 1977, **99**: p. 5417.
35. Meot-Ner, M. and Sieck, W., J. Am. Chem. Soc., 1991, **113**: p. 4448.
36. Keesee, R.G. and Castleman Jr., A.W., J. Phys. Chem. Ref. Data, 1986, **15**.
37. Keesee, R.G. and Castleman Jr., A.W., Chem. Phys. Lett., 1980, **74**: p. 139.
38. Arshadi, M., Yamadagni, R., and Kebarle, P., J. Phys. Chem., 1970, **74**: p. 1475.
39. Hiraoka, K., Mizuse, S., and Yamabe, S., J. Am. Chem. Soc., 1988, **92**: p. 3943.
40. Good, A., Durden, D.A., and Kebarle, P., J. Chem. Phys., 1970, **52**: p. 212.
41. Hogg, A.M. and Kebarle, P., J. Chem. Phys., 1965, **43**: p. 449.
42. Lau, Y.K., Ikuta, S., and Kebarle, P., J. Am. Chem. Soc., 1982, **104**: p. 1462.
43. Sunner, J. and Kebarle, P., J. Phys. Chem., 1981, **85**: p. 327.
44. Wagman, D.D., Evans, W.H., Parker, V.B., Schumm, R.H., Halow, I., Bailey, S.M., Churney, K.L., and Nuttal, R.L., J. Phys. Chem. Ref. Data, 1982, **11, Suppl. No. 2**.
45. Archer, D.G. and Wang, P., J. Phys. Chem. Ref. Data, 1990, **19**: p. 371.
46. Hill, P.G., J. Phys. Chem. Ref. Data, 1990, **19**: p. 1233.
47. Combariza, J.E., Kestner, N.R., and Jortner, J., Chem. Phys. Lett., 1992, **203**: p. 423.
48. Combariza, J.E., Kestner, N.R., and Jortner, J., J. Chem. Phys., 1994, **100**: p. 2851.

49. Combariza, J.E., Kestner, N.R., and Jortner, J., Chem. Phys. Lett., 1994, **221**: p. 156.
50. Ayala, R., Martinez, J.M., Pappalardo, R.R., and Marcos, E.S., J. Phys. Chem., 2000, **104**: p. 2799.
51. Frisch, M.J., Trucks, G.W., Schlegel, H.B., Scuseria, G.E., Robb, M.A., Cheeseman, J.R., Zakrzewski, V.G., Montgomery, J.A., Stratmann, R.E., Burant, J.C., Dapprich, S., Millam, J.M., Daniels, A.D., Kudin, K.N., Strain, M.C., Farkas, O., Tomasi, J., Barone, V., Cossi, M., Cammi, R., Mennucci, B., Pomelli, C., Adamo, C., Clifford, S., Ochterski, J., Petersson, G.A., Ayala, P.Y., Cui, Q., Morokuma, K., Malick, D.K., Rabuck, A.D., Raghavachari, K., Foresman, J.B., Cioslowski, J., Ortiz, J.V., Stefanov, B.B., Liu, G., Liashenko, A., Piskorz, P., Komaromi, I., Gomperts, R., Martin, R.L., Fox, D.J., Keith, T., Al-Laham, M.A., Peng, C.Y., Nanayakkara, A., Gonzalez, C., Challacombe, M., Gill, P.M.W., Johnson, B., and Chen, W., *GAUSSIAN98 Revision A.6*, 1998, Gaussian Inc.: Pittsburgh, PA.
52. LaJohn, L.A., Christiansen, P.A., Ross, R.B., Atashroo, T., and Ermler, W.C., J. Chem. Phys., 1987, **87**: p. 2812.
53. Dang, L.X. and Smith, D.E., J. Chem. Phys., 1993, **99**: p. 6950.
54. Stein, S.E. and Rabinovitch, B.S., J. Chem. Phys., 1973, **58**: p. 2438.
55. Yeh, I., Perera, L., and Berkowitz, M.L., Chem. Phys. Lett., 1997, **264**: p. 31.
56. Perera, L. and Berkowitz, M.L., J. Chem. Phys., 1991, **95**: p. 1954.
57. Perera, L. and Berkowitz, M.L., J. Chem. Phys., 1993, **99**: p. 4222.
58. Perera, L. and Berkowitz, M.L., J. Chem. Phys., 1994, **100**: p. 3085.
59. Sremaniak, L.S., Perera, L., and Berkowitz, M.L., J. Chem. Phys., 1996, **100**: p. 1350.
60. Perera, L. and Berkowitz, M.L., J. Chem. Phys., 1993, **99**: p. 4236.
61. Asada, T., Nishimoto, K., and Kitaura, K., J. Phys. Chem, 1993, **97**: p. 7724.
62. Ferguson, E.E., J. Geophys. Rev. Space Phys., 1969, **74**: p. 2217.
63. Narcisi, R.S. and Bailey, A.D., J. Geophys. Rev., 1965, **70**: p. 3687.
64. Lindinger, W., Phys. Rev. A, 1973, **7**: p. 328.
65. Palmer, J.A., *Atmospheric Electricity*. 1967, Pergamon Press: New York.
66. Dalleska, N.F., Honma, K., and Armentrout, P.B., J. Am. Chem. Soc., 1993, **115**: p. 12125.
67. Cunningham, A.J., Payzant, J.D., and Kebarle, P., J. Am. Chem. Soc., 1972, **94**: p. 7627.
68. Kebarle, P., Searles, S.K., Zolla, A., Scarborough, J., and Arshadi, M., J. Am. Chem. Soc., 1967, **89**: p. 6393.
69. Lide, D.R., *CRC Handbook of Chemistry and Physics*. 76 ed. 1996, CRC Press: Boca Raton.
70. Huggins, C.M., Pimentel, G.C., and Shoolery, J.N., J. Phys. Chem, 1955, **23**: p. 1244.

Suppliers Internet addresses

Alltech	*www.alltechweb.com*
Cajon	*www.swagelok.com*
Chromalox	*www.chromalox.com*
Cole-Parmer	*www.coleparmer.com*
Dasylab	*www.datalog-kg.de*
Edwards	*www.boc.com/evt/*
Eurotherm	*www.eurotherm.com*
Galileo	*www.galileocorp.com*
Hamilton	*www.hamiltoncompany.com*
Hoke	*www.hoke.com*
Insultech	*www.insultech.ch*
Keithley	*www.keithley.com*
Kurt Lesker	*www.lesker.com*
Leybold	*www.leyboldvac.de*
Magnetic Shield Corp.	*www.magnetic-shield.com*
Micromass	*www.micromass.co.uk*
MicroSim	*www.orcad.com*
Minco	*www.minco.com*
Melles Griot	*www.mellesgriot.com*
MKS	*www.mksinst.com*
Omega	*www.omega.com*
Ontrak	*www.ontrak.net*
EG&G Ortec	*www.perkinelmer.com*
QVR Designs	*home.att.net/~qvr1.pete/*
SimIon	*www.sisweb.com*
Scimar	*www.scimar.co.uk*
Start Spellman	*www.start-spellman.co.uk*
Swagelok	*www.swagelok.com*
TTI	*www.tti-test.com*

Appendix A. Technical Documentation

A.1 Sample introduction system

The sample introduction system consisted of the gas-handling plant (GHP), syringe pump, carrier gas, mass flow controller, heated gas transfer lines, a 3-way switching valve, thin bore glass capillary, and a rotary pump. The overall layout of the system is shown in Figure A.1. The carrier gas was delivered to both the GHP and flow controller through a standard vacuum hose. The outlets of the GHP and flow controller were made of 1/4" stainless steel tubing and were connected to a Hoke SelectoMite 7165 stainless steel 3-way valve. In this configuration, flow from either the GHP or through the flow controller could be used. To control the flow from the gas-handling plant, a Hoke MilliMite 1300 stainless steel metering valve was mounted between the GHP and the 3-way valve. The section of the source inlet line located following the 3-way valve was constructed of 1/4" stainless steel tubing. This line was fitted with a septum port for direct liquid sample introduction using a syringe pump connected in series with the gas flow. The part of the inlet line located after the septum port was assembled using 2m of 9mm inside diameter coiled glass tube connected to a 60cm long, 4mm inside diameter glass tube which was then connected directly to the source. The outlet line was also constructed of 60cm and 2m glass tubes and was made symmetrical with the glass inlet line. The purpose of the glass tubes and their large length was to prevent electrical discharge in the gas from the source potential to ground. With this chosen length and for gas line pressures in the range 2-10 mbar, the glass tubes provided adequate protection up to 6kV. A corona discharge was occasionally observed in the glass lines adjacent to the source over a small length at low line pressures (0.5-2mbar and 6kV), although, it never extended beyond the ends of the glass lines. Two Swagelok Tees (PFA and teflon) were inserted in-line and opposite to the ion source ends of the 2m glass tubes and these were, in turn, connected to another Hoke SelectoMite 7165 stainless steel 3-way valve. The output port of this valve was connected to a 10 mbar MKS Baratron 628A absolute pressure transducer using 1/4" stainless steel tubing.

The inlet or outlet pressure could be monitored at points located equidistant with respect to the ion source. Following the teflon tee, the outlet gas line was made of PVC hose and was connected to a rotary pump through a 2cm long, 1mm inside diameter glass capillary used to

limit the conductance of the outlet line. As can be seen in Figure A.1, both inlet and outlet ion source gas lines had the ability to be pumped directly through the GHP.

All of the joints in the gas line were constructed using Swagelok or Gyrolok adapters with teflon ferrules. All valve and flow controller ports were also of the Swagelok or Gyrolok type. The teflon and PFA tee's and unions were bored through to minimize the surface area exposed to the gas flow. All components of the inlet and outlet lines, except for the PVC hose, were heated to 140°C with band heaters controlled by VG Micromass temperature controllers from the mass spectrometer and a Eurotherm 2132 temperature controller/Eurotherm TE10S solid state relay combination. The stainless steel line to the 10 mbar pressure transducer was heated to 70°C in a similar fashion using an additional VG Micromass temperature controller.

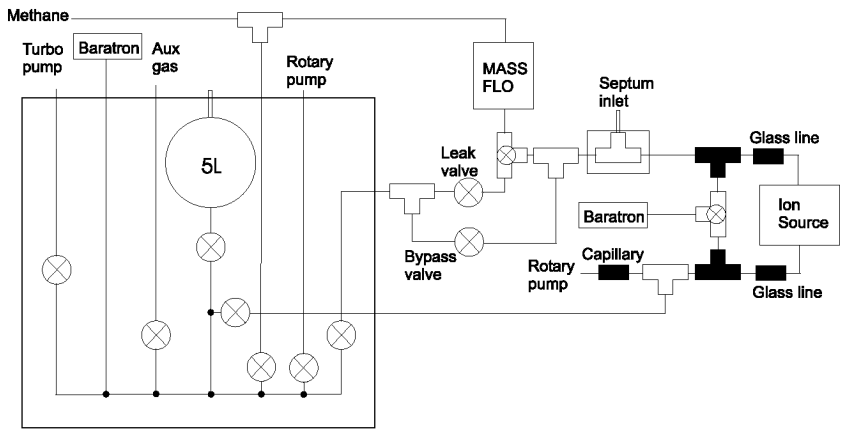

Figure A.1. Sample introduction system.

Syringe pump and mass flow controller

The gas-handling plant was normally used for all experimental mixtures. For some experiments, liquid compounds were introduced into the methane flow using a Cole-Parmer 74900 syringe pump connected through a high-temperature septum port mounted inside an insulated steel box. The temperature of the septum inlet port was kept constant at 100°C using a VG temperature controller. To reduce the conductance of the syringe-septum line and to prevent the solution from being drawn into the gas flow, a 6cm piece of 0.125mm i.d. Peek tubing was used to connect the syringe pump and septum port. The carrier gas flow was controlled and measured by an MKS 1679A Mass-Flo flow controller. Hamilton syringes of 10-100µl volume were used where necessary.

Gas Handling Plant

The gas handling plant was constructed on site based on an earlier design by Kebarle [6]. The GHP was a steel box (63 x 58 x 50cm, 1mm wall thickness) insulated using 20mm thick Insulboard walls. The box enclosed several all-metal valves and the vacuum manifold. The manifold was constructed of glass and stainless steel and featured a calibrated 5L glass bulb with a septum port to allow addition of liquid samples. All of the connections were made using high vacuum CF type flanges obtained from Kurt Lesker. Copper O-rings were used everywhere in the GHP except between the 5L bulb and the adjacent valve, where a gold-plated copper O-ring was used. The volume of the bulb was calibrated using distilled water or acetone at 25°C by weight. A small correction was made to account for the additional volume due to the O-ring between the bulb and the valve. The estimated maximum error in the bulb volume calibration was 0.06%.

The manifold and bulb were evacuated initially by a rotary pump and then by an Edwards EXT 250H Turbo pump. A large (12cm diameter and 47cm long) glass Nitrogen trap was used between the GHP and the turbo pump. The large size of the trap and large diameter for the main manifold components were dictated by the desire to maximize pumping speeds. The pressure in the GHP was measured by a 1000 mbar MKS Baratron 628A absolute pressure transducer when absolute pressures of added components were required. During bakeout or pump down the pressure was normally monitored using a standard ion gauge.

The gas-handling plant was maintained at 140°C by one 250 Watt and one 1000 Watt heater. Temperature control and readout was provided by an Omega CN76033 temperature controller in combination with a Eurotherm TE10S solid state relay. To achieve a more uniform temperature distribution in the GHP, a motor-driven mixing propeller from a lab oven was used. The temperature of the bulb was determined to be 140.0±0.8°C.

Because of the possibility of electric discharge from the ion source to the GHP through the gas inlet line, preventive measures were taken. The ion source valve of the GHP was isolated from the manifold by a glass break and was mounted on a separate support assembly using ceramic stand-offs. Since typical GHP pressures are close to atmospheric, the glass break would normally be sufficient for preventing electrical breakdown. Further precautions, however, were taken. The aluminum manifold support assembly was electrically isolated from the GHP box by ceramic stand-offs. All valves were operated with valve handle assemblies consisting of a stainless steel extension rod and a plastic 80mm diameter disk. The handle assemblies could be removed when the GHP required baking. Openings in the steel walls of the GHP for valve

handle rods, gas inlet and outlet lines, and pumping lines were made considerably larger than the corresponding openings in the insulative walls. Gas inlet and pumping lines were constructed from non-conducting plastic and rubber hoses.

The gas inlet and outlet lines, MKS Baratrons, and mass flow controller were mounted so as to be electrically isolated from ground. Both MKS Baratrons were monitored by an MKS PDR-C-2C Power Supply and Readout. The flow controller was connected to an MKS 247C Power Supply and Readout. The MKS readouts were powered through a high voltage isolation transformer and were floated at near-ground potentials.

A.2 Source temperature control and pressure and flow monitoring

The ion source temperature control circuit consisted of the temperature sensor element embedded in the ion source, a Keithley 2001 Multimeter, a Keithley 7001 Switch System with 7059 switching card, an IOtech Extender488/F IEEE bus extender, a controlling computer, a Eurotherm SSDA solid state relay, and an in-house built fiber-optic computer-heater relay interface. The pressure and flow logging system included an Ontrak ADR112 analog-to-digital converter incorporating a serial interface and was connected using a Scimar OP232 optical RS232 isolator.

Even though the temperature sensor was electrically isolated from the ion source, it was assumed to be floating close to the ion source potential. A 4-wire resistance measurement of the sensor was performed by the Keithley multimeter/switching system combination that were powered through a high voltage isolation transformer. The measured signal was sent to the PC computer through a fiber-optic IEEE bus extender. Data logging and PID temperature control was achieved using a Dasylab 5.0 data acquisition software. The controlling program acquired readings every 4 seconds, performed resistance to temperature conversion, and fed the temperature reading into the incorporated PID module. The PID output was then compared with a software-generated saw-tooth function to achieve time-proportioning power control and the resulting logical output was used to turn the source heaters on and off. The heaters were controlled by the computer using the logical input solid state relay. The computer-heater interface circuit is shown in Figure A.2. The controlling program sends a suitable byte to the interface through the serial port. The UART in the computer-heater interface converted the serial data to parallel data and one of the 8 bits of parallel data was used to turn the solid state relay on or off. Since the relay was floated at the source potential, the controlling bit was sent via a fiber-optic link. The output of the solid-state relay controlled the heaters through a variac.

With this setup, the variac could be adjusted such that for any required source temperature, steady state could be achieved with 50% heater power. The solid state relay used zero-crossing switching leading to the power control time resolution of 10ms for a 50Hz power line frequency. This meant that the power could only be varied in discrete steps. The ratio of the time resolution to the period of the saw-tooth function determines the power resolution of this temperature control configuration. If the power step was too large, the source temperature oscillated independent of the PID parameters. It was found by trial and error that the saw-tooth function period should be greater than 4 seconds for our ion source.

The inner shield of the ion source was controlled by a Eurotherm 2116 temperature controller combined with a Eurotherm TE10S Solid State Relay, both powered through isolation transformers and kept at source potential. The current design of the ion source temperature control system revealed one drawback. At high temperatures requiring high heater currents, the on-off cycle of the controller had an effect on electron gun focusing. In addition, a 50Hz ripple due to AC heater current could be observed on top of mass peaks in continuous ionization mode. Further improvements to the ion source design should include incorporation of a DC-based temperature control system.

DC voltage outputs from the MKS pressure and flow meters were converted to digital form with a two-input ADR112 analog-to-digital converter and were sent via the serial interface to the controlling computer and logged by the temperature control program. The serial cable was fitted with an inline optical RS232 isolator because of the possibility that the MKS readouts would be at high voltage if electrical breakdown occurred in the gas lines. The Dasylab program for temperature control and data logging is shown in Figure A.3.

Two PRT's were incorporated into the ion source assembly: the main PRT embedded in the ion source itself with the provision for 4-wire resistance measurement and an additional PRT mounted inside the copper source jacket for 2-wire resistance measurement. Both PRT's were tested for the use as temperature sensors for the source temperature control. Better results were obtained using the main 4-wire ion source PRT. A change in the source temperature when it is in a steady state is caused by a perturbation exerted on the source. Three of the most frequent perturbations were: changes in heating power due to changes in the line voltage, heating or cooling due to gas flow through the source, and heating due to the electron beam. The first two perturbations caused the readings of both PRT's to change synchronously at a slow rate. Electron beam heating had a more pronounced effect on the main source PRT. Because of this, the inset source PRT was found to be superior for temperature control.

A.3 Determination of ion source pressure and gas residence time

Determination of ion source pressure

There was no provision for direct measurement of the ion source pressure. Instead, the pressure was measured upstream and downstream of the source. These measured pressures will be referred to as P_{in} and P_{out}, respectively. Gas lines in and out of the source were constructed symmetrically and as such, their conductances were very similar. The pressure inside the source was calculated using P_{in} and P_{out}. If the gas flows through the inlet and outlet lines were the same, the ion source pressure could be easily calculated by taking the average of P_{in} and P_{out}. However, because of the gas outflow from the source through ion exit and electron entrance slits, the pressure inside the source was not simply the average of P_{in} and P_{out}. Calculation of the source pressure thus required knowledge of conductances of these gas lines and source slits.

The conductances of the gas lines and source slits depend in a rather complicated fashion on temperatures and pressures across the lines. Our goal here is to find physically sensible functional forms for these dependencies and derive fitted coefficients from fits of experimental data.

The data for determination of conductances was collected according to the following scheme. First, the line out of the source was blanked off and methane was allowed to flow into the source through the inlet line at different flow rates. The flow was controlled by the mass flow controller and measured by an accurate MKS mass flow meter. The pressure in the blanked off outlet line and the pressure preceding the inlet line were measured. The pressure in the blanked off line was equal to the source pressure. The ratio of the known flow to the pressure drop across the gas line yields the line's conductance. The pressure in the high vacuum region outside the source was assumed to be zero. Therefore, the ratio of the flow to the source pressure yields the total conductance of the source slits. In a similar fashion, the inlet line was blanked off and gas was allowed to flow into the source through the outlet line. These measurements were done at three different source temperatures: -50°C, 35°C, and 190°C.

The gas lines were modeled in the following fashion. Inlet and outlet lines were considered to consist of essentially two different parts – the glass lines from the pressure gauge to the source flange and stainless steel lines inside the source housing. The temperature of the glass lines was always constant and maintained at 140°C by temperature controllers. The temperature of the stainless steel lines was assumed to be equal to the source temperature. Within the model, the total conductance of the gas inlet or outlet lines is a series of

conductances of the glass and stainless steel lines.

If the conductance is defined as the ratio of mass flow in sccm to the pressure difference across the gas line or source slits in mbar, then the conductance of a line under continuum flow conditions can be described by the formula following from Poiseuille's equation:

$$C = \frac{C_0(P_{in} + P_{out})}{T\sqrt{T}} \tag{A.1}$$

Since the temperature of the glass lines was constant, it can be included in the constant C_0 coefficient, but for the stainless steel lines inside the source, the temperature must be allowed to vary:

$$C_{glass} = C_1(P_{in} + P_1) \tag{A.2}$$

$$C_{steel} = \frac{C_2(P_1 + P_{src})}{T\sqrt{T}} \tag{A.3}$$

Pressure P_1 is the pressure at the point where the glass line joins the stainless steel line. It can be easily derived from the requirement that flow through the glass line is equal to flow through the stainless steel line:

$$P_1 = \sqrt{\frac{C_1 T\sqrt{T} P_{in}^2 + C_2 P_{src}^2}{C_1 T\sqrt{T} + C_2}} \tag{A.4}$$

The total conductance of the gas inlet and outlet lines has the following form corresponding to two conductances connected in a series, where C_1 and C_2 will have values determined from fits of experimental data:

$$C = \frac{C_{glass} C_{steel}}{C_{glass} + C_{steel}} \tag{A.5}$$

The conductance of the source slits will have a more complicated form. The outflow from the source through the ion exit slit that normally was of 10μm width is molecular or near molecular. The electron entrance orifice was normally of 100μm diameter and flow out of this orifice is in the transitional region between continuum and molecular. Since measured slit conductances were pressure-dependent, this flow can be neither molecular nor continuum, because both flow regimes are pressure-independent for flows through an orifice. The transitional region between the two flow regimes is the least well described and as such, there are no universal formulas for it. The conductance of the slits is assumed to be a sum of two parallel molecular and continuum conductances. For the range of source pressures and temperatures investigated, the outflow of methane gas never attained purely continuum flow,

but remained much closer to molecular flow. A sensible function to describe the transition from constant molecular to constant continuum conductance is *arctan(x)*, where x should be a function of the Knudsen number. The logarithm of the Knudsen number inside *arctan* appropriately describes the range between molecular and near transitional regions. Both molecular and continuum conductances are inversely proportional to the square root of temperature. The function used for fitting source slits conductances thus had the following form:

$$\begin{aligned} C &= \frac{C_1 + C_2 \arctan\left[A \ln(d/L) + B\right]}{\sqrt{T}} \\ L &= \frac{3.107T}{P_{src} D_m^{\,2}} \\ A &= 0.434dl \\ B &= -dl \end{aligned} \tag{A.6}$$

In the above, L is mean free path, D_m is the methane molecular diameter, d is the characteristic slit dimension, and the ratio L/d is the Knudsen number. The parameter dl represents the argument of *arctan(x)* at which *arctan* nearly reaches the horizontal asymptote. Parameters A and B are chosen such that the argument of *arctan* equals $-dl$ and dl when the Knudsen number is 1 and 0.01, respectively. Parameters D_m and dl can be chosen to assume sensible values and all other parameters will then be determined from fits of experimental data.

Conductances of gas inlet and outlet lines and the source slits, C_{in}, C_{out}, C_s, can be calculated for any combination of source temperature and inlet and outlet pressures. Therefore, the source pressure can be determined from balancing the flows into and out of the source:

$$C_{in}(P_{in} - P_{src}) = C_{out}(P_{src} - P_{out}) + C_s P_{src} \tag{A.7}$$

It is also possible to measure the conductance of the outlet line between the source rotary pump and the point where P_{out} was determined using measured values for P_{out} and assuming a perfect vacuum at the pump inlet. This part of the outlet line includes the glass capillary that limits flow through the source and reduces oil backstreaming from the pump. Its conductance is assumed to be independent of the ion source temperature and to have the form:

$$C = C_c P_{out} \tag{A.8}$$

The following flow balance equation can be written for the outlet line:

$$C_c P_{out}^2 = C_{out}(P_{src} - P_{out}) \tag{A.9}$$

Solving this equation together with Eq. (A.7), P_{src} and P_{out} can be determined having knowledge

of P_{in} only. Experimental data shows that C_c depends slightly on the flow through the capillary. However, this dependence is not strong and the average C_c can be used.

The error to be assigned to the calculated source pressure will be composed of errors of measured P_{in}, measured or calculated P_{out}, and errors in the calculated conductances. Chosen functions accurately describe the experimentally measured conductances to an error level considerably less than experimental uncertainties. Overall uncertainties were calculated from the stated accuracy of the flow meter and pressure gauge. Experimental values of conductances had larger errors at lower flow rates, due to the lowest relative accuracy of the flow meter. With increasing flow rates, the errors were observed to exponentially decrease. Since fitted conductances were used as a convenience to calculate the source pressure at temperatures and pressures other than those at which the calibration had been done, the errors assigned to calculated conductances should be similar to errors in measured conductances. Conductance errors were assumed to be a function of the flow rate only and to have the form:

$$C_{err} = y_0 + Ae^{-\frac{F}{t}} \tag{A.10}$$

Parameters y_0, A, and t were obtained from fits of experimental uncertainties against flow rate F. A new calibration should be done each time the bath gas, source slits, the gas lines or their temperature are changed.

After the first set of experiments the conductance calibration was re-checked. The outlet gas line was blanked and inlet and outlet pressures were measured. In this case, the outlet pressure is equal to the source pressure. The outlet pressure can be calculated from the model using the inlet pressure and compared to the measured value. If the conductance of the gas lines did not change, a conclusion can be made whether there are any changes in the conductance of the source slits. It was determined that the conductance of the source slits decreased by 6±2%. The estimated effect of this change on calculated source pressures is such that experimental enthalpies are changed by less than 0.04 kJ·mol^{-1} and no significant changes in entropies occur.

Gas residence time in the source

To estimate the gas residence time in the ion source, the ideal gas equation, the Bernoulli equation, and the mass conservation equation were used:

$$p = nkT \tag{A.11}$$

$$\frac{P}{mn} + \frac{v^2}{2} = const \tag{A.12}$$

$$nvA = F \tag{A.13}$$

where n is the number density, m is the carrier gas molecule mass, v is the mean flow speed, A is the cross sectional area of a flow tube or ion source, and F is the mass flow.

For each given ion source temperature, the gas flow rate required to maintain a given pressure in the source can be experimentally determined. This data can be used to calculate the mean flow speed at any given cross section of a flow path. From the Bernoulli equation it then follows that the maximum change in number density due to changes in flow speed at different cross sections is less than 0.01% and, therefore, can be neglected. Thus, it is possible to use the mass conservation equation to estimate the gas residence time in the source under the assumption that number density throughout the flow path changes only due to temperature and pressure changes:

$$t = \int_{-R}^{R} \frac{dr}{v(r)} = \int_{-R}^{R} \frac{nA(r)}{F} dr = \int_{-R}^{R} \frac{2Hp\sqrt{R^2 - r^2}}{kTF} dr \tag{A.14}$$

where R and H are radius and height of the ion source, F is the flow rate in particles/sec, and n is the number density of gas in the source.

A simple program was written to solve Eqns. (A.7) and (A.9) numerically in order to calculate the source pressure from either P_{in} and P_{out} or P_{in} and C_c and calculate the gas residence time using Eq. (A.14).

A.4 Electron gun power supply and pulse circuitry

The electron gun control system consisted of a high voltage power supply, an in-house made high voltage resistor divider, a floating filament power supply custom made by QVR Designs, a floating pulse amplifier, and a TTI TGP110 pulse generator.

Electron Gun Power Supply

The electron gun design was adapted from that of a standard Hewlett-Packard oscilloscope. The electrode configuration was modeled using the ion optics software package SimIon 6.0. The simulation results provided approximate voltages for the electrodes to minimize the electron beam diameter at the ion source entrance. The electron acceleration voltage was designed to be equal to the ion source potential.

The power supply for the electron gun consisted of two parts, the High Voltage power

supply itself and a resistor divider for the provision of voltages for the electron gun electrodes. This power supply is designed to operate in the –6..6 kV range of ion source voltages. The HV power supply was constructed in-house using two Start Spellman MP series HV modular power supplies, one with a 0..10kV output for positive ion mode and one with a –15..0kV output for negative ion mode. The optimal electrode voltages obtained using SimIon were used to design the resistor divider. The divider was designed and modeled with the aid of an electronics design software package MicroSim 8.0, and relevant schematics are shown in Figure A.4. The adjustment of electrode voltages was done by means of rotary switches for coarse and potentiometers for fine control. A high voltage digital voltmeter was constructed to monitor voltages on all of the electrodes. The approximate voltages for 4kV and –4kV modes of operation are given in Table A.1. Due to the fact that Start Spellman HV supplies have a limited output current (0.6mA for 10kV supply and 1mA for –15kV supply), the total resistance of the divider had to be large. For this configuration, any electron current intercepted by electrodes, or connection of the HV voltmeter somewhat changed all electrode voltages. Following tuning of the electron beam, the HV voltmeter remained connected to the same electrode as during the tuning procedure to prevent changes in electron beam focusing.

Ion Source	4000	-4000
Drawout	50	-7950
Extractor	330	-7670
Einzel 1	3970	-4030
Einzel 2	430	-7570
Einzel 3	3970	-4030
Y and Z deflect, center	3970	-4030

Table A.1. Electron gun voltages, Volts.

The floating filament power supply provided regulated current from 0 to 5A. The filament electron emission current was 1.3mA at 5A of filament current. At these conditions, the electron current intercepted by the ion source block was 0.01mA. No provision was made to measure the electron current entering the ion source.

Floating pulse amplifier

A battery operated floating pulse amplifier was used to pulse the drawout electrode of the electron gun to switch the electron beam on and off. The amplifier provided –140V offset to the drawout output of the electron gun supply, which, in turn, could range from 5 to 80V. The drawout electrode thus could be kept 60-135V below the filament potential in order to turn the

electron beam off and 5-80V above the filament potential to turn the beam on. The amplifier accepted a master pulse from the pulse generator and transmitted it through a fiber-optic link to a battery driven transistor amplifier, thus providing HV isolation of the input. Schematics for this circuit are shown in Figure A.5. The leads of the transistor in the amplifier were shorted together when the amplifier was turned off. This prevented the transistor from breaking down when the high voltage was switched on. With this design, the amplifier should be turned on and off only when high voltage is applied.

A.5 Ion focus circuitry

The ion source cones, focusing, and deflection electrodes were modeled with SimIon for determination of voltages needed for best focusing of the ion beam. A resistor divider circuit was designed and modeled with MicroSim for provision of voltages to cone and focusing electrodes, as shown in Figure A.6. The operating voltages for ion-focusing electrodes when operating at 4kV are given in Table A.2. All of the voltages could be adjusted by means of coarse and fine potentiometers. The resistor divider was connected in parallel with the existing VG mass spectrometer ion source focusing circuit and by design had a large impedance, such that no significant loading of the existing circuit would occur.

Ion Source	4000
Cone 1	3960
Cone 2	3230
Focus/Beam Centering	2080

Table A.2. Ion source electrodes' voltages, Volts.

Additional Y focusing and Z focusing and deflection electrodes were inserted in the analyzer part of the flight tube in the region between the ion source and the Electrostatic Analyzer to improve focusing in the mass-spectrometer. The existing VG power supply for standard VG ion focusing electrodes was modeled using MicroSim and it was determined that the power supply could be further loaded by addition of a focusing circuit for these new electrodes. The diagram of this new focusing circuit is given in Figure A.7.

A.6 Ionic profile acquisition

Ions arriving at the detector were collected by a Galileo Channeltron 4870V digital multiplier. The existing VG multiplier power supply was used to power the multiplier tube and

deflector electrode of the Channeltron. The multiplier output was fed into EG&G Ortec VT120A and VT120C fast preamplifiers that were connected in series. The preamplifiers had gains of 200 and 20 respectively. The preamplifier output was sufficient to drive the EG&G Ortec 9349 Ratemeter that was used for tuning. For data collection, the preamplifier output was connected to the discriminator input of an EG&G Ortec Turbo MCS multichannel scaler. The overall layout of the ion collection system was shown in Figure 2.1. The main pulse generator was used to provide the channel sweep triggering pulses to the scaler.

Two modes of data acquisition could be used. In manual mode, the mass spectrometer was manually tuned to a mass of interest and the scaler was programmed to collect data for a certain number of channel sweeps. It was desirable to keep the electron gun in pulsing mode when retuning the mass spectrometer from one mass to another. This is due to the sensitivity of the ion source temperature to any change in electron beam current. The reading of the ratemeter was sensitive enough to retune the mass spectrometer even in pulsing mode.

The VG data acquisition system allowed for Selected Ion Recording (SIR). In this mode, the mass spectrometer was programmed via software to monitor several masses in sequence with the possibility of magnet calibration before acquisition. The required input parameters for each mass were the mass itself, the dwell time for that mass, and the delay time between the masses. The VG data system provided an "ON CHANNEL" TTL-compatible signal (called "ON SCAN" in normal acquisition), which was kept HIGH during a mass data acquisition and set LOW when acquisition of that mass completed. As such, during a mass dwell time the "ON CHANNEL" output was held HIGH while the magnet stayed tuned to that mass. During the delay time the "ON CHANNEL" signal switched to LOW and the magnet was moved to the next mass. The "ON CHANNEL" output was used to synchronize the VG SIR mode of operation with data acquisition by the multichannel scaler.

The main pulse generator could be operated in gated mode, where the "ON CHANNEL" signal could be used to switch the pulse generator off during the delay time. However, that would also cause the electron beam to be switched off as well and, as a result, the ion source temperature would change. To avoid this, an in-house built synchronizer, shown in Figure A.8, was used. The output of the pulse generator was split into two parts: one part was continuously fed into the electron gun and the other part was fed into the synchronizer circuit. The synchronizer circuit performed synchronization and a logical AND operation on the pulse generator and the "ON CHANNEL" signals. Its output was then used to provide a START pulse to trigger channel sweeps by the multichannel scaler. The synchronizer circuit also

detected the falling edge of the "ON CHANNEL" signal and provided a STOP pulse to the multichannel scaler. The scaler was configured for an unlimited number of sweeps and the STOP signal was used to terminate a mass acquisition by the scaler. Due to the fact that the "ON CHANNEL" signal and the pulse generator had independent timing as can be seen from the timing diagram in Figure A.8, the scaler performed one extra channel sweep during the delay time, when the magnet was already switched to another mass. This effect was eliminated by programming the VG SIR acquisition and the scaler such, that each mass appears in the SIR scan list twice in series. The recording is performed by the scaler only during the first appearance of a mass and the dwell and delay time for the second appearance of this same mass are small. This was to ensure that all counts and signal averaging pertain to the mass in question. Obtained ionic profiles were used for determination of equilibrium ratios of ion abundances. Visualization of ionic profiles and averaging of the ratio of ionic abundances were performed using a Windows program custom-written for this purpose.

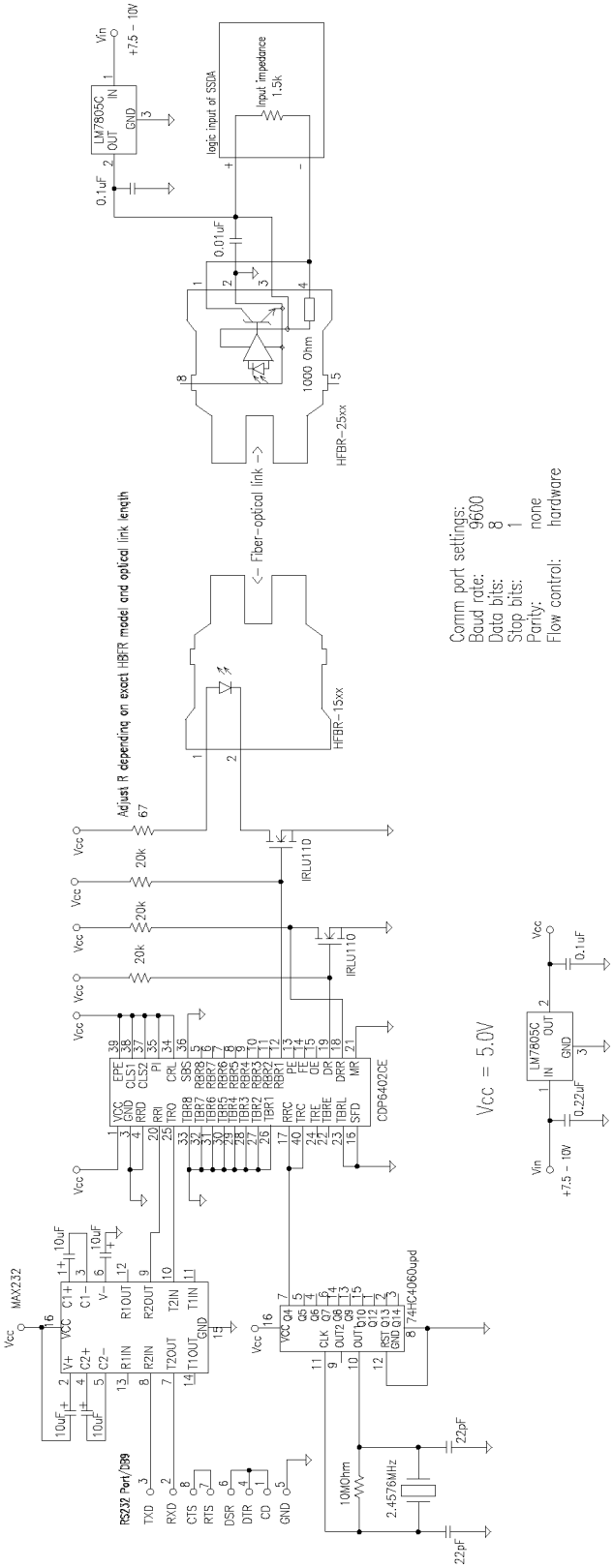

Figure A.2. Computer-heater interface.

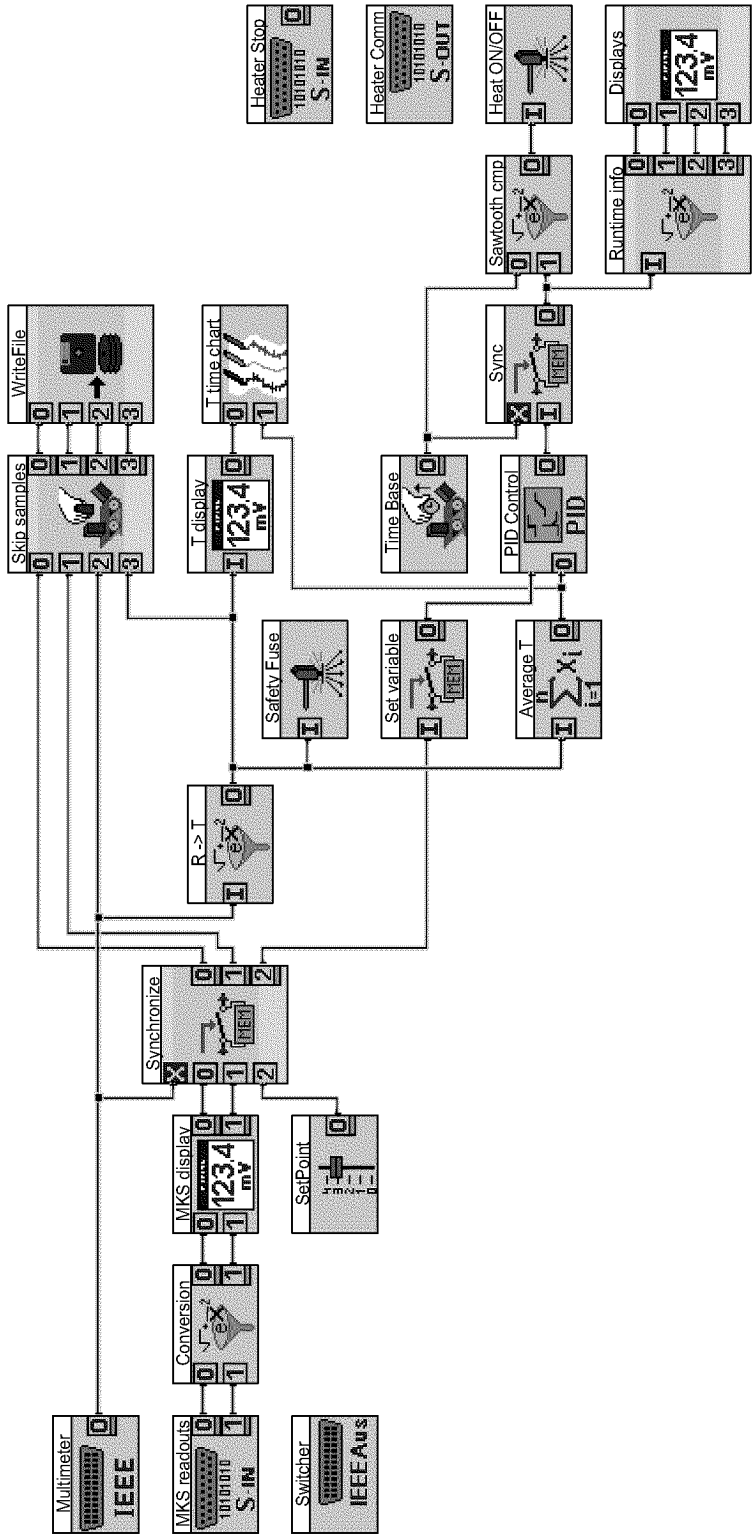

Figure A.3. Dasylab temperature control and data logging worksheet.

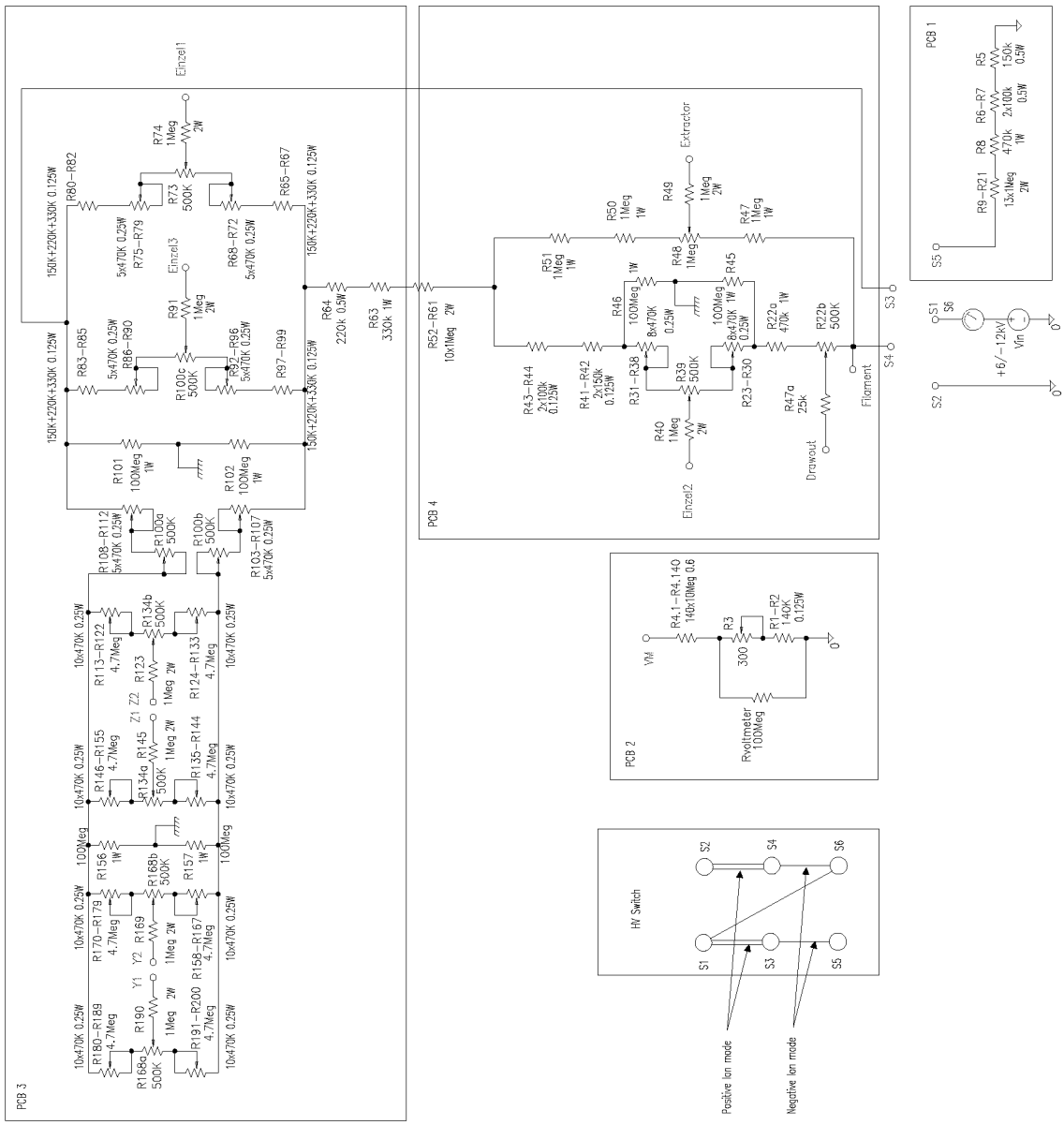

Figure A.4. Electron gun resistor divider.

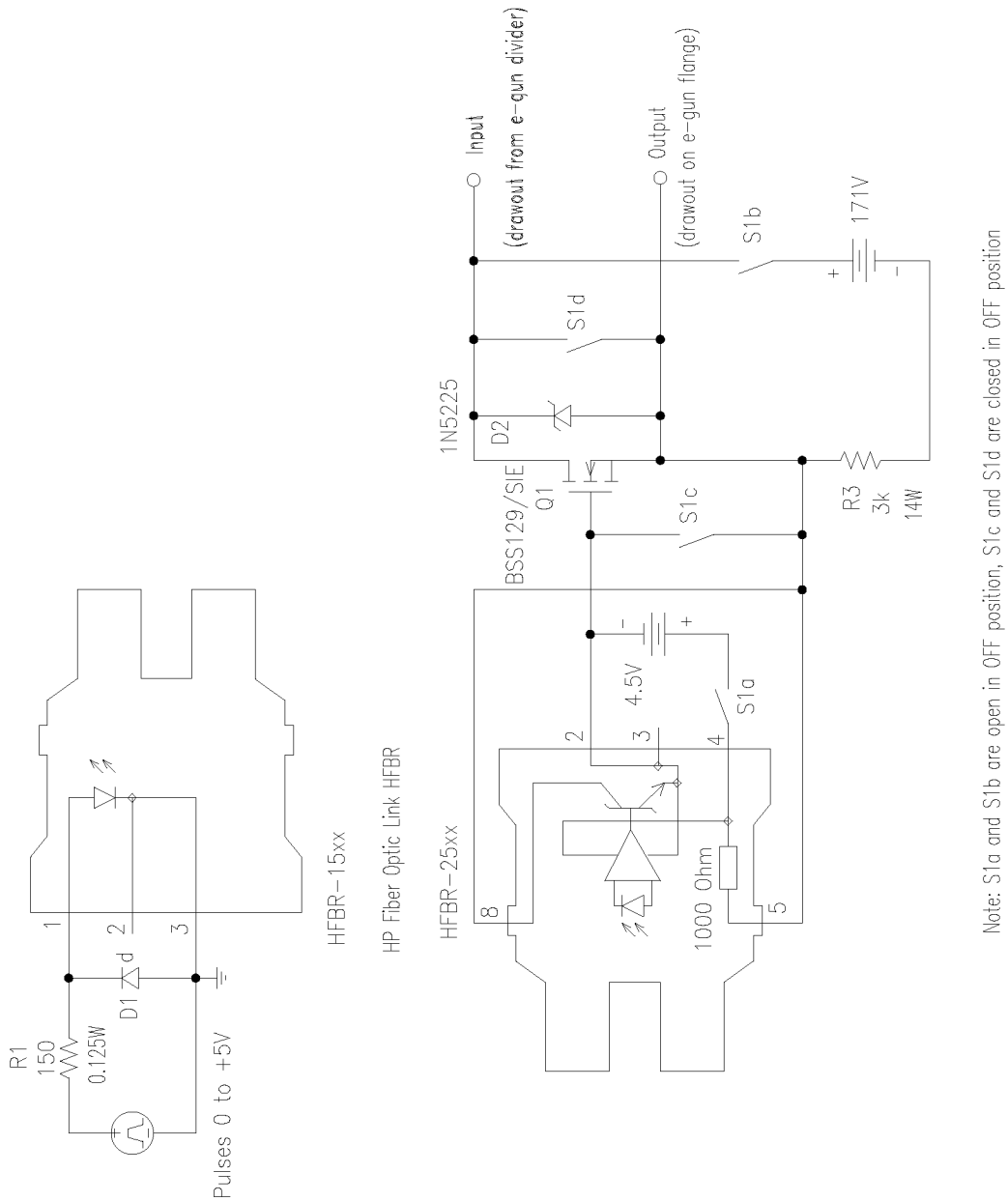

Figure A.5. Floating pulse amplifier.

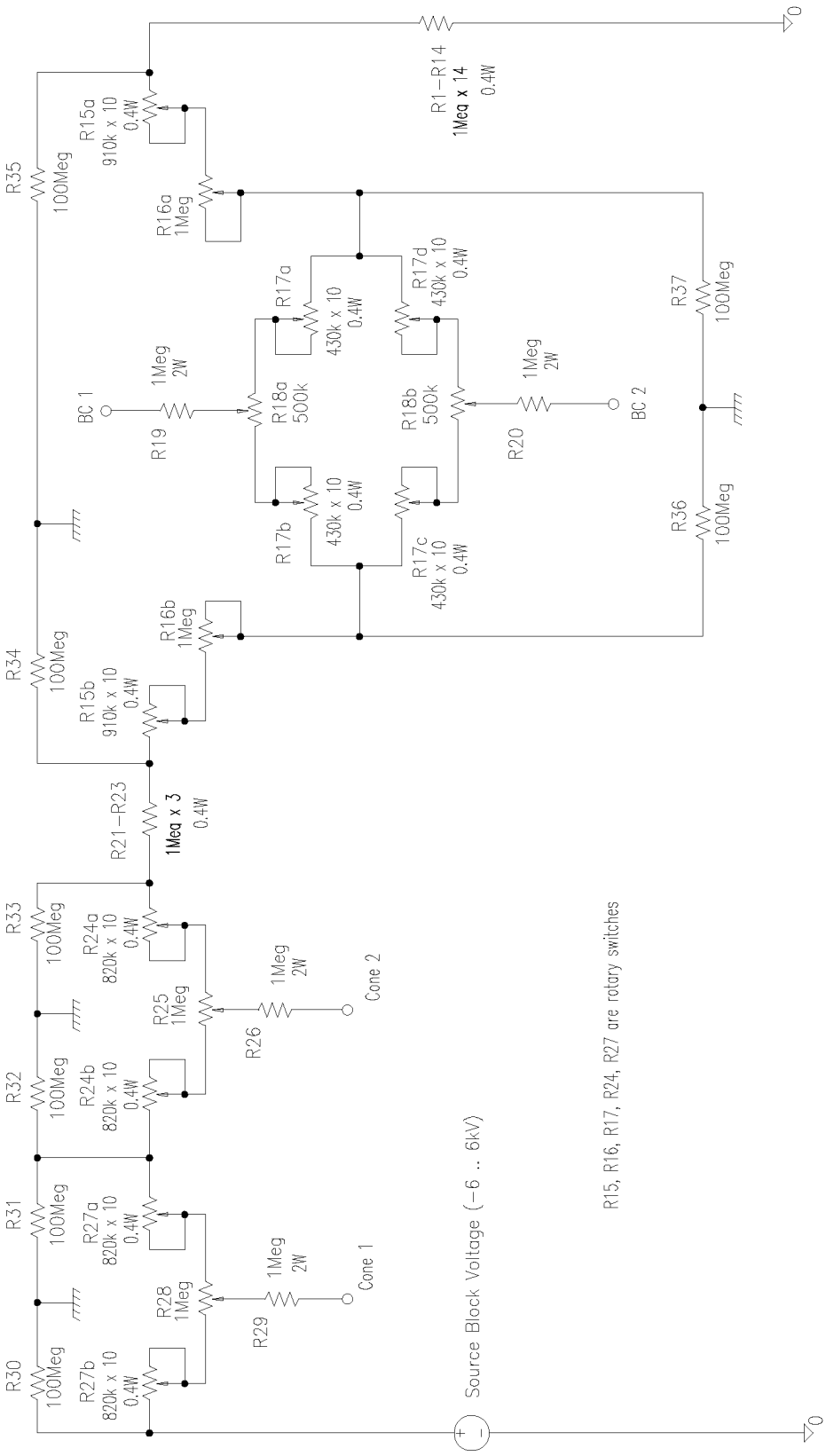

Figure A.6. Ion source beam focusing.

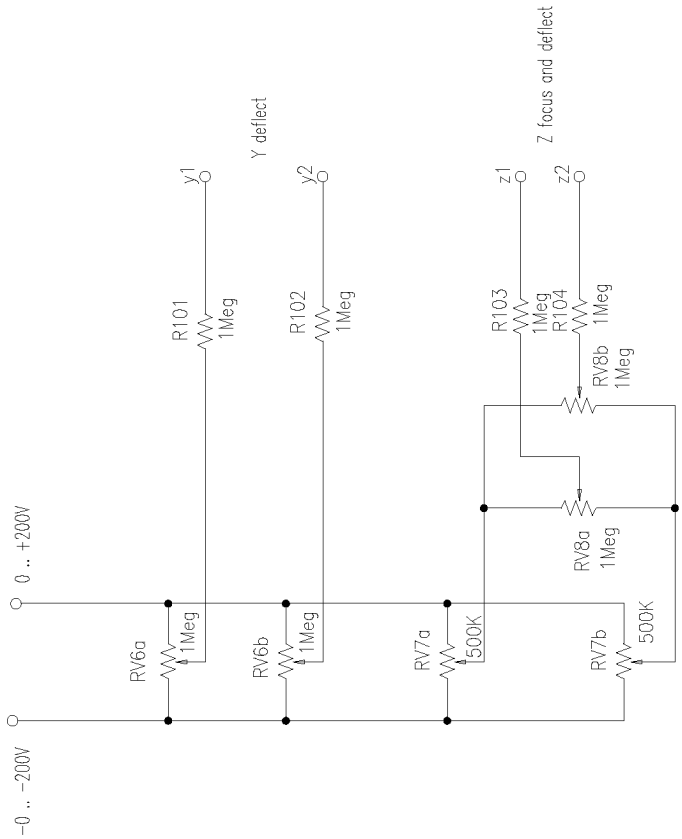

Figure A.7. Additional Y and Z focusing and deflection.

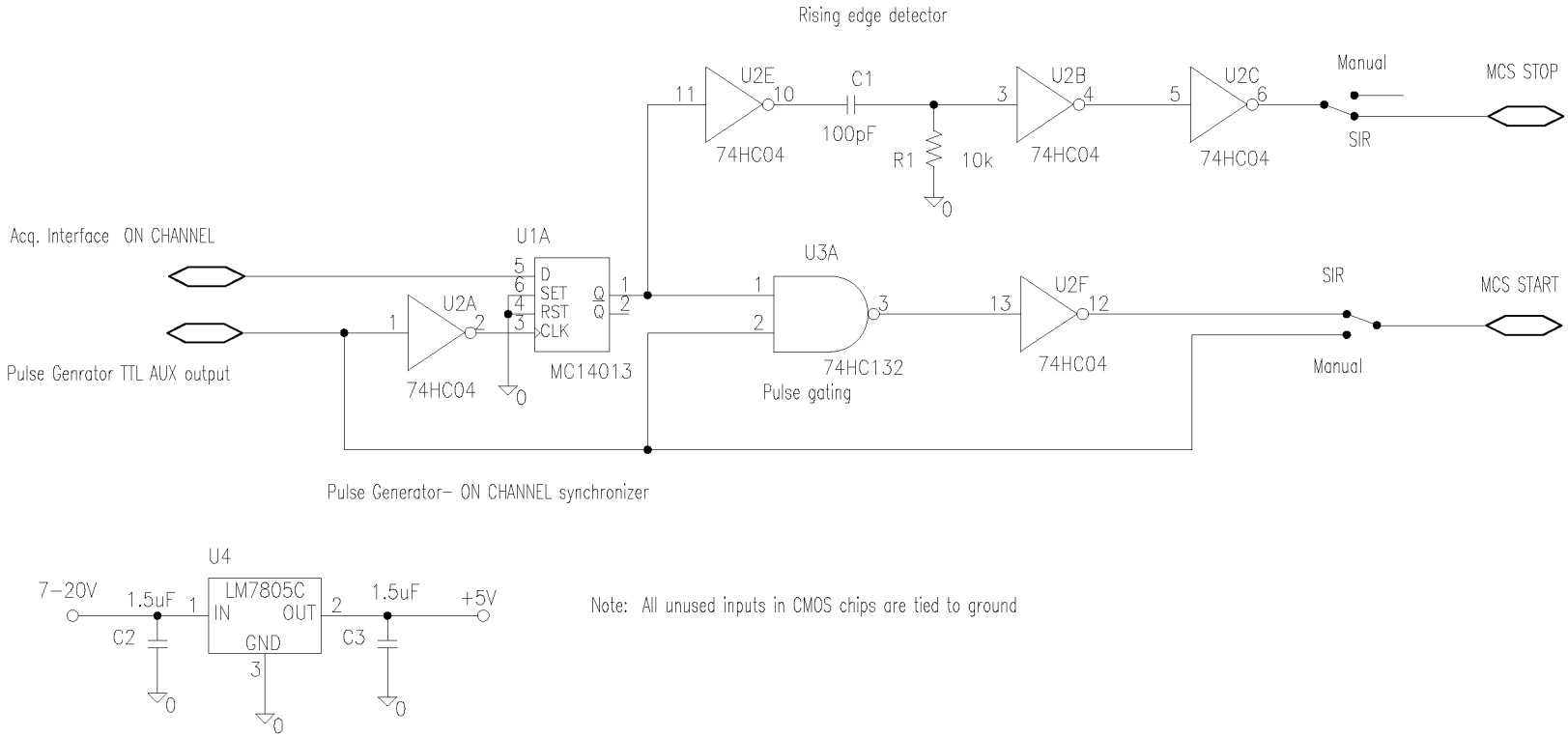

Figure A.8. Synchronizer.

Appendix B. Experimental Results

Table B.1. Equilibrium constants as a function of temperature for reaction

$$Cl^-(H_2O)_{n-1} + H_2O = Cl^-(H_2O)_n$$

$\ln K_{01}$	1000/T(K)	$\ln K_{12}$	1000/T(K)	$\ln K_{23}$	1000/T(K)	$\ln K_{34}$	1000/T(K)
7.2493	2.2698	5.2811	2.4061	5.0783	2.8867	5.5994	3.4105
8.2410	2.4061	6.2571	2.5598	6.2381	3.0597	6.7931	3.5992
9.3653	2.5598	7.3770	2.7324	7.5173	3.2541	7.6160	3.7307
10.6417	2.7324	8.2309	2.8867	8.5351	3.4105	8.1761	3.8289
11.7548	2.8867	9.4411	3.0597	9.7261	3.5992	9.0220	3.9511
13.0090	3.0597	10.7247	3.2541	10.6014	3.7307	9.4780	4.0255
		11.7812	3.4105	11.1854	3.8289	9.9849	4.1043
				12.0249	3.9511		
				12.4400	4.0255		

$\ln K_{45}$	1000/T(K)	$\ln K_{56}$	1000/T(K)	$\ln K_{67}$	1000/T(K)	$\ln K_{78,\ corr}$	1000/T(K)
6.5757	3.8288	6.2057	3.9510	6.6184	4.1065	7.5097	4.1953
7.2945	3.9511	6.6873	4.0255	7.1853	4.1953	7.9526	4.2792
7.7127	4.0255	7.2061	4.1043	7.7355	4.2792	8.4062	4.3705
8.1424	4.1043	7.7585	4.1953	8.3073	4.3705		
8.7336	4.1953	8.2921	4.2792				
9.2930	4.2792	8.8738	4.3705				

Table B.2. Equilibrium constants as a function of temperature for reaction

$$Br^-(H_2O)_{n-1} + H_2O = Br^-(H_2O)_n$$

$\ln K_{01}$	1000/T(K)	$\ln K_{12}$	1000/T(K)	$\ln K_{23}$	1000/T(K)	$\ln K_{34}$	1000/T(K)
5.6952	2.3227	5.5035	2.7321	4.6317	3.0595	4.3169	3.4156
7.2041	2.5599	6.4456	2.8866	5.9369	3.2548	5.5214	3.6035
8.2939	2.7321	7.4909	3.0595	6.9064	3.4156	6.3144	3.7310
9.3317	2.8866	8.6688	3.2548	8.0463	3.6035	6.8837	3.8287
10.3640	3.0595	9.6428	3.4156	8.8547	3.7310	7.5593	3.9459
11.6987	3.2548	10.8210	3.6035	9.4684	3.8287	8.0490	4.0248
12.6964	3.4156			10.2183	3.9459	8.6214	4.1096
				10.7041	4.0248	9.2415	4.1910
				11.2328	4.1096	9.6625	4.2792

$\ln K_{45}$	1000/T(K)	$\ln K_{56}$	1000/T(K)	$\ln K_{67}$	1000/T(K)
6.3263	3.9459	5.6605	3.9471	6.7020	4.1910
6.8430	4.0248	6.1307	4.0248	7.2551	4.2792
7.3229	4.1096	6.6468	4.1096	7.7988	4.3649
7.8379	4.1910	7.1472	4.1910		
8.3512	4.2792	7.6858	4.2792		
8.8866	4.3642	8.2123	4.3642		

Table B.3. Equilibrium constants as a function of temperature for reaction

$$I^-(H_2O)_{n-1} + H_2O = I^-(H_2O)_n$$

$\ln K_{01}$	1000/T(K)	$\ln K_{12}$	1000/T(K)	$\ln K_{23}$	1000/T(K)	$\ln K_{34}$	1000/T(K)	$\ln K_{45}$	1000/T(K)
5.4133	2.6563	6.2448	3.2549	5.1857	3.4838	5.3938	3.8609	6.3028	4.1079
6.4784	2.8457	7.5964	3.4838	6.2625	3.6652	6.2687	3.9903	6.7017	4.1783
7.6618	3.0598	8.5488	3.6652	7.4839	3.8609	6.9766	4.1079	7.2224	4.2744
8.7349	3.2549	9.6115	3.8609	8.2718	3.9903	7.4043	4.1783	7.7004	4.3667
10.0143	3.4838	10.3811	3.9903	8.9309	4.1079	7.9860	4.2744		
10.9857	3.6652	11.0442	4.1079	9.4352	4.1783	8.5151	4.3667		
		11.4281	4.1783	10.0306	4.2744				
		11.9609	4.2744	10.5328	4.3667				

Table B.4. Equilibrium constants as a function of temperature for reaction

$$H^+(H_2O)_{n-1} + H_2O = H^+(H_2O)_n$$

$\ln K_{12}$	1000/T(K)	$\ln K_{23}$	1000/T(K)	$\ln K_{34}$	1000/T(K)
7.2305	1.2351	5.7246	1.6942	5.0628	2.1257
8.0239	1.2824	7.8057	1.8857	7.4182	2.3778
8.8134	1.3337	10.3918	2.1257	10.3638	2.6959
9.7094	1.3891	13.1210	2.3778	12.0976	2.8900
10.6931	1.4493				
11.7407	1.5151				

$\ln K_{45}$	1000/T(K)	$\ln K_{56}$	1000/T(K)	$\ln K_{67}$	1000/T(K)
5.9531	2.8900	6.7179	3.3653	6.6284	3.7148
7.5346	3.1083	7.6344	3.5066	7.3317	3.8002
9.4081	3.3653	8.0112	3.5618	8.0169	3.8858
10.7580	3.5618	9.0210	3.7148	8.8216	3.9815
		9.5714	3.8002		
		10.0510	3.8858		
		10.6532	3.9815		

Appendix C. Quantum Mechanical Calculations

This chapter lists the results from quantum chemical calculations. The optimized geometries are given in terms of Cartesian coordinates in angstroms. Vibrational frequencies were scaled using the factor 0.89 and recalculated to corresponding vibrational temperatures. For halide water clusters, (S) and (I) designate surface and interior geometries, respectively. All the calculations were done using the B3LYP method. The 6-311++G** basis set for H, O, Cl, Br and the CRENBL ECP basis set for I were used for halide clusters. In the proton hydration calculations, the 6-311G** basis set was used for all atoms.

Geometry of water with 6-311++G** basis set

O	0.000000		
H	0.961971	0.000000	
H	0.961971	1.527808	0.000000

Electronic energy for water, [Hartree/particle]: -76.4585310

Rotational temperatures for water, [K]: 39.6365, 20.6203, 13.5639

Vibrational temperatures for water, [K]: 2051.01, 4888.94, 5024.20

Electronic energies for halide water clusters, [Hartree/particle]

Ion	n=0	n=1	n=2(I)	n=2(S)	n=3(I)	n=3(S)
Cl	-460.303727	-536.785922	-613.265362	-613.267492	-689.745042	-689.749696
Br	-2574.237796	-2650.716687	—	-2727.196341	—	-2803.677575
I	-111.565583	-188.040873	-264.514270	-264.518203	-340.990761	-340.998352

Ion	n=4(I)	n=4(S)	n=5(I)	n=5(S)	n=6(I)	n=6(S)
Cl	-766.225798	-766.230333	-842.702253	-842.707756	-919.180830	-919.189936
Br	-2880.151162	-2880.157653	-2956.630401	-2956.635009	-3033.104565	-3033.115334
I	-417.469518	-417.477873	-493.943875	-493.954617	-570.421183	-570.433229

Ion	n=7(I)	n=7(S)	n=8(I)	n=8(S)
Cl	-995.658470	-995.671356	-1072.137781	-1072.146345
Br	-3109.582942	-3109.596031	-3186.061447	-3186.070778
I	-646.899627	-646.912597	—	-723.386976

Geometries of Cl^- water clusters; number of water molecules is given by *n*.

n=1

O	0.028746	2.016254	0
Cl	0.028746	-1.129203	0
H	0.214099	1.044611	0
H	-0.932754	2.021813	0

n=2(I)

Cl	-0.000088	-0.030787	-0.014310
O	3.180211	-0.048379	-0.022485
H	2.218054	-0.225046	-0.121783
H	3.171319	0.801591	0.427014
O	-3.177451	0.102789	-0.026086
H	-3.200595	-0.727937	0.457563
H	-2.209362	0.239485	-0.130958

n=2(S)

O	-1.609122	-1.396737	0.013288
O	-1.090632	1.570395	-0.091297
Cl	1.489126	-0.148485	0.002741
H	-0.63496	-1.378075	0.039389
H	-1.802758	-0.453278	-0.091703
H	-1.061848	1.855193	0.826971
H	-0.217539	1.111143	-0.197184

n=3(I)

O	-2.611238	-1.400533	0.042089
O	-2.091074	1.554883	-0.098351
Cl	0.529873	-0.135239	-0.024840
H	-1.640069	-1.416941	0.070567
H	-2.778436	-0.452406	-0.070067
H	-2.058551	1.865472	0.811416
H	-1.206486	1.131168	-0.213259
O	3.720513	0.051319	0.086081
H	2.748848	0.136022	0.195030
H	3.781251	-0.609615	-0.609962

n=3(S)

O	1.042881	-0.38871	1.685568
O	1.037387	1.656204	-0.506876
O	1.03991	-1.265486	-1.180996
Cl	-1.712245	-0.001021	0.001159
H	0.088135	-0.267481	1.51287
H	1.297947	-0.953576	0.938789
H	0.085668	-1.175596	-0.987396
H	1.296094	-0.336711	-1.296922
H	0.083298	1.442223	-0.523588
H	1.2956	1.292438	0.354976

n=4 (I)

O	2.082773	1.577583	-0.348052
O	1.832419	-1.253507	-1.227352
O	1.781347	-0.584573	1.681566
Cl	-0.875991	0.183527	-0.078069
H	1.113866	1.50425	-0.42865
H	2.240235	1.128912	0.498676
H	0.843897	-0.373217	1.516395
H	2.00055	-1.114567	0.898158

H	0.878104	-1.101527	-1.097198
H	2.169623	-0.34316	-1.256558
O	-4.09199	-0.007002	0.05926
H	-3.148247	0.250929	0.072965
H	-4.042579	-0.931584	-0.199989

n=4 (S)

Cl	-1.568149	-0.832836	-0.110115
O	0.515232	0.50221	2.08992
H	1.173334	-0.070363	1.656065
H	-0.31588	0.102947	1.774009
O	-0.225544	2.200734	-0.149696
H	0.190711	1.90405	0.679901
H	-0.933961	1.53917	-0.249227
O	0.930125	0.265843	-1.987472
H	0.771742	1.104558	-1.517523
H	0.106415	-0.216337	-1.79025
O	1.678146	-1.429385	0.250842
H	1.752939	-0.870127	-0.543603
H	0.729549	-1.650898	0.23384

n=5 (I)

O	2.456831	-0.321733	1.672891
O	2.55047	1.594862	-0.582923
O	2.359398	-1.316113	-1.129572
Cl	-0.375085	0.131021	0.02754
O	-3.611832	1.409466	-0.029345
H	1.499601	-0.175581	1.57465
H	2.639145	-0.93401	0.941242
H	1.408165	-1.187351	-0.966537
H	2.656074	-0.403896	-1.282228
H	1.581811	1.513519	-0.603662
H	2.759693	1.238637	0.296684
H	-2.644452	1.457509	-0.044989
H	-3.757392	0.454697	0.056275
O	-3.073423	-1.517346	0.088345
H	-2.184655	-1.118535	0.212615
H	-3.033098	-1.865432	-0.807385

n=5 (S)

O	-1.287468	0.803818	1.681658
O	1.539512	0.357431	1.487648
O	2.050408	-1.945706	0.112074
O	-0.293064	-1.271584	-1.436446
O	-2.528249	-1.311705	0.119331
Cl	0.277643	1.844442	-1.026412
H	1.410318	0.943843	0.710902
H	0.636654	0.34932	1.859354
H	-1.016981	1.319642	0.897753
H	-1.773195	0.051123	1.297484
H	-0.115122	-0.304506	-1.458044
H	0.480566	-1.639098	-0.969246
H	1.888945	-1.162756	0.697456
H	2.824915	-1.700563	-0.402497
H	-1.722912	-1.38268	-0.454341
H	-3.182227	-0.887872	-0.443935

n=6 (I)

Cl	-0.001426	-0.004919	-0.018105
O	2.880968	-0.747449	-1.524445
O	2.857156	1.711387	0.11791
O	2.874533	-0.950527	1.417686
O	-2.856492	0.705873	1.559426
O	-2.890789	0.994002	-1.378185
H	3.098858	0.170697	-1.292549
H	1.916391	-0.759721	-1.407605
H	3.079224	1.055073	0.79917
H	1.89542	1.597988	0.036986
H	1.910331	-0.843648	1.366453
H	3.097155	-1.192235	0.502717
O	-2.862578	-1.703454	-0.158436
H	-1.898793	-1.595256	-0.093155
H	-3.097502	-1.02376	-0.812034
H	-1.893726	0.723276	1.428932
H	-3.076948	-0.204105	1.299197
H	-1.929209	0.860709	-1.337098
H	-3.099343	1.215959	-0.454871

n=6 (S)

O	1.701676	-1.237848	-1.455302
Cl	1.123055	1.770856	-0.255318
O	1.806781	-0.695341	1.440365
O	-1.787341	1.18177	1.400652
O	-0.983314	-1.552203	1.619223
O	-1.130517	-1.862965	-1.206371
O	-1.887724	0.890568	-1.444377
H	-0.91462	1.534589	1.158724
H	-1.607727	0.240187	1.601309
H	1.611171	0.166387	0.986673
H	2.442434	-0.479497	2.128571
H	-0.988951	1.262213	-1.439881
H	-2.151603	1.021172	-0.512901
H	1.592611	-0.269097	-1.41556
H	1.97415	-1.439802	-0.548121
H	-1.491381	-0.974981	-1.404051
H	-0.183471	-1.778931	-1.422872
H	-1.102518	-1.786406	0.674125
H	-0.02852	-1.39223	1.700869

n=7 (I)

O	-2.416145	0.160167	-1.939914
O	-2.626024	2.079561	0.13795
O	-2.590169	-2.089824	-0.151721
O	-2.445503	-0.165087	1.933055
Cl	0.277328	-0.014088	0.012038
H	-1.494159	-0.17081	1.734329
H	-2.73964	0.645153	1.475154
H	-2.740516	-1.536729	0.642158
H	-1.625086	-2.1006	-0.211896
H	-2.708343	-0.654997	-1.489382
H	-1.466969	0.171652	-1.730765
H	-1.663372	2.116178	0.216772
H	-2.747824	1.52094	-0.657486
O	3.143032	1.632208	-0.535524
O	3.200194	-1.259278	-1.129237
O	3.188841	-0.332726	1.662221

H	2.182049	1.527833	-0.438485
H	3.383225	0.829073	-1.027281
H	2.235068	-1.156082	-1.113349
H	3.417011	-1.267013	-0.181425
H	2.225256	-0.386951	1.554235
H	3.394921	0.501687	1.208145

n=7 (S)

Cl	-2.609173	-0.023655	-0.28089
O	-0.715571	-1.868284	1.280355
O	-0.701219	2.124877	0.788824
O	-0.049504	-0.301815	-2.443867
O	1.358092	-2.117148	-0.798529
H	0.894099	-1.588291	-1.48298
H	0.693457	-2.206839	-0.096265
H	-0.907696	-0.234144	-1.990276
H	0.432636	0.505779	-2.171109
H	-1.360991	1.474213	0.42906
H	-1.222217	2.88924	1.051398
H	-1.371349	-1.31719	0.776503
H	-1.238892	-2.558967	1.69725
O	0.866551	0.292729	2.41673
O	1.392639	1.860412	-1.25436
H	0.35331	1.011339	2.00816
H	0.352214	-0.504953	2.202426
H	0.73171	2.124132	-0.593677
H	2.026586	1.309471	-0.747426
O	2.865474	0.028516	0.337017
H	2.499018	-0.78226	-0.072079
H	2.342359	0.126318	1.154784

n=8 (I)

Cl	0.027486	-0.337913	-0.33333
O	-3.033124	-1.007671	-1.246462
O	-3.397741	1.847626	-1.026094
O	-2.258791	1.177713	1.411434
O	-3.408735	-1.468802	1.466254
H	-3.389042	-1.40322	0.482938
H	-2.644282	-2.014622	1.677237
H	-2.742773	0.362156	1.64165
H	-1.430385	0.833602	1.024939
H	-2.062078	-0.941091	-1.175059
H	-3.310152	-0.076511	-1.338192
H	-3.052873	1.735371	-0.109244
H	-2.659791	2.23058	-1.510871
O	3.576589	1.320431	1.548084
O	2.7051	1.406401	-1.21194
O	3.058111	-1.396187	-1.613994
O	2.709003	-1.282408	1.240016
H	3.067921	-1.5076	0.360289
H	1.773867	-1.103583	1.025285
H	2.09674	-1.508762	-1.634904
H	3.147815	-0.421991	-1.635016
H	1.787684	1.137053	-1.027598
H	3.084969	1.544031	-0.32464
H	3.330551	0.364778	1.544812
H	2.931264	1.737495	2.126585

n=8 (S)

Cl	2.910098	-0.860638	-0.317611
O	1.905356	1.824697	0.762067
O	0.540555	-1.951383	1.286067
O	0.426388	-0.219747	-2.446574
O	-0.189597	2.265714	-1.247288
H	0.024394	1.484584	-1.801953
H	0.546243	2.301435	-0.61401
H	1.25472	-0.466891	-1.997746
H	-0.255725	-0.759134	-2.002385
H	1.339746	-1.663165	0.769217
H	0.813319	-2.749379	1.748391
H	2.293743	0.983615	0.400939
H	2.661942	2.370675	0.995229
O	-0.169276	0.649345	2.402996
O	-1.526217	-1.443044	-0.695426
H	0.038393	-0.279299	2.199148
H	0.564817	1.14433	1.997993
H	-0.92167	-1.821956	-0.03496
H	-1.750644	-0.563787	-0.324503
O	-2.134006	1.095081	0.400459
H	-1.582509	1.633553	-0.20941
H	-1.592827	1.022147	1.213028
O	-4.493925	-0.585039	-0.053104
H	-3.907854	0.158433	0.163161
H	-3.871989	-1.249308	-0.376314

Rotational temperatures for Cl^- water clusters, [K]

n=1	n=2(I)	n=2(S)	n=3(I)	n=3(S)	n=4(I)	n=4(S)
26.20778	12.52852	0.30664	0.30493	0.15516	0.15475	0.08213
0.21176	0.06850	0.16922	0.05391	0.10221	0.04115	0.07933
0.21006	0.06830	0.10988	0.04605	0.10219	0.04109	0.07907

n=5(I)	n=5(S)	n=6(I)	n=6(S)	n=7(I)	n=7(S)	n=8(I)	n=8(S)
0.10518	0.05798	0.07941	0.04790	0.05534	0.04147	0.04457	0.03957
0.03046	0.05623	0.02372	0.04516	0.02036	0.03129	0.01540	0.02123
0.02785	0.04596	0.02369	0.04028	0.01998	0.03121	0.01530	0.02063

Vibrational temperatures for Cl^- water clusters, [K]

n=1	n=2(I)	n=2(S)	n=3(I)	n=3(S)	n=4(I)	n=4(S)
234.48	11.13	105.83	11.28	112.81	15.11	52.64
440.28	15.14	200.82	15.2	115.26	20.42	106.66
938.69	43.07	250.18	60.38	160.82	55.41	113.41
2136.92	182.02	264.59	98.64	195.99	112.68	124.6
4317.01	254.37	444.1	193.76	200.28	119.17	149.99
4959.19	397.78	522.62	200.1	254.75	140.75	244.97
	407.63	610.92	258.41	503.32	195.72	246.86
	881.44	861.56	270.22	514.52	198.84	247.66
	884.71	1026.91	402.68	561.18	204.38	250.62
	2131.18	2125.31	422.04	602.11	263.06	512.11
	2142.53	2178.28	510.14	603.32	377.35	521
	4442.57	4230.93	590.77	860.07	493.76	544.2
	4481.27	4665.98	842.81	896.04	502.54	553.94
	4962.15	4806.71	852.4	898.3	550.47	621.83
	4962.75	4955.91	987.39	1092.22	613.23	774.53
			2122.47	2164.69	618.43	776.89
			2134.43	2166.59	817.54	851.51
			2176.35	2192.68	841.91	885.59
			4342.42	4569.61	866.13	954.38
			4509.11	4571.96	870.28	958.37
			4730.11	4610.36	1103.95	1164.86
			4805.32	4753.55	2129.07	2181.19
			4958.55	4779.97	2164.38	2185.92
			4959.68	4780.43	2166.8	2186.72
					2190.01	2208.88
					4573.21	4615.48
					4641.35	4638.07
					4644.55	4644.73
					4660.21	4654.04
					4749.51	4699.03
					4766.73	4702.76
					4769.97	4705.11
					4965.63	4721.16

n=5(l)	n=5(S)	n=6(l)	n=6(S)	n=7(l)	n=7(S)	n=8(l)	n=8(S)
5.58	48.26	10.66	77.58	11.62	78.48	13.87	40.53
18.2	60.93	25.47	90.62	24.57	80.78	19.14	50.53
22.84	84.48	27.57	98.05	30.80	85.56	19.56	81.65
78.77	103.65	97.51	108.85	41.69	98.21	29.22	82.13
107.5	157.73	99.63	116.65	58.96	101.11	53.19	91.06
111.14	164.72	109.79	136.21	89.85	130.20	57.85	99.14
147.31	201.62	111.32	152.28	105.50	157.16	85.93	102.70
192.67	230.15	114.90	194.32	107.31	191.32	108.09	132.46
196.58	240.47	180.05	219.19	111.00	199.72	118.09	164.65
205.66	262.37	190.44	233.56	130.43	209.07	149.78	174.74
221.41	330.96	194.68	239.72	176.36	222.30	156.30	195.89
258.66	343.43	199.13	267.35	198.85	232.59	168.86	204.66
263.86	358.53	202.73	271.03	201.05	253.99	208.58	216.93
389.68	361.29	232.69	280.46	235.00	274.24	235.24	228.98
478.32	541.2	260.35	283.15	255.22	279.93	242.35	236.97
481.2	570.14	454.50	317.04	257.80	283.61	245.14	263.57
486.62	617.67	468.39	495.93	279.85	292.48	254.92	270.56
527.81	638.11	470.77	540.10	281.60	303.81	267.44	283.99
549.62	716.55	485.86	558.39	465.88	317.33	301.40	290.47
614.04	836.89	502.69	603.68	466.35	341.84	309.44	304.78
620.68	873.8	533.07	637.33	471.61	499.97	319.20	335.79
813.44	912.81	626.78	700.25	475.56	548.94	363.03	345.99
821.92	946.99	629.59	734.16	494.17	617.80	393.75	369.45
833.86	1030.4	630.34	783.65	516.89	670.99	420.89	467.01
839.37	1074.83	632.65	823.56	532.09	702.13	508.01	503.01
921.03	1215.84	797.88	847.03	620.91	722.44	514.86	517.22
1114.64	1273.53	801.18	888.94	629.78	739.01	521.44	558.06
2116.33	2164.64	806.05	904.39	631.92	779.78	571.14	619.32
2161.25	2167.04	811.21	981.46	691.85	810.32	583.68	666.87
2162.39	2175.73	818.82	1002.44	785.31	863.61	618.89	687.38
2168.05	2180.47	824.14	1043.61	795.04	897.50	623.30	723.61
2188.01	2208.54	1122.72	1078.17	799.29	922.65	642.75	741.11
4474.62	4220	1133.86	1296.32	809.86	931.57	679.45	793.89
4673.11	4244.47	2160.45	2087.71	817.29	995.56	807.77	822.02
4679.17	4442.34	2160.50	2167.85	865.48	1016.24	834.75	839.52
4698.05	4495.44	2160.99	2180.04	968.22	1033.09	845.00	873.06
4761.56	4583.25	2162.00	2195.17	986.45	1061.55	858.13	906.71
4763.4	4638.22	2175.68	2202.92	1132.88	1094.33	912.57	939.64
4766.71	4650.61	2194.57	2218.26	1250.60	1316.53	973.85	969.89
4769.57	4673.4	4674.99	4181.39	2160.05	2091.27	979.07	1008.00
4835.29	4962.57	4678.57	4455.28	2161.02	2101.22	983.38	1030.66
4963.24	4964.69	4707.21	4544.99	2173.58	2179.09	1067.24	1040.15
		4711.04	4556.65	2174.35	2184.87	1099.59	1080.45
		4713.28	4615.29	2190.75	2199.05	1253.75	1133.98
		4715.85	4628.68	2192.01	2212.91	1291.13	1329.98
		4763.62	4671.19	2203.69	2218.39	2160.22	2090.27
		4767.25	4715.72	4509.50	4140.02	2160.77	2099.72
		4768.66	4733.35	4555.61	4212.91	2161.04	2150.42
		4770.80	4748.85	4635.23	4426.93	2177.05	2169.24
		4773.04	4826.38	4645.22	4497.40	2180.05	2189.79
		4792.86	4970.68	4674.59	4543.37	2181.25	2202.79
				4713.38	4569.16	2189.94	2213.57
				4719.04	4618.52	2196.58	2221.23
				4734.88	4687.17	4335.58	4127.73
				4743.76	4701.50	4342.27	4201.30
				4769.35	4722.80	4385.77	4399.12
				4774.06	4757.48	4548.55	4487.32
				4793.11	4760.36	4600.87	4506.47
				4860.01	4967.75	4616.68	4553.46
				4870.13	4968.36	4624.12	4608.64
						4642.63	4669.46
						4647.67	4685.79
						4650.18	4711.57
						4664.62	4738.85
						4706.69	4749.71
						4834.67	4750.83
						4947.03	4890.47
						4953.04	4966.03
						4963.36	4966.71

Geometries of Br^- water clusters; number of water molecules is given by *n*.

n=1

O	-2.619937	-0.084054	-0.000048
Br	0.720743	0.00227	-0.000003
H	-1.656649	-0.284745	0.000406
H	-2.609845	0.877723	0.000095

n=2

O	1.783813	1.53239	-0.088348
O	2.204679	-1.428517	0.012511
Br	-1.090379	-0.053866	0.001421
H	1.232917	-1.42667	0.040854
H	2.38972	-0.48238	-0.090993
H	0.880394	1.15765	-0.226588
H	1.752311	1.805735	0.83369

n=3

O	-1.644084	-0.032717	1.713519
O	-1.634463	-1.472207	-0.887583
O	-1.635918	1.50471	-0.831135
Br	1.341085	0.000142	0.001387
H	-0.680693	0.044185	1.578998
H	-1.870955	-0.738298	1.085652
H	-0.671578	-1.39366	-0.749546
H	-1.860519	-0.576088	-1.186489
H	-0.672422	1.349962	-0.827972
H	-1.866085	1.310631	0.092415

n=4 (I)

O	-2.592858	-1.386672	-0.144797
O	-2.014781	1.236295	-1.398887
O	-2.069337	0.982097	1.550635
Br	0.719123	-0.348937	-0.003197
H	-1.628631	-1.49843	-0.211888
H	-2.672059	-0.795794	0.623076
H	-1.147048	0.675922	1.488261
H	-2.195848	1.406796	0.685568
H	-1.071895	1.0262	-1.274218
H	-2.426797	0.361117	-1.305166
O	4.050118	0.388595	0.007367
H	3.175789	-0.045534	0.013129
H	3.812047	1.320003	-0.02142

n=4 (S)

O	-1.363838	-2.033201	0.19415
O	-1.357267	0.194955	2.035721
O	-1.362244	-0.191604	-2.034519
O	-1.354056	2.037408	-0.192247
Br	1.473594	-0.001947	-0.000777
H	-0.409561	-1.858568	0.116947
H	-0.403478	0.11705	1.858405
H	-0.400305	1.857827	-0.118388
H	-0.407715	-0.119395	-1.859045
H	-1.61571	-1.413017	0.90391
H	-1.610217	0.904375	1.4156
H	-1.611065	1.418632	-0.90131
H	-1.618487	-0.899227	-1.41375

n=5 (I)

O	1.874203	0.986973	-1.832013
O	2.198461	-1.673469	-0.794933
O	2.018849	-0.67618	1.891332
O	1.646467	1.984379	0.853551
Br	-0.922388	-0.215437	-0.043429
O	-4.32623	0.111364	0.025197
H	1.054201	-0.706088	1.787557
H	2.321284	-1.103631	1.06664
H	2.002863	1.213175	1.334166
H	0.718774	1.723546	0.724717
H	2.01506	1.478364	-0.999692
H	0.931682	0.761249	-1.768421
H	1.230868	-1.7061	-0.719701
H	2.333402	-0.826213	-1.261817
H	-3.403041	-0.195934	-0.048473
H	-4.215506	1.037383	0.259968

n=5 (S)

O	0.562163	-1.338822	1.908124
O	0.486113	1.496075	1.668995
O	2.089945	2.307415	-0.383044
O	1.277701	-0.100102	-1.720606
O	2.148529	-2.270475	-0.320969
Br	-1.788899	-0.029565	-0.29303
H	-0.3288	1.311075	1.158936
H	0.733693	0.594589	1.956504
H	-0.24981	-1.212529	1.383109
H	1.193419	-1.709825	1.263329
H	0.335218	-0.073033	-1.450966
H	1.648098	0.730844	-1.365704
H	1.57666	2.050991	0.424795
H	1.614408	3.063436	-0.739262
H	1.909583	-1.479115	-0.867168
H	1.663392	-2.994392	-0.727521

n=6 (I)

O	3.088881	-0.683824	-1.537746
O	3.066968	-1.018629	1.377231
O	3.089545	1.681081	0.20849
Br	-0.001558	0.011093	-0.027779
O	-3.099855	1.281841	-1.082972
O	-3.078366	-1.604991	-0.546699
O	-3.061612	0.302463	1.685171
H	3.284515	0.225178	-1.252054
H	2.119881	-0.713478	-1.480552
H	3.272673	0.977498	0.854665
H	2.12271	1.642035	0.131252
H	2.099747	-0.937615	1.370059
H	3.262613	-1.216446	0.444916
H	-2.109694	-1.579026	-0.488861
H	-3.278598	-0.774784	-1.012661
H	-2.094974	0.359612	1.617322
H	-3.253856	-0.515606	1.194674
H	-2.132482	1.204328	-1.106497
H	-3.28252	1.276503	-0.127805

n=6 (S)

O	0.278461	2.149484	-1.47672
Br	-1.856879	-0.214144	-0.065649

O	0.008706	1.966492	1.444764
O	0.825128	-2.067547	1.442903
O	2.410637	0.294064	1.4741
O	2.532126	0.310758	-1.360325
O	0.890223	-2.033589	-1.405488
H	-0.04328	-1.654638	1.308968
H	1.430592	-1.307571	1.572293
H	-0.610376	1.27747	1.093307
H	-0.479507	2.407664	2.14614
H	0.015107	-1.612707	-1.391163
H	1.008713	-2.27178	-0.464295
H	-0.439939	1.494204	-1.418875
H	0.328222	2.469032	-0.563061
H	2.057483	-0.533345	-1.501746
H	1.858711	0.990307	-1.54774
H	2.595882	0.327706	0.510832
H	1.706922	0.951417	1.59917

n=7 (I)

O	-2.513669	-0.321308	1.788068
O	-3.622323	-1.929063	-0.157228
O	-2.656582	0.221274	-1.814817
O	-2.744026	2.111741	0.3006
Br	0.356555	0.208638	-0.032814
O	3.664658	1.40104	-0.233749
O	3.305679	-0.884145	1.572764
O	3.256722	-1.292237	-1.337847
H	-3.062287	-2.709377	-0.205312
H	-3.287616	-1.425281	0.622869
H	-3.069146	-0.562709	-1.405894
H	-1.712786	0.12296	-1.602159
H	-2.783291	0.565185	1.475625
H	-1.576168	-0.347332	1.524351
H	-2.886674	1.590705	-0.51683
H	-1.780596	2.192721	0.329911
H	2.70178	1.511687	-0.180379
H	3.751854	0.661416	-0.85949
H	3.630654	-0.022001	1.260084
H	2.343505	-0.777165	1.505501
H	3.414802	-1.496657	-0.40007
H	2.312853	-1.064901	-1.34204

n=7 (S)

Br	-2.342248	-0.031448	-0.097437
O	-0.100247	-1.611023	1.651699
O	-0.117585	2.257183	0.500502
O	0.334411	-0.713204	-2.333937
O	1.840644	-2.231311	-0.490798
H	1.329693	-1.824784	-1.223608
H	1.222901	-2.200715	0.257171
H	-0.514764	-0.565728	-1.884675
H	0.820594	0.130468	-2.223461
H	-0.825533	1.592919	0.303072
H	-0.590846	3.076673	0.673149
H	-0.811065	-1.168187	1.12314
H	-0.569149	-2.209578	2.240998
O	1.56774	0.686888	2.286993
O	1.824713	1.604503	-1.611793
H	1.029983	1.340547	1.807901
H	1.034572	-0.125352	2.237118

H	1.215102	1.986512	-0.960066
H	2.496425	1.142127	-1.066021
O	3.419655	0.060923	0.151618
H	3.029905	-0.805679	-0.084933
H	2.956208	0.299778	0.976224

n=8 (I)

O	2.523228	1.551354	1.243548
O	3.267159	-1.105668	1.79994
O	3.209992	-1.14566	-1.065
O	3.759845	1.545387	-1.354226
Br	-0.00122	-0.425096	-0.066536
O	-2.635694	1.376201	-1.347716
O	-3.75624	1.751521	1.145133
O	-3.216862	-1.423398	-1.486437
O	-3.15211	-1.057521	1.32751
H	3.129853	-0.134339	1.757745
H	2.367639	-1.448031	1.871465
H	3.440265	-1.283682	-0.1251
H	2.236813	-1.109133	-1.032353
H	1.658837	1.220832	0.940737
H	3.002375	1.730943	0.412376
H	3.644933	0.565391	-1.35352
H	3.143234	1.863392	-2.020466
H	-3.451399	-0.133364	1.420923
H	-2.18786	-0.978598	1.230555
H	-3.133582	2.295752	1.636123
H	-3.404352	1.733149	0.223379
H	-1.729553	1.12721	-1.090024
H	-3.01619	0.510086	-1.594471
H	-3.387829	-1.428893	-0.521693
H	-2.265026	-1.59007	-1.528928

n=8 (S)

O	1.104418	2.232733	0.640304
O	-0.889582	0.976282	2.32878
O	-2.810905	0.954469	0.240776
O	-0.958157	2.183159	-1.466685
O	-0.009547	-0.316438	-2.375015
O	-1.842535	-1.582003	-0.546669
O	0.17709	-1.626892	1.554029
O	-4.927904	-1.044088	-0.08851
Br	2.700488	-0.487353	-0.130874
H	-0.627774	1.379747	-1.923784
H	-0.25645	2.384835	-0.826585
H	0.843759	-0.429157	-1.9218
H	-0.625768	-0.889576	-1.878518
H	0.974603	-1.330696	1.045277
H	0.494325	-2.333547	2.124696
H	1.634318	1.434629	0.387793
H	1.75847	2.905961	0.851382
H	-0.560124	0.064996	2.241701
H	-0.202378	1.513225	1.896337
H	-1.230378	-1.811807	0.172358
H	-2.194798	-0.706504	-0.280324
H	-2.306986	1.492267	-0.4094
H	-2.296996	1.037614	1.069798
H	-4.44391	-0.215298	0.059227
H	-4.220025	-1.657119	-0.323637

Rotational temperatures for Br^- water clusters, [K]

n=1	n=2(S)	n=3(S)	n=4(I)	n=4(S)	n=5(I)	n=5(S)
25.64191	0.31013	0.15718	0.14498	0.08285	0.08250	0.05516
0.15229	0.10441	0.06799	0.03631	0.05461	0.03009	0.03916
0.15139	0.07855	0.06793	0.03556	0.05461	0.03000	0.03424

n=6(I)	n=6(S)	n=7(I)	n=7(S)	n=8(I)	n=8(S)
0.08016	0.04603	0.05734	0.04127	0.04369	0.03813
0.02102	0.03321	0.01712	0.02225	0.01406	0.01573
0.02101	0.02966	0.01664	0.02217	0.01386	0.01521

Vibrational temperatures for Br^- water clusters, [K]

n=1	n=2	n=3	n=4(I)	n=4(S)	n=5(I)	n=5(S)
199.35	90.51	105.83	12.32	97.04	4.77	49.17
394.01	198.08	107.56	16.13	112.24	11.81	62.69
857.15	222.41	137.22	66.07	113.39	33.16	87.77
2129.72	254.31	189.43	108.85	113.78	65.57	96.21
4444.51	406.24	195.44	113.58	128.36	96.74	139.63
4956.58	512.00	232.38	128.99	230.84	100.66	154.64
	590.61	497.30	169.21	255.20	109.02	183.97
	844.62	502.65	197.10	255.25	115.32	219.93
	963.47	544.45	198.36	261.56	165.55	238.09
	2119.39	619.82	234.62	512.25	232.85	268.08
	2171.64	623.71	343.34	514.48	256.89	336.02
	4339.01	835.49	492.55	514.67	259.83	349.19
	4716.13	852.19	500.22	548.82	267.65	365.46
	4794.85	859.55	540.09	639.19	337.38	369.03
	4952.03	1117.41	629.68	775.40	483.15	550.23
		2158.67	631.84	775.88	499.35	568.75
		2161.10	746.84	823.41	501.10	614.26
		2187.09	818.31	877.33	533.03	632.88
		4616.32	828.56	959.49	638.53	703.78
		4618.16	839.58	959.63	736.90	820.99
		4637.67	1130.35	1191.58	759.84	847.12
		4736.28	2118.44	2178.47	765.20	887.81
		4760.10	2159.85	2182.78	798.17	936.94
		4761.57	2160.76	2182.84	842.19	1032.16
			2184.81	2206.24	958.20	1089.90
			4622.08	4585.20	961.39	1207.00
			4658.83	4636.22	1220.39	1265.31
			4665.34	4636.37	2116.42	2160.77
			4681.06	4672.27	2180.26	2163.63
			4747.87	4689.69	2180.49	2174.10
			4751.85	4706.05	2182.00	2177.08
			4754.47	4706.48	2202.55	2208.47
			4962.70	4736.75	4554.16	4227.88
					4612.62	4255.43
					4622.03	4506.00
					4631.00	4554.31
					4654.03	4572.21
					4724.77	4619.52
					4747.92	4635.69
					4757.96	4670.37
					4779.89	4963.78
					4964.84	4965.51

n=6(l)	n=6(S)	n=7(l)	n=7(S)	n=8(l)	n=8(S)
4.97	62.26	11.07	67.82	10.79	39.29
13.48	73.36	20.70	71.14	14.87	45.30
15.94	93.74	21.80	73.57	22.14	69.84
91.34	107.02	42.42	96.50	25.64	73.48
95.02	108.62	67.69	99.58	46.14	84.89
99.93	117.30	97.86	124.76	58.85	96.17
102.76	131.99	100.65	138.37	73.77	101.47
105.89	185.43	106.69	186.59	107.26	125.97
143.21	215.21	117.85	195.12	111.65	142.94
197.89	231.47	127.64	199.23	120.12	173.94
200.33	232.01	154.40	213.12	130.10	191.30
202.95	240.41	199.58	232.07	136.04	196.59
203.61	270.37	203.57	244.66	160.29	206.69
237.46	276.52	236.55	248.92	237.51	219.75
242.23	285.12	240.05	267.00	239.95	231.36
457.90	309.89	250.23	278.37	251.64	253.33
462.52	452.73	273.74	285.30	252.34	257.01
471.22	523.82	319.25	294.65	274.16	270.76
478.82	535.02	354.75	314.49	285.20	275.15
487.28	588.62	463.13	341.35	315.38	291.62
522.98	611.60	476.91	465.04	318.93	328.52
626.68	688.59	483.90	515.33	355.07	346.74
633.71	721.58	508.40	611.03	361.47	362.67
638.21	769.10	517.63	653.08	459.25	463.80
639.43	797.34	550.12	699.88	495.54	479.26
776.83	820.07	605.27	716.09	512.02	506.18
780.43	871.54	631.94	728.58	519.01	526.54
786.09	886.20	644.17	780.80	555.67	607.63
792.20	988.12	664.52	807.94	566.01	653.23
794.01	991.64	775.25	836.26	604.48	682.59
799.73	1033.07	785.46	884.50	614.75	708.57
1148.05	1062.89	787.98	901.12	639.22	731.64
1159.72	1307.15	792.24	923.33	668.25	787.97
2154.41	2081.38	823.28	959.26	789.00	814.57
2155.24	2161.31	908.45	990.46	797.84	831.89
2156.42	2172.76	977.80	1010.48	816.87	845.26
2157.24	2191.61	1073.76	1047.41	834.13	893.97
2171.26	2200.89	1153.26	1087.59	908.97	922.32
2189.52	2215.20	1267.23	1317.76	936.50	946.21
4654.66	4240.05	2155.02	2087.07	981.52	974.38
4656.14	4437.29	2155.80	2097.58	985.87	1006.95
4705.61	4524.47	2156.74	2171.54	1073.09	1020.75
4706.90	4551.03	2162.28	2183.54	1080.97	1057.50
4708.39	4599.73	2176.57	2198.88	1263.67	1134.05
4710.77	4640.91	2184.73	2209.56	1279.16	1331.64
4767.11	4690.28	2195.61	2218.35	2156.26	2087.02
4770.36	4740.91	4327.51	4223.24	2161.35	2097.48
4772.51	4748.09	4517.87	4280.40	2161.97	2149.49
4774.14	4767.25	4600.17	4422.47	2163.02	2161.12
4784.57	4812.25	4631.55	4496.33	2183.89	2186.48
4800.57	4965.21	4656.04	4535.30	2186.40	2200.86
		4680.08	4566.89	2188.37	2210.66
		4706.46	4622.79	2196.62	2221.97
		4710.89	4692.87	4335.40	4211.89
		4726.18	4722.87	4336.94	4269.18
		4770.38	4730.78	4468.42	4397.69
		4776.11	4766.09	4518.68	4485.74
		4795.81	4769.21	4603.03	4505.55
		4849.92	4963.07	4604.19	4554.58
		4964.66	4963.89	4622.38	4597.98
				4629.33	4674.00
				4670.21	4706.43
				4674.50	4719.78
				4695.26	4744.87
				4729.29	4752.42
				4852.45	4760.88
				4900.97	4894.57
				4961.82	4961.22
				4964.69	4962.18

Geometries of I^- water clusters; number of water molecules is given by *n*.

n=1

O	0.024951	2.345884	0
I	0.024951	-1.319386	0
H	0.308911	1.409998	0
H	-0.932697	2.252486	0

n=2(I)

O	3.665884	0.164872	-0.003322
I	-0.000502	-0.253833	0.002676
O	-3.665309	0.165568	-0.002467
H	2.788189	-0.259551	-0.009007
H	3.428550	1.097327	0.012653
H	-3.423130	1.096924	0.001642
H	-2.789672	-0.263058	-0.004467

n=2(S)

O	-1.957433	-1.359617	0.010254
O	-1.324811	1.537952	-0.082054
I	1.819444	-0.14754	0.003192
H	-1.000549	-1.508002	0.044043
H	-2.00422	-0.394276	-0.082427
H	-1.242944	1.783113	0.845471
H	-0.42489	1.20067	-0.28696

n=3(I)

O	3.620083	-0.580474	0.490683
O	2.276593	1.968309	-0.119831
I	-0.379522	-0.430911	-0.124519
H	2.758924	-1.014530	0.420880
H	3.387774	0.352868	0.352814
H	2.279664	2.074282	-1.076579
H	1.449125	1.464719	0.038172
O	-3.803463	0.906294	0.340875
H	-3.012382	0.502221	-0.059601
H	-3.494144	1.105662	1.229973

n=3(S)

O	1.270287	1.487103	-0.819535
O	1.244366	-0.029364	1.700527
O	1.26529	-1.460397	-0.868841
I	-2.083138	0.001245	-0.006459
H	0.295309	-1.398123	-0.913232
H	1.437376	-1.28192	0.072128
H	0.274641	-0.10021	1.653729
H	1.422866	0.70186	1.084035
H	1.44357	0.583586	-1.136497
H	0.300042	1.494914	-0.747579

n=4 (I)

O	-2.793675	-1.108091	-0.207294
O	-1.627552	1.347369	-1.343561
O	-1.773183	0.982127	1.567005
I	0.99882	-0.987964	-0.011806
O	4.399334	0.54351	-0.001186
H	-1.914906	-1.514031	-0.278689
H	-2.699355	-0.544793	0.581356
H	-0.920076	0.515978	1.573387
H	-1.749131	1.443554	0.710473

H	-0.735479	0.96284	-1.30372
H	-2.195578	0.560361	-1.277557
H	3.682434	-0.112687	-0.043712
H	3.912759	1.364841	0.119457

n=4 (S)

O	-1.014071	-2.021606	-0.085823
O	-1.012435	0.08638	-2.021682
O	-1.011354	2.022449	0.085953
O	-1.012171	-0.08545	2.021807
I	2.203994	-0.000928	-0.000139
H	-0.046809	-1.944789	-0.130574
H	-0.04499	-0.130431	1.943838
H	-0.044181	1.944082	0.13035
H	-0.045212	0.130281	-1.943575
H	-1.222459	-1.481991	0.702587
H	-1.22096	0.703114	1.48258
H	-1.220845	1.483242	-0.702436
H	-1.222204	-0.701907	-1.482446

n=5 (I)

O	2.642923	1.513916	-0.767051
O	3.393284	-1.248799	-0.207686
O	2.137667	0.391605	1.888467
I	-0.375668	-0.753248	-0.677034
O	-3.098131	1.571555	-0.240727
O	-4.438065	-0.904632	0.542978
H	1.786304	1.197427	-1.097317
H	2.519196	1.481705	0.198023
H	1.250816	0.14323	1.578782
H	2.697315	-0.301098	1.496835
H	2.513194	-1.578298	-0.446132
H	3.402298	-0.361969	-0.610355
H	-3.619165	-1.398064	0.413347
H	-4.184078	-0.00287	0.282661
H	-2.34969	1.036899	-0.574049
H	-2.731271	1.999083	0.539931

n=5 (S)

O	0.145206	1.252606	1.92406
O	-0.16276	-1.539101	1.605785
O	-2.022483	-2.022036	-0.33436
O	-1.353841	2.498701	-0.179268
O	-1.065207	0.267304	-1.736253
I	2.444647	-0.239318	-0.663307
H	0.65285	-1.512336	1.07135
H	-0.236393	-0.606127	1.897026
H	0.946982	1.106226	1.39224
H	-0.447935	1.729885	1.311228
H	-0.107833	0.106824	-1.626641
H	-1.48611	-0.516865	-1.331037
H	-1.410592	-1.88095	0.431252
H	-1.716112	-2.83672	-0.743115
H	-1.337652	1.704663	-0.76902
H	-0.743525	3.114011	-0.596778

n=6 (I)

O	3.392137	1.510137	0.756295
O	3.475449	-0.12825	-1.655564
O	3.378289	-1.418187	0.964317
I	-0.000382	0.048667	-0.075544
O	-3.333382	-0.142712	1.713115
O	-3.470927	1.501399	-0.69896
O	-3.440707	-1.410362	-0.933136
H	3.551963	0.631072	1.141786
H	2.424887	1.538091	0.686615
H	3.554797	-1.283794	0.016083
H	2.410084	-1.414593	1.004501
H	2.509785	-0.167199	-1.729811
H	3.614223	0.633576	-1.064885
H	-2.505859	1.532058	-0.787473
H	-3.591028	1.233812	0.229826
H	-2.472846	-1.458997	-0.949187
H	-3.611795	-0.476951	-1.151388
H	-2.365965	-0.074805	1.684776
H	-3.518621	-0.815814	1.034866

n=6 (S)

O	-0.4372	2.092771	-1.494401
O	2.113442	0.709826	-1.288124
O	1.880369	0.642774	1.530236
O	0.875874	-1.999591	1.429887
O	1.034976	-1.937792	-1.403479
O	-0.792606	1.844682	1.40888
I	-2.465854	-0.817599	-0.163128
H	-0.072783	-1.818361	1.343819
H	1.277781	-1.117547	1.583564
H	-1.296568	1.059447	1.085391
H	-1.358364	2.241615	2.078414
H	0.083845	-1.770257	-1.486904
H	1.127289	-2.130179	-0.447455
H	-1.059392	1.346441	-1.525559
H	-0.493636	2.366117	-0.565533
H	1.833793	-0.212948	-1.454701
H	1.324446	1.238758	-1.506819
H	2.09533	0.724767	0.575578
H	1.058942	1.149978	1.629399

n=7 (I)

O	2.620019	0.345982	1.837625
O	3.365142	2.10633	-0.157334
O	3.193476	-1.982507	0.303531
O	2.912031	-0.155158	-1.844033
I	-0.445098	-0.629783	-0.079444
O	-3.442238	1.511246	-1.092063
O	-4.177568	-1.264847	-0.554782
O	-3.637778	0.554403	1.657933
H	2.634008	2.727428	-0.229327
H	3.15262	1.560257	0.636248
H	3.150406	0.683293	-1.401871
H	1.947013	-0.19715	-1.751669
H	2.980476	-0.491658	1.480565
H	1.669703	0.254407	1.655474
H	3.263454	-1.452522	-0.518134
H	2.265807	-2.256025	0.303531

H	-3.256788	-1.567901	-0.54294
H	-4.116205	-0.411413	-1.019743
H	-4.012097	-0.197606	1.165037
H	-2.690006	0.351139	1.668103
H	-3.575118	1.52687	-0.127385
H	-2.511282	1.253595	-1.174354

n=7 (S)

O	-0.528333	-1.164778	2.005057
O	1.081974	1.265769	2.043185
O	2.996216	0.168294	0.171101
O	1.399928	1.145433	-1.946637
O	0.038201	-1.330707	-2.118073
O	1.490095	-2.256911	0.117239
O	-0.589716	2.322396	-0.11084
I	-3.122625	-0.141353	-0.185364
H	0.992812	-2.074203	-0.708591
H	0.850653	-2.054767	0.818028
H	-0.86045	-1.129598	-1.813707
H	0.478042	-0.456954	-2.194782
H	-1.314271	1.654566	-0.156659
H	-1.039628	3.171789	-0.160471
H	-1.259637	-0.909911	1.394719
H	-0.968803	-1.611187	2.735203
H	0.539881	1.763508	1.408048
H	0.564676	0.457233	2.199253
H	0.774417	1.67838	-1.430772
H	2.073575	0.8656	-1.289498
H	2.63676	-0.742401	0.161177
H	2.509681	0.594991	0.900986

n=8 (S)

O	1.678772	2.032005	0.753841
O	-0.351107	0.742169	2.383401
O	-2.308847	0.983283	0.344952
O	-0.431116	2.249297	-1.305958
O	0.33178	-0.2123	-2.461723
O	-1.480442	-1.516835	-0.666427
O	0.544172	-1.874126	1.418837
O	-4.544679	-0.850727	-0.10257
I	3.445705	-0.838658	-0.303097
H	-0.158558	1.473698	-1.84155
H	0.296393	2.357199	-0.672635
H	1.209569	-0.431426	-2.109592
H	-0.283657	-0.79151	-1.969341
H	1.370784	-1.631926	0.937017
H	0.78408	-2.642826	1.946188
H	2.19616	1.254998	0.434051
H	2.345234	2.675638	1.0149
H	-0.074314	-0.176732	2.226414
H	0.35811	1.271117	1.978556
H	-0.880445	-1.84459	0.023562
H	-1.788055	-0.653303	-0.317216
H	-1.792209	1.547534	-0.271896
H	-1.778312	0.97785	1.167404
H	-4.006995	-0.068853	0.103739
H	-3.883028	-1.481807	-0.411785

Rotational temperatures for I^- water clusters, [K]

n=1	n=2(I)	n=2(S)	n=3(I)	n=3(S)	n=4(I)	n=4(S)
24.87216	3.14832	0.31688	0.19721	0.15962	0.10706	0.08416
0.11766	0.05170	0.07299	0.04040	0.04941	0.03286	0.03970
0.11711	0.05086	0.05959	0.03456	0.04936	0.02982	0.03970

n=5(I)	n=5(S)	n=6(I)	n=6(S)	n=7(I)	n=7(S)	n=8(S)
0.08177	0.05406	0.08030	0.04512	0.05269	0.04067	0.03703
0.02333	0.02890	0.01753	0.02472	0.01503	0.01669	0.01210
0.02169	0.02646	0.01752	0.02245	0.01443	0.01660	0.01176

Vibrational temperatures for I^- water clusters, [K]

n=1	n=2(I)	n=2(S)	n=3(I)	n=3(S)	n=4(I)	n=4(S)
150.64	33.92	62.80	17.88	101.02	17.00	62.64
307.40	50.46	173.82	22.93	109.83	23.47	81.70
761.94	73.17	211.38	56.96	119.13	67.63	81.83
2116.60	140.41	257.88	83.21	201.29	92.18	103.10
4577.14	156.88	344.02	140.72	201.86	99.49	106.31
4953.45	307.87	486.41	168.81	236.08	112.38	228.36
	309.78	526.02	221.08	491.32	135.69	263.37
	701.75	852.04	271.75	497.11	197.51	263.40
	722.63	869.90	289.39	544.30	204.31	278.52
	2116.13	2111.34	344.94	644.92	236.93	464.53
	2120.07	2162.40	463.3	651.39	287.88	478.11
	4650.56	4454.94	503.88	800.02	469.90	478.43
	4662.94	4735.24	694.16	813.16	482.87	541.62
	4953.49	4817.39	854.85	821.04	514.45	628.11
	4954.29	4944.10	867.18	1161.25	632.41	756.62
			2105.77	2153.60	646.40	756.74
			2114.31	2155.16	660.29	782.47
			2163.03	2179.00	771.78	856.73
			4478.76	4640.26	792.45	970.50
			4663.61	4672.42	802.04	970.51
			4724.51	4676.83	1168.45	1244.83
			4859.22	4734.26	2111.57	2173.15
			4950.28	4735.59	2150.55	2177.15
			4956.86	4741.50	2151.20	2177.18
					2174.06	2200.62
					4637.63	4515.64
					4685.66	4585.69
					4694.13	4585.88
					4699.18	4623.82
					4744.16	4728.48
					4748.09	4739.67
					4777.90	4740.03
					4959.20	4765.51

n=5(I)	n=5(S)	n=6(I)	n=6(S)	n=7(I)	n=7(S)	n=8(S)
17.01	37.26	6.14	58.75	18.18	60.02	37.40
19.37	58.22	14.43	65.32	19.83	67.46	40.56
27.92	88.95	19.22	70.84	24.11	69.14	62.11
33.14	93.22	82.17	95.66	42.60	94.53	63.43
95.52	122.61	88.82	106.84	76.57	96.13	78.40
98.95	134.07	90.68	109.50	92.09	120.39	94.93
111.56	158.29	97.14	120.32	97.62	126.06	98.69
163.66	219.35	98.81	176.05	103.30	168.55	121.01
201.34	245.19	115.66	204.08	106.54	184.54	128.23
208.95	276.42	200.15	224.42	111.68	187.50	169.44
231.66	336.98	200.58	232.93	128.18	198.09	178.61
240.14	350.00	205.29	238.52	206.51	231.30	188.52
284.60	367.37	205.66	272.26	209.61	237.53	191.72
336.27	389.09	238.43	277.89	241.99	238.47	201.87
406.93	551.09	239.23	287.57	242.82	259.30	234.16
475.40	566.49	438.47	301.94	261.24	282.35	242.80
478.96	572.97	448.93	419.20	279.17	286.36	248.04
488.09	609.11	456.92	500.23	316.73	295.20	267.10
507.81	673.40	463.06	517.79	380.02	308.90	275.29
637.22	780.28	478.63	557.16	456.28	334.25	289.98
648.49	803.74	507.39	597.49	461.52	421.72	326.85
766.80	856.25	622.57	674.18	475.52	481.05	344.54
779.21	938.36	628.13	701.96	505.89	593.55	355.54
784.86	1040.95	635.86	757.82	519.75	621.61	428.35
820.84	1090.64	636.97	780.15	528.74	677.58	454.90
875.46	1187.31	742.76	795.34	593.19	694.02	480.62
1173.61	1259.88	754.88	839.85	633.39	712.67	500.67
2103.08	2157.55	759.07	862.03	639.54	764.26	585.88
2151.87	2161.17	762.65	946.57	672.20	787.70	627.63
2152.69	2174.45	768.89	992.41	751.07	812.62	667.79
2156.56	2177.19	771.52	1027.04	759.01	846.82	693.89
2175.09	2202.24	1166.60	1054.20	765.22	848.87	717.45
4553.72	4245.98	1176.67	1315.55	769.70	892.92	770.15
4634.55	4289.98	2144.53	2076.61	786.65	927.73	794.04
4688.03	4527.03	2145.77	2154.36	895.35	948.19	808.92
4698.63	4568.76	2148.48	2167.22	992.22	1004.80	822.20
4709.64	4599.48	2148.85	2184.22	1057.94	1041.13	844.45
4754.49	4614.73	2160.77	2198.04	1181.11	1079.45	870.20
4764.67	4643.84	2176.17	2209.52	1285.69	1315.47	908.33
4801.04	4701.37	4631.40	4316.79	2147.37	2081.70	947.45
4905.60	4958.85	4633.02	4417.02	2148.62	2092.67	964.76
4952.32	4965.71	4690.01	4503.53	2156.25	2164.50	1018.26
		4690.63	4536.80	2165.65	2178.92	1049.54
		4697.01	4581.14	2168.19	2194.92	1124.30
		4701.31	4650.77	2182.76	2202.41	1327.99
		4780.80	4717.88	2187.60	2217.29	2079.41
		4781.26	4757.32	4341.56	4331.59	2087.77
		4794.85	4775.33	4499.51	4372.24	2146.74
		4798.87	4798.11	4568.02	4410.42	2154.21
		4809.16	4802.40	4600.27	4493.84	2181.24
		4818.30	4958.05	4627.37	4518.44	2196.10
				4690.10	4566.14	2204.40
				4692.10	4627.77	2219.63
				4731.07	4700.40	4315.35
				4767.27	4742.13	4357.15
				4795.47	4765.16	4396.20
				4796.18	4778.73	4486.49
				4813.53	4784.21	4507.23
				4851.60	4954.73	4557.24
				4960.00	4955.95	4580.38
						4683.31
						4729.65
						4744.80
						4749.68
						4763.40
						4771.08
						4900.07
						4953.53
						4954.30

Geometry of water with 6-311G** basis set

O	0.000000		
H	0.961970	0.000000	
H	0.961970	1.513876	0.000000

Electronic energy for water, [Hartree/particle]: -76.4474481

Rotational temperatures for water, [K]: 38.4454, 21.0016, 13.5821

Vibrational temperatures for water, [K]: 2098.66, 4878.52, 5002.35

Geometries of H^+ water clusters; number of water molecules is given by *n*.

n=1

O	0.000046	-0.000045	-0.069708
H	0.931547	-0.162981	0.185966
H	-0.324669	0.888303	0.185805
H	-0.607247	-0.724959	0.185896

n=2

O	1.195034	-0.033775	-0.048231
H	1.705125	0.710175	-0.399241
H	1.66807	-0.45413	0.684804
H	0.008226	0.022717	0.000595
O	-1.19472	-0.030408	0.047625
H	-1.671702	-0.480273	-0.664456
H	-1.71223	0.714978	0.383145

n=3

O	0.000038	0.862456	-0.042561
H	-0.889275	0.322433	0.010687
H	0.000365	1.660961	0.50134
H	0.88904	0.321763	0.010801
O	2.125044	-0.417887	-0.008473
H	2.565162	-0.842237	0.736383
H	2.730373	-0.416739	-0.758828
O	-2.124672	-0.418976	-0.008803
H	-2.729328	-0.416224	-0.759747
H	-2.569615	-0.834699	0.738056

n=4

O	0.000366	-0.000408	-0.429995
O	-0.571207	2.422098	0.122371
O	2.384002	-0.716637	0.122371
H	0.931241	-0.311982	-0.178066
H	-0.735125	-0.650779	-0.178576
H	-0.195385	0.961622	-0.178201
H	-0.365738	2.912096	0.925755
H	-0.704527	3.068114	-0.580116
H	3.010515	-0.923853	-0.579885
H	2.70596	-1.13895	0.925959
O	-1.813286	-1.70499	0.122265
H	-2.307092	-2.143483	-0.579528
H	-2.338843	-1.773294	0.926556

n=5

O	0.971616	-0.000914	0.619802
O	-1.354302	-0.780074	0.870738
O	1.269822	2.451089	-0.140888
O	2.542329	-1.65608	-0.591366
H	-0.033962	-0.296559	0.710437
H	1.099115	0.937265	0.28579
H	1.546999	-0.664808	0.133019
H	3.253237	-2.090314	-0.107342
H	2.315759	-2.231246	-1.329794
H	-2.112889	-0.493909	0.305968
H	-1.684491	-0.94382	1.759429
H	1.379899	2.768974	-1.043215
H	1.711272	3.085231	0.434573
O	-3.380336	-0.029156	-0.689985
H	-3.956074	0.725386	-0.528242
H	-3.911887	-0.675128	-1.167026

n=6

O	-1.618145	-0.703511	-0.696607
O	-0.073893	0.827938	0.531723
O	2.19271	-0.113968	1.006461
O	-4.030766	-1.378846	0.24933
O	0.031267	3.240855	-0.455107
O	3.478283	-1.835051	-0.60589
H	-0.715978	0.219581	-0.004617
H	-1.715753	-0.698083	-1.653283
H	-2.496009	-0.93566	-0.314144
H	0.00207	1.746324	0.146472
H	0.850028	0.402009	0.71139
H	2.423065	-0.324582	1.916196
H	2.668914	-0.747485	0.42156
H	0.710181	3.575135	-1.050598
H	-0.264936	3.990379	0.072482
H	3.371584	-2.79139	-0.581602
H	4.373444	-1.673773	-0.921796
H	-4.272919	-2.259674	0.551561
H	-4.769342	-0.802127	0.467097

n=7

O	-1.822881	-0.34917	-0.696719
O	0.089776	-1.051371	0.734187
O	2.52152	-2.078025	-0.361074
O	1.050172	1.528802	0.9884
O	-4.209172	-0.713839	0.274693
O	3.261103	0.681999	-0.194733
H	-1.045374	-0.745748	-0.116105
H	-1.619505	0.647278	-0.796114
H	-2.722602	-0.504345	-0.285387
H	0.44863	-0.192844	1.044203
H	0.843622	-1.530817	0.345795
H	2.492641	-2.557445	-1.198223
H	3.021556	-2.641624	0.242735
H	1.911917	1.359832	0.527365
H	1.259611	1.986075	1.810076
H	3.188779	-0.264696	-0.397505
H	3.823506	1.081513	-0.864405
H	-4.884638	-1.147673	-0.257554
H	-4.444108	-0.862032	1.196609
O	-0.969602	2.030069	-0.777633

H	-0.24345	2.098951	-0.122848
H	-1.397918	2.885863	-0.865613

n=8

O	-0.769489	-0.098504	0.591311
O	0.698558	1.516471	-0.495013
O	-2.778952	-0.736408	-0.838453
O	0.678815	-2.199485	1.183466
O	3.035334	0.309436	-1.112338
O	1.066192	3.88831	0.772588
O	-5.333814	-0.258115	-0.085542
O	3.254232	-2.356324	-0.028026
H	-1.563751	-0.340558	0.004653
H	-0.248368	-0.914322	0.834537
H	-0.122411	0.638579	0.125837
H	-3.689101	-0.558301	-0.515729
H	-2.790258	-0.585893	-1.788058
H	-5.953649	-0.962198	0.129081
H	-5.670611	0.53601	0.34049
H	1.584064	-2.29274	0.839963
H	0.665669	-2.579836	2.066645
H	1.561097	1.129018	-0.766324
H	0.869102	2.360177	-0.02384
H	0.90898	4.714831	0.305294
H	1.708445	4.089089	1.460238
H	3.301476	-3.09978	-0.641867
H	4.035475	-2.432391	0.533748
H	3.164922	-0.608034	-0.823211
H	3.43192	0.383295	-1.985404

Electronic energy for H^+ water clusters, [Hartree/particle]

n=0	n=1	n=2	n=3	n=4
0.000000	-76.729892	-153.242286	-229.734100	-306.218716

n=5	n=6	n=7	n=8
-382.693304	-459.166042	-535.645424	-612.110752

Rotational temperatures for H^+ water clusters, [K]

n=1	n=2	n=3	n=4	n=5	n=6	n=7	n=8
15.97956	8.73953	0.97830	0.13083	0.11007	0.06540	0.08014	0.03887
15.97186	0.41476	0.13713	0.13070	0.05274	0.03381	0.03029	0.02056
8.96928	0.41330	0.12337	0.06809	0.04046	0.02448	0.02445	0.01494

Vibrational temperatures for H^+ water clusters, [K]

n=1	n=2	n=3	n=4	n=5	n=6	n=7	n=8
994.72	250.22	86.94	83.50	24.37	22.43	33.58	16.18
2146.70	395.96	89.12	84.70	45.76	31.83	52.74	25.96
2147.74	492.51	168.62	92.39	81.37	41.13	57.23	28.46
4598.23	619.22	196.09	151.98	87.60	53.77	69.28	43.75
4717.43	640.22	246.48	162.90	115.06	78.83	96.56	53.22
4719.08	788.37	443.27	168.99	151.50	90.82	121.20	60.90
	1296.72	491.29	267.52	157.86	116.21	131.86	77.15
	1878.66	499.38	324.68	176.36	123.42	148.66	86.65
	1955.02	511.51	328.40	303.72	152.77	209.67	101.18
	2160.87	569.55	360.27	310.83	163.72	230.34	117.75
	2275.05	753.81	442.65	330.49	173.74	243.03	127.07
	4807.08	1423.24	443.11	341.60	297.08	250.89	135.12
	4820.61	1585.37	475.59	362.43	303.17	271.43	213.09
	4921.16	2048.44	477.26	368.49	311.98	278.41	221.69
	4928.90	2100.97	533.23	389.86	330.80	310.23	223.25
		2133.19	887.53	422.38	350.14	317.67	243.78
		2151.72	1277.26	451.32	362.39	369.02	246.07
		3104.12	1279.24	492.00	368.54	393.17	257.94
		3341.89	1530.17	553.16	376.44	402.98	272.85
		4876.59	2091.60	712.53	382.04	436.73	288.02
		4877.49	2091.73	922.29	459.03	468.08	298.68
		4899.85	2109.84	1127.37	499.85	495.26	329.35
		4993.65	2189.12	1218.59	529.44	531.67	337.53
		4994.36	2189.52	1337.39	649.85	538.85	358.73
			3705.89	1653.29	687.33	581.81	365.91
			3706.70	2074.78	955.70	639.55	372.79
			3877.19	2091.57	1087.58	758.95	389.03
			4881.53	2103.59	1103.02	804.28	472.40
			4881.68	2122.44	1231.08	828.10	513.78
			4883.13	2182.92	1427.83	903.58	594.60
			4998.66	2212.22	1668.22	959.18	613.31
			4998.83	2985.64	2085.85	995.67	627.41
			4999.46	3925.29	2095.03	1080.81	660.87
				4009.68	2098.72	1199.86	831.51
				4328.16	2115.84	1276.07	853.74
				4883.14	2133.80	1351.30	873.41
				4883.90	2205.34	1742.87	941.88
				4885.41	2217.92	2076.97	1047.39
				4962.09	3214.11	2088.15	1063.29
				5001.20	3433.72	2101.98	1178.76
				5001.91	4090.68	2109.08	1284.13
				5004.44	4399.95	2136.02	1438.15
					4402.06	2165.25	1800.77
					4884.28	2204.57	2076.80
					4886.99	2334.04	2087.80
					4896.79	3030.12	2088.79
					4966.75	3620.78	2108.52
					4968.95	4044.44	2111.93
					5002.85	4227.28	2124.25
					5007.40	4480.60	2132.89
					5019.22	4551.34	2166.00
						4669.06	2282.36
						4730.35	2463.31
						4850.63	3683.38
						4885.62	4102.31
						4937.67	4421.78
						4961.70	4476.15
						4980.79	4491.23
						4983.25	4677.91
						5004.92	4733.92
							4850.47
							4892.30
							4893.83
							4963.68
							4970.01
							4971.23
							4974.84
							5015.72
							5017.43